NICKEL METAL AND NICKEL OXIDE FOR SATURABLE ABSORBER FEMTOSECONDS PULSE LASER PERFORMANCE

By

SITI ASMA BINTI CHE AZIZ

Thesis Submitted to the School of Graduate Studies, Universiti Putra Malaysia, in Fulfilment of the Requirements for the Degree of Doctor of Philosophy

December 2024

FK 2024 78

Abstract of thesis presented to the Senate of Universiti Putra Malaysia in fulfilment of the requirement for the degree of Doctor of Philosophy

NICKEL METAL AND NICKEL OXIDE FOR SATURABLE ABSORBER FEMTOSECONDS PULSE LASER PERFORMANCE

By

SITI ASMA BINTI CHE AZIZ

December 2024

Chairman : Professor Adzir bin Mahdi, PhD
Faculty : Engineering

Ultrashort pulses generated from fibre lasers can be achieved through passive mode-locking using a saturable absorber. This study investigated the use of nickel metal and nickel oxide as saturable absorbers integrated with tapered fibres. The conventional method for creating saturable absorbers with these materials predominantly utilised a fibre ferrule configuration. While this approach offers compatibility and flexibility, it suffers from a limited interaction length between light and the saturable absorber material. To address this limitation, this research focused on the fabrication of nickel- and nickel oxide-based saturable absorbers embedded in polydimethylsiloxane as a host polymer. By exploiting the evanescent field along the tapered fibre, efficient light-matter interaction was achieved, enabling effective modulation of transmitted light. The saturable absorbers were characterised for their morphological, optical absorption, and crystallinity properties. The fabrication process involved liquid-phase exfoliation, ultrasonication, and spin coating onto the tapered fibre.

The performance of nickel-based saturable absorbers was first evaluated by integrating them into an erbium-doped fibre laser ring cavity for dispersion management studies. The nickel-based absorber demonstrated nonlinear transmission characteristics, including a modulation depth of 4.77%, a saturation intensity of 265 MW/cm², and nonsaturable absorption of 61.6%. Adjusting the single-mode fibre length within the cavity significantly influenced the pulse properties. Longer single-mode fibre lengths resulted in narrower spectral bandwidth and slower pulse width but caused increased attenuation losses. An optimised single-mode fibre length of 24.2 metres provided the best results, achieving stable pulses with a peak extension ratio of 57.55 dB at a repetition rate of 7.99 MHz.

Subsequent experiments focused on nickel oxide-based saturable absorbers to assess the influence of various material concentrations on laser performance. Nickel oxide concentrations ranging from 0.1 to 3.0 mg/mL were tested. Concentrations below 0.5 mg/mL failed to support mode-locking due to insufficient material, while concentrations exceeding 2.1 mg/mL led to particle re-aggregation and performance degradation. The saturable absorber with a nickel oxide concentration of 0.9 to 1.5 mg/mL exhibited the optimal balance, offering a modulation depth of 4.1 to 4.9 %, reduced transmission losses, and stable mode-locking performance.

In conclusion, this research advanced ultrashort pulse lasers by integrating nickel-based saturable absorbers with tapered fibres, while optimising fibre length and material concentration. This study aligns with the united nations sustainable development goal (SDG 9), which emphasises industry, innovation, and infrastructure, by providing high-precision, energy-efficient solutions for advanced manufacturing

processes such as cutting, drilling, and welding. Furthermore, these innovations hold significant potential for applications in various fields, including telecommunications, biomedical imaging, and precision measurement.

Keywords: saturable absorber, tapered fibre, nickel materials, pulse fibre laser

SDG: GOAL 9: Industry, Innovation and Infrastucture

Abstrak tesis yang dikemukakan kepada Senat Universiti Putra Malaysia sebagai memenuhi keperluan untuk ijazah Doktor Falsafah

LOGAM NIKEL DAN LOGAM NIKEL TEROKSIDA SEBAGAI PENYERAP BOLEH TEPU UNTUK PRESTASI DENYUT LASER FEMTOSAAT

Oleh

SITI ASMA BINTI CHE AZIZ

Disember 2024

Pengerusi : Profesor Adzir bin Mahdi ,PhD
Fakulti : Kejuruteraan

Denyut ultrapendek yang dihasilkan daripada laser gentian boleh dicapai melalui penguncian ragam pasif menggunakan penyerap tepu. Kajian ini menyiasat penggunaan logam nikel dan nikel oksida sebagai penyerap tepu yang disepadukan dengan gentian tirus. Kaedah konvensional untuk mencipta penyerap tepu dengan bahan-bahan ini kebanyakannya menggunakan konfigurasi ferul gentian. Walaupun pendekatan ini menawarkan keserasian dan fleksibiliti, namun panjang interaksi antara cahaya dan bahan penyerap tepu adalah terhad. Untuk menangani kekangan ini, penyelidikan ini memberi tumpuan kepada fabrikasi penyerap tepu berasaskan nikel dan nikel oksida yang tertanam dalam polimer hos polidimetilsiloksana. Dengan memanfaatkan medan evanescent di sepanjang gentian tirus, interaksi cahaya-jirim yang cekap dicapai, membolehkan modulasi cahaya yang dihantar dilakukan dengan berkesan. Penyerap tepu ini dicirikan berdasarkan sifat morfologi, penyerapan optik, dan kristalinitinya. Proses fabrikasi melibatkan pengelupasan fasa cecair, ultrasonikasi, dan salutan putar ke atas gentian tirus.

Prestasi penyerap tepu berasaskan nikel pada awalnya dinilai dengan menyepadukannya ke dalam rongga gelang laser gentian doped erbium untuk kajian pengurusan penyebaran. Penyerap berasaskan nikel menunjukkan ciri transmisi tak linear, termasuk kedalaman modulasi sebanyak 4.77%, keamatan tepu sebanyak 265 MW/cm², dan penyerapan tidak tepu sebanyak 61.6%. Pelarasan panjang gentian mod tunggal dalam rongga tersebut memberi kesan ketara terhadap sifat denyut. Panjang gentian mod tunggal yang lebih panjang menghasilkan jalur spektrum yang lebih sempit dan lebar denyut yang lebih perlahan tetapi menyebabkan peningkatan kehilangan pelemahan. Panjang gentian mod tunggal yang dioptimumkan sebanyak 24.2 meter memberikan hasil terbaik, mencapai denyut stabil dengan nisbah lanjutan puncak sebanyak 57.55 dB pada kadar pengulangan 7.99 MHz.

Eksperimen seterusnya memberi tumpuan kepada penyerap tepu berasaskan nikel oksida untuk menilai pengaruh pelbagai kepekatan bahan terhadap prestasi laser. Kepekatan nikel oksida antara 0.1 hingga 3.0 mg/mL diuji. Kepekatan di bawah 0.5 mg/mL gagal menyokong penguncian mod disebabkan oleh bahan yang tidak mencukupi, manakala kepekatan melebihi 2.1 mg/mL menyebabkan pengagregatan semula zarah dan kemerosotan prestasi. Penyerap tepu dengan kepekatan nikel oksida sebanyak 0.9 hingga 1.5 mg/mL menunjukkan keseimbangan yang optimum, menawarkan kedalaman modulasi sebanyak 4.1 hingga 4.9 %, pengurangan kehilangan transmisi, dan prestasi penguncian mod yang stabil.

Kesimpulannya, penyelidikan ini memajukan laser denyut ultrapendek dengan menyepadukan penyerap tepu berasaskan nikel dengan gentian tirus, dengan mengoptimumkan panjang gentian dan kepekatan bahan. Kajian ini selaras dengan

matlamat pembangunan mampan (SDG 9), yang menekankan industri, inovasi, dan infrastruktur, dengan menyediakan penyelesaian berketepatan tinggi dan cekap tenaga untuk proses pembuatan lanjutan seperti pemotongan, penggerudian, dan pengelasan. Selain itu, inovasi ini mempunyai potensi yang signifikan untuk aplikasi dalam pelbagai bidang, termasuk telekomunikasi, pengimejan bioperubatan, dan pengukuran berketepatan tinggi.

Kata Kunci: penyerap tepu, gentian tirus, nikel, denyut ultra pendek

SDG: MATLAMAT 9: Industri, Innovasi, Infrastruktur

ACKNOWLEDGEMENTS

Praise be to Allah, the Most Gracious and the Most Merciful. With His permission and abundant blessings, I have successfully completed the journey as a PhD student. This PhD experience has been a beautiful and unforgettable journey, one that has taught me to see myself as a servant of Allah, always dependent on Him and to continually draw closer to Him. Inshaa Allah.

By the decree of Allah, Prof. Dr. Mohd Adzir bin Mahdi became a main Supervisor for this PhD study. I would like to express my heartfelt gratitude to Prof. Adzir, for his guidance, ideas, support, and constructive criticisms that I have gained a deeper understanding in necessary knowledge. I extend my heartfelt thanks for the patience, encouragement, and unwavering commitment towards his supervision.

I am also grateful to my supervisor committee Dr. Nadiah Husseini binti Zainol Abidin, Assoc. Prof. Dr. Che Azurahanim binti Che Abdullah, and Dr. Muhammad Idzdihar bin Idris for their invaluable suggestion, support, and expertise throughout this research journey.

Special thanks go to my husband, mother, and father for their immense support and assistance in ensuring the smooth progression of this PhD journey. To my children, they have been my strength to complete this PhD thesis. I convey my heartfelt appreciation as my family understands the challenges present in this journey, which required considerable sacrifice.

I am infinitely grateful to Allah for bringing friends who have consistently been my listeners and have provided invaluable assistance throughout my PhD study. A heartfelt thank you to Dr. Maisarah, Dr. Rosyati, and Dr. Amaniah for providing me with a space to express my feelings of sadness, joy, and excitement throughout this PhD journey. Special thanks are also extended to Dr. Norita for her invaluable assistance throughout the journey, providing insightful ideas and offering solutions to the challenges I faced. Not forgetting the backbone of the lab, En. Zamili, who consistently ensured the smooth progress of my tapered fibre fabrication.

Not to be forgotten, I would like to express my gratitude to Dr. Amir Murad, Dr. Yasmin, Aishah, Dr. Hafizah, Dr. Nurul and others for providing ideas and guidance as a senior member in the lab. Lastly, I am thankful to all those who directly or indirectly contributed to this PhD journey. Only the grace of Allah can adequately repay the kindness extended by each of you.

This thesis was submitted to the Senate of Universiti Putra Malaysia and has been accepted as fulfillment of the requirement for the degree of Doctor of Philosophy. The members of the Supervisory Committee were as follows:

Mohd Adzir bin Mahdi, PhD
Professor
Faculty of Engineering
Universiti Putra Malaysia
(Chairman)

Nadiah Husseini binti Zainol Abidin, PhD
Senior Lecturer
Faculty of Engineering
Universiti Putra Malaysia
(Member)

Che Azurahanim binti Che Abdullah, PhD
Associate Professor
Faculty of Science
Universiti Putra Malaysia
(Member)

Muhammad Idzdihar bin Idris, PhD
Senior Lecturer Ts.
Faculty of Electronic and Computer Technology and Engineering
Universiti Teknikal Malaysia Melaka
(Member)

ZALILAH MOHD SHARIFF, PhD
Professor and Dean
School of Graduate Studies
Universiti Putra Malaysia

Date: 17 April 2025

TABLE OF CONTENTS

		Page
ABSTRACT		i
ABSTRAK		iv
ACKNOWLEDGEMENTS		vii
APPROVAL		ix
DECLARATION		xi
LIST OF TABLES		xvi
LIST OF FIGURES		xvii
LIST OF APPENDICES		xxiii
LIST OF ABBREVIATIONS		xxiv
CHAPTER		
1	**INTRODUCTION**	1
	1.1 Overview	1
	1.2 Problem Statement and Motivation	4
	1.3 Research Objective	6
	1.4 Research Scope and Limitations	6
	1.5 Material Selection and Rationale	9
	1.6 Thesis Organization	10
2	**LITERATURE REVIEW**	12
	2.1 Overview	12
	2.2 Dispersion and Non-Linear Pulse Propagation	12
	2.2.1 Optical Kerr Effect	15
	2.2.2 Self-Phase Modulation	16
	2.2.3 Soliton Propagation	18
	2.3 Principle of Pulsed Fibre Laser Generation	20
	2.3.1 Q-Switching	20
	2.3.2 Mode-Locked (ML) Fibre Laser	21
	2.3.3 Saturable Absorber Structure and Deposition Techniques	26
	2.4 Material-Based Tapered Fibre Saturable Absorber	34
	2.5 Development of Nickel-Based Saturable Absorber	40
	2.5.1 Nickel Metal and Nickel Oxide Properties	40
	2.5.2 Nickel-Based Material as Saturable Absorber	42
	2.6 Summary	45
3	**Ni METAL/PDMS AS SATURABLE ABSORBER FOR NET DISPERSION MANAGEMENT ON EDFL PERFORMANCE**	46
	3.1 Overview	46
	3.2 Ni Metal Characterisation in SEM-EDX, XRD, and UV-VIS-NIR	47
	3.3 Ni/PDMS SA Fabrication Process	52
	3.3.1 Preparation of Ni/PDMS Composite	52

3.3.2 Preparation and Characterisation of a Tapered Fibre 53
3.3.3 Deposition of Ni/PDMS SA and its Characterisation 56
3.4 Nonlinear Saturable Absorption Measurement of Ni/PDMS-SA 59
3.5 Mode-Locked EDFL Cavity Setup 60
3.6 Net Dispersion Calculations 62
3.7 Ni/PDMS SA at Alteration Net Dispersion for Pulse Laser Performance 63
3.7.1 Optical Spectrum for Mode-Locked Pulse Laser 63
3.7.2 Oscilloscope Pulse Train 67
3.7.3 Pulse Duration 69
3.7.4 Peak-to-Pedestal Extinction Ratio 70
3.7.5 Average Output Power and Pulse Energy 72
3.7.6 Optical Spectrum Stability, Autocorrelator Stability and Time Bandwidth Product 76
3.8 Summary 78

4 NiO/PDMS SATURABLE ABSORBER FOR INVESTIGATING CONCENTRATION EFFECTS ON EDFL PERFORMANCE 81
4.1 Overview 81
4.2 NiO Characterisation in SEM-EDX, XRD and UV-VIS-NIR 82
4.3 NiO/PDMS SA Fabrication at Various NiO Concentrations 85
4.4 NiO/PDMS SA Functionality at Various Concentration and its Characterisation 89
4.4.1 Integration onto EDFL and Transmission Loss of Various NiO/PDMS SA 89
4.4.2 SEM-EDX Characterisation of Various Concentration NiO/PDMS SA 91
4.4.3 Nonlinear Saturable Absorption Properties of Various Concentration NiO/PDMS SA 95
4.5 Effect of NiO Concentrations on Pulse Laser Performance 97
4.5.1 Optical Spectrum of Continuous Wave Laser 98
4.5.2 Optical Spectrum of Mode-Locked Pulse Laser 99
4.5.3 Oscilloscope Pulse Train 107
4.5.4 Peak-to-Pedestal Extinction Ratio (PER) 108
4.5.5 Pulse Duration and Time Bandwidth Product 109
4.5.6 Average Output Power and Pulse Energy 112
4.5.7 Optical Spectrum Stability and Autocorrelator Stability 115
4.6 Summary 117

5 CONCLUSION AND FUTURE RECOMMENDATION 122
5.1 Conclusion 122
5.2 Outcome and Research Contribution 124
5.3 Suggestion for Future Work 125

REFERENCES 126
APPENDICES 141
BIODATA OF STUDENT 159
LIST OF PUBLICATIONS 160

LIST OF TABLES

Table		Page
2.1	Latest Tapered Fibre Based SA Reported from 2022-2024	38
2.2	Development of Ni-Based Materials as SA for Q-Switched and Mode-Locked in EDFL Cavity	44
3.1	Estimated GVD Values for the Laser Cavity Setup for Different Cavity Lengths according to the Experiment	63
3.2	Summarizes the Laser Performance for Different SMF Lengths	75
3.3	TBP Estimation for ML-EDFL by Altering the Fibre Lengths	78
4.1	NiO/PDMS Decorated on Tapered Fibre with Different Concentrations	88
4.2	Modulation Depths for Different NiO Concentrations of SA	97
4.3	Optical Spectrum Properties of All SAs	103
4.4	Repetition Rate and PER of the RF Spectrum for Each NiO Concentration SA	109
4.5	Pulse Width, Spectral Bandwidth, Central Wavelength, and TBP at Maximum Pump Power	112
4.6	Summary of Optical Spectra and Auto-Correlator Stability for All NiO/PDMS Samples with Different Concentrations of SA	117
4.7	Summarize of Non-Linear Characteristics and ML-EDFL Performances of Differents NiO Concentrations	119

LIST OF FIGURES

Figure		Page
1.1	Highlighted Are the Research Scope Encompases an Overview of Studies Focusing on Mode-Locking EDFL with SA the Study of SA Based on Ni-Based Materials, Including Ni-Metal and Ni-Oxide, Employing Tapered Fibre Technique	8
2.1	Summary of Mode-Locked Fibre Laser Operating Regimes Sorted by Net Dispersion. Ref: [22]	14
2.2	Types of Third Order Susceptibility Ref: [31]	15
2.3	Gain and Loss in the Passively Q-Switched Laser System [51]	20
2.4	Mode-Locked Laser Intensity: (a) Effectively Locked Phases; (b) Random Phases Ref: [51]	22
2.5	Active Mode Locking (a) Resonant Cavity Mechanism (b) Modulating the Loss and Saturated Gain in the Cavity	23
2.6	Diagram of Passively Mode-Locking with Fast Saturable Absorber, Time Dependence, and Gain Ref: [55]	24
2.7	Pauli Blocking Effect-Induced Linear Absorption and Saturable Absorption Processes (a) Illustrates the Photon Excitation of Electrons to the Conduction Band, Forming Hot Fermi–Dirac Electrons, (b) Rapid Electron Thermalization via Intraband Scattering, Establishing a Hot Carrier Distribution, and (c) an Increased Carrier Population at High Light Intensities, Triggering the Pauli Blocking Effect. Ref: [58]	27
2.8	Example of a Nonlinear Transmission Curve for Saturable Absorber	28
2.9	Fibre Ferrule Techniques for SA in Both Powder and Thin Film Forms	30
2.10	D-Shaped Fibre with Material Deposition	31
2.11	Schematic Illustration of the Flame Approach Used for Fabrication of the Tapered Fibre. Ref: [81]	32
2.12	Principle for Optical Evanescent-Field Deposition of Nanocomposites. Ref: [83]	33
3.1	Flowchart of the Methodology	47

3.2	(a) SEM-EDX Morphology Analysis (a) SEM Image of Ni Powder, (b) EDX Spectra of Elemental Composition (c) Elemental Mapping in Weight and Atomic Percentage, and (d) Measurements of the Diameter of Ni Particles in the Histogram Image	48
3.3	XRD Peaks of Ni Powder	49
3.4	Tauc Plot of (a) Ni Powder and (b) PDMS Alone for Band Gap Measurements	50
3.5	Optical Absorbance of Ni Powder, Ni/PDMS, and PDMS	51
3.6	Preparation Step for Ni/PDMS Composite	53
3.7	Vytran GPX-3400 Optical Processing Workstation	53
3.8	Schematic Diagram of Tapered Fibre at the Upper Length, Lower Length, and Waist Length	55
3.9	(a) Measurement Setup of Tapered Fibre Loss and (b) Transmission Loss of Bare Tapered Fibre Characterisation	56
3.10	Step Process of Deposition of Material to Tapered SA and Spin Coating Techniques	57
3.11	(a) Illustration of Ni/PDMS Composite Deposition Process on the Tapered Fibre (b) Transmission Loss of Bare Tapered Fibre and Ni/PDMS SA	58
3.12	(a) SEM Micrograph of Ni/PDMS SA along the Waist Region of the Tapered Fibre; (b) Material Composition Detected in Ni/PDMS SA	59
3.13	Non-Linear Characterisation of SA; (a) Set-Up of the Balanced Two-Detector System and (b) Nonlinear Transmittance Curve of the Ni/PDMS-SA	60
3.14	Laser Configuration Setup of EDFL with Ni/PDMS-SA Tapered Fibre	61
3.15	(a) OSA Spectrum for the EDFL with 22.6 nm Length SMF and (b) its Enlarged Spectrum Indicating the Calculation of the Sepctral Bandwidth. (c) Laser Spectral Bandwidth against Variation of Total SMF Length in the EDFL Cavity	65
3.16	Optical Spectrum of MLFL Employing Additional (a) SMF-22.6 m and (b) SMF-25.8 m	66
3.17	Laser Output of EDFL with SMF-21.8 m; (a) OSA Spectrum at CW Laser Threshold, ML Threshold and ML at Maximum Pump Power, and (b) Enlarged View with CW Component at Maximum Pump Power of 250 mW	67

3.18 (a) Osciloscope Trace for SMF-22.6 m and (b) Fundamental Repetition Rate Decrements Observed with SMF Alterations 68

3.19 (a) Autocorrelation Trace of the Generated Pulses at SMF-22.6 m (b) Pulse Duration Results Obtained by Employing Different Additional SMF Lengths 70

3.20 (a) RF Spectrum of the Laser Output Measured with SMF-22.6 m and (b) Measurements of PER across the Additional SMF Length in the EDFL Cavity 71

3.21 (a) An Average Output Power Over Pump Power (b) Pulse Energy over Pump Power for Overall SMF Length (c) Average Output Power and Pulse Energy at Maximum Pump Power Plotted over SMF length (d) CW Laser and ML Treshold Power over SMF Length 74

3.22 OSA Stability Captured within 200 Minutes for SMF-22.6 m (a) 3-D Spectogram of Spectrum Stability, and (b) Spectral Bandwidth and Central Wavelength Extracted from the Spectogram 77

3.23 AC Stability within 60 Minutes at SMF-22.6 m (a) 3-D Spectogram of AC Stability, and (b) Pulse Width of the AC Stability within 60 Minutes 77

4.1 Flowchart of the Methodology in Chapter 4 82

4.2 Morphoplogy Analysis (a) SEM Image of NiO Powder, (b) Elemental Analysis of NiO Powder, (c) Elemental Distribution in Percentage and (d) Counts of NiO Particles with Average Diameters 83

4.3 XRD Peak NiO Powder Crystanality 84

4.4 (a) Tauc Plot of NiO Powder, and (b) Absorbance (a.u) of NiO Powder, NiO/PDMS and PDMS Alone Versus Wavelength 85

4.5 Transmission Loss of (a) NiO SA-01 to SA-05 and (b) Enlarged Image of Wavelength 1558–1563 nm 90

4.6 Transmission Loss of (a) NiO/PDMS SA-06 to SA-18 and (b) Enlarged Image of y-axis (2.74 to 5.03 dB) 91

4.7 SEM-EDX for SA-01, SA-03 and SA-05 (a) SEM Micrograph of NiO/PDMS with 0.1 mg/mL in Tapered Fibre, (b) Material Composition Detected in SA-01; (c) SEM Micrograph of NiO/PDMS in Tapered Fibre with 0.3 mg/mL (d) Material Composition Detected in SA-03 (e) SEM Micrograph of NiO/PDMS in Tapered Fibre with 0.5 mg/mL (f) Material Composition Detected in SA-05 92

4.8 SEM-EDX Analysis of NiO/PDMS SA at Different Concentrations: (a), (c), and (e) SEM Micrographs of NiO/PDMS SA along the Waist Region of Tapered Fibre for Concentrations SA-09, SA-15, and SA-

21, Respectively. (b), (d), and (f), Corresponding Material Composition Detected in SA-09, SA-15, and SA-21, Respectively 94

4.9 Nonlinear Saturable Absorption for Different Concentrations of NiO/PDMS SA 96

4.10 (a) CW Laser Wavelength Spectrum for SA-06 to SA-21 and (b) Enlarged Spectrum from 1558 to 1564 nm Wavelength Range 99

4.11 Optical Spectrum for Threshold and Maximum Power Mode-Locking and its Respective 3-dB Bandwidth for (a) SA-06 (b) Enlarged View of SA-06 (c) SA-09 (d) Enlarged View SA-09 (e) SA-12 and (f) Enlarged View of SA-12 101

4.12 Optical Spectrum for Threshold and Maximum Power Mode-Locking and its Respective 3-dB Bandwidth for (a) SA-15 (b) Enlarged View of SA-15 (c) SA-18 (d) Enlarged View SA-18 (e) SA-21 and (f) Enlarged View of SA-21 102

4.13 Spectrogram of Mode-Locking Spectrum for (a) SA-06, (b) Top View of SA-06, (c) SA-09, (d) Top View of SA-09, (e) SA-12, and (f) Top View of SA-12 105

4.14 Spectrogram of Mode-Locking Spectrum for (g) SA-15, (h) Top View of SA-15, (i) SA-18, (j) Top View of SA-18, (k) SA-21, and (l) Top View of SA-21 106

4.15 Oscilloscope Trace of Pulse Laser Output Using SA-06 107

4.16 RF Spectrum of Mode-Locked for SA-06 108

4.17 Autocorrelation Traces at Maximum Pump Power for (a) SA-06, (b) SA-09, (c) SA-12, (d) SA-15, (e) SA-18, and (f) SA-21 111

4.18 Average Output Power and Pulse Energy against Input Pump Power for: (a) SA-06, (b) SA-09, (c) SA-12, (d) SA-15, (e) SA-18, and (f) SA-21 114

4.19 Spectrum Stability for SA-06 (a) 3-D Spectrogram within 200 Minutes (b) Overview of (c) Measurements of 3-dB Bandwidth and Central Wavelength over 200 Minute 116

4.20 Autocorrelator Trace Stability for SA-06 (a) 3-D Spectogram of Normalised Autocorrelator within 60 Minutes. (b) Pulse-Width (fs) Measurements within 60 Minutes 116

4.21 Modulation Depth of NiO/PDMS SA Relationship (a) SA Transmission Loss (dB) and Non-Saturable Loss %. (b) Pulse Width Shortening (fs) and 3-dB Spectral Bandwidth Broadening (nm) 120

A1	OSA Spectrum Highlighted the 3 dB Spectral Measurements for (a) SMF-23.4 m, (b) SMF-24.2 m (c) SMF-25.0 m, (d) SMF-25.8 m, (e) SMF-26.6 m (f) SMF-27.4 m	141
A2	OSA Spectrum Highlighted the 3 dB Spectral Measurements for (a) SMF-28.2 m, (b) SMF-29.0 m (c) SMF-29.8 m, (d) SMF-30.6 m, (e) SMF-31.4 m (f) SMF-32.2 m	142
B1	(a) Oscilloscope Trace for SMF-21.8 m (b) PER Measurement (c) AC Trace for SMF-21.8 m	143
B2	3-D Spectrogram for OSA Stability for SMF-21.8m within 200 Minutes	143
C1	Oscilloscope Trace in Time Domain Measurement for (a) SMF-23.4 m, (b) SMF-24.2 m (c) SMF-25.0 m, (d) SMF-25.8 m, (e) SMF-26.6 m (f) SMF-27.4 m	144
C2	Oscilloscope Trace in Time Domain Measurement for (a) SMF-28.2 m, (b) SMF-29.0 m (c) SMF-29.8 m, (d) SMF-30.6 m, (e) SMF-31.4 m (f) SMF-32.2 m	145
D1	AC Trace Measurement for (a) SMF-23.4 m, (b) SMF-24.2 m (c) SMF-25.0 m, (d) SMF-25.8 m, (e) SMF-26.6 m (f) SMF-27.4 m	146
D2	AC Trace Measurement for (a) SMF-28.2 m, (b) SMF-29.0 m (c) SMF-29.8 m, (d) SMF-30.6 m, (e) SMF-31.4 m (f) SMF-32.2 m	147
E1	RF Spectrum Measurement for (a) SMF-23.4 m, (b) SMF-24.2 m (c) SMF-25.0 m, (d) SMF-25.8 m, (e) SMF-26.6 m (f) SMF-27.4 m	148
E2	RF Spectrum Measurement for (a) SMF-28.2 m, (b) SMF-29.0 m (c) SMF-29.8 m, (d) SMF-30.6 m, (e) SMF-31.4 m (f) SMF-32.2 m	149
F1	OSA Spectrum Stability for (a) SMF-23.4 m, (b) SMF-24.2 m (c) SMF-25.0 m, (d) SMF-25.8 m, (e) SMF-26.6 m (f) SMF-27.4 m	150
F2	OSA Spectrum Stability (a) SMF-28.2 m, (b) SMF-29.0 m (c) SMF-29.8 m, (d) SMF-30.6 m, (e) SMF-31.4 m (f) SMF-32.2 m	150
G1	AC Trace Stability for (a) SMF-23.4 m, (b) SMF-24.2 m (c) SMF-25.0 m, (d) SMF-25.8 m, (e) SMF-26.6 m (f) SMF-27.4 m	151
G2	AC Trace Stability for (a) SMF-28.2 m, (b) SMF-29.0 m (c) SMF-29.8 m, (d) SMF-30.6 m, (e) SMF-31.4 m (f) SMF-32.2 m	151
H1	Oscilloscope Trace for Different Concentrations (a) SA-09 (b) SA-12 (c) SA-15, (d) SA-18, and (e) SA-21	152
I1	PER for Different Concentrations (a) SA-09 (b) SA-12 (c) SA-15, (d) SA-18, and (e) SA-21	153

J1 Spectrum Stability for SA-09 (a) 3-D Spectrogram within 200 Minutes (b) Overview of (c) Measurements of 3-dB Bandwidth and Central Wavelength over 200 Minutes 154

J2 Spectrum Stability for SA-12 (a) 3-D Spectrogram within 200 Minutes (b) Overview of (c) Measurements of 3-dB Bandwidth and Central Wavelength over 200 Minutes 154

J3 Spectrum Stability for SA-15 (a) 3-D Spectrogram within 200 Minutes (b) Overview of (c) Measurements of 3-dB Bandwidth and Central Wavelength over 200 Minutes 155

J4 Spectrum Stability for SA-18 (a) 3-D Spectrogram within 200 Minutes (b) Overview of (c) Measurements of 3-dB Bandwidth and Central Wavelength over 200 Minutes 155

J5 Spectrum Stability for SA-21 (a) 3-D Spectrogram within 200 Minutes (b) Overview of (c) Measurements of 3-dB Bandwidth and Central Wavelength over 200 Minutes 156

K1 Autocorrelator Stability for SA-09 (a) 3-D Spectogram of Normalised Autocorrelator within 60 Minutes. (b) Pulse-Width (fs) Measurements within 60 Minutes 157

K2 Autocorrelator Stability for SA-12 (a) 3-D Spectogram of Normalised Autocorrelator within 60 Minutes. (b) Pulse-Width (fs) Measurements within 60 Minutes 157

K3 Autocorrelator Stability for SA-15 (a) 3-D Spectogram of Normalised Autocorrelator within 60 Minutes. (b) Pulse-Width (fs) Measurements within 60 Minutes 158

K4 Autocorrelator Stability for SA-18 (a) 3-D Spectogram of Normalised Autocorrelator within 60 Minutes. (b) Pulse-Width (fs) Measurements within 60 Minutes 158

K5 Autocorrelator Stability for SA-12 (a) 3-D Spectogram of Normalised Autocorrelator within 60 Minutes. (b) Pulse-Width (fs) Measurements within 60 Minutes 158

LIST OF APPENDICES

Appendix		Page
A	OSA Spectrum Over SMF at Maximum Pump Power	141
B	Multiple Pulse Oberserved from Oscilloscope, PER Measurement, AC and OSA Stability for SMF-21.8 m	143
C	Osciloscope Trace for Different SMF Length	144
D	Autocorrelator Trace for Different SMF Length	146
E	RF Spectrum-PER Measurements for Different SMF Length	148
F	OSA Spectrum Stability for Different SMF Length	150
G	AC Stability Measurements for Different SMF Length	151
H	Osciloscope Trace for Different Nio Concentrations	152
I	Peak Extention Ratio (PER) for Different Nio Concentrations	153
J	OSA Spectrum Stability for Different Nio Concentrations	154
K	Auto Correlator Stability for Differents Nio Concentrations	157

LIST OF ABBREVIATIONS

ASE	Amplified spontaneous emission
CNT	Carbon nanotube
CS	Conventional soliton
CVD	Chemical vapor deposition
CW	Continuous wave
DS	dissipative soliton
EDX	Energy dispersive x-ray spectroscopy
FWHM	Full width at half maximum
FWM	Four Wave Mixing
GVD	Group velocity dispersion
LD	Laser diode
Ni	Nickel
NiO	Nickel Oxide
NIR	Near infrared
NLO	Nonlinear optical
NLP	Noise like pulse
NSE	Nonlinear Schrodinger Equation
OC	Optical coupler
OPM	Optical power metre
OSA	Optical spectrum analyser
PC	Polarisation controller
PDMS	Polydimethylsiloxane
RBW	Resolution bandwidth
RSA	Reverse saturable absorption
SA	Saturable absorber

SESAM	Semiconductor saturable absorber mirror
SEM	Scanning Electron Microscope
SMFs	Single mode fibres
SPM	Self Phase Modulation
TBP	Time bandwidth product
THF	Tetrahydrofuran
TMD	Transition metal dichalcogenides
TPA	Two photon absorption
UV-VIS-NIR	Ultraviolet visible near-infrared
VBW	Video bandwidth
VOA	Variable optical attenuator
WDM	Wavelength division multiplexer

CHAPTER 1

INTRODUCTION

1.1 Overview

Femtosecond fibre lasers are renowned for their ultrashort pulse durations and exceptionally high peak powers, making them invaluable in fields such as micromachining, biomedical applications, and optical sensing. Notably, ultrashort pulses in the 1.55 μm wavelength range are particularly advantageous for remote sensing, light detection and ranging, and also space communication, owing to their minimal transmission loss and eye-safe properties. Passive mode-locking is the predominant technique for generating these ultrashort pulses, with saturable absorbers (SAs) playing a crucial role. Conventional SAs, such as semiconductor saturable absorber mirrors (SESAMs), have been widely used, but have limitations, including low damage thresholds and complex fabrication processes.

Advancements in nanomaterials have introduced a variety of new SAs with superior nonlinear optical (NLO) properties. Recent advancements in nanomaterials have significantly enhanced ultrashort pulse generation in fibre lasers through the development of novel SAs. Materials such as black phosphorus, carbon nanotubes (CNTs), and graphene have been effectively utilised as SAs, enabling the production of femtosecond pulses with high stability. For instance, black phosphorus thin films have been employed in mode-locked fibre lasers to achieve pico seconds pulse [1]. Similarly, graphene-based SAs have demonstrated efficient ultrafast pulse generation due to their exceptional optical properties [2]. Transition metal dichalcogenides (TMDs), such as molybdenum disulfide (MoS_2) and tungsten disulfide (WS_2) have

been incorporated into fibre lasers, resulting in stable mode-locked operation with pulse durations in the femtosecond range [3]. Transition metal oxides (TMOs), including titanium dioxide (TiO_2) exhibits a broad absorption spectrum that extends into the near-infrared (NIR) region, despite its band gap being around 3.2 eV (ultra violet region) [4].

Metals and metal oxides exhibit distinct structural and electronic properties that influence their applications in various fields. While metals typically possess closely packed crystalline structures that facilitate high electrical and thermal conductivity, metal oxides consist of metal cations bonded to oxygen anions, resulting in diverse lattice structures that can exhibit semiconducting or insulating behavior [5]. Focusing on nickel (Ni) and its oxide, nickel oxide (NiO), Ni exhibits a face-centered cubic (FCC) crystal structure, characterised by a uniform arrangement of nickel atoms. For instance, Ni displays significant thermal expansion near its melting point, indicating strong temperature-dependent density changes [7]. Furthermore, its alloying capabilities with metals like copper enhance mechanical properties and corrosion resistance, while its electrochemical activity makes it essential in advanced batteries such as lithium-ion technologies [8]. NiO is a versatile material with exceptional thermal and chemical stability, making it suitable for catalysis [10], energy storage [9], and photodetedtor [17]. Its nanoparticles effectively absorb ultraviolet light, with band gap energies of 2.4–4.95 eV, influenced by annealing conditions [9].

Ni and NiO have also emerged as a promising candidate in photonics, particularly as a SA material for ultrafast laser applications, offering an alternative to SESAM technology. This shift is driven by NiO's strong optical absorption, and high thermal

stability, enabling effective saturable absorptions of laser pulses with enhanced durability and performance. To date, Ni has been utilised as a SA in fibre ferrule configurations to produce Q-switched pulse lasers, particularly in the regions of 1, 1.5, and 2 μm [11]. Additionally, Ni/polyvinyl alcohol (PVA) composites, incorporating Ni nanoparticles have been used to generate Q-switched fibre laser pulses in erbium-doped fibre lasers (EDFLs) [12] and ytterbium-doped fibre lasers (YDFLs) [13]. NiO-based materials have also demonstrated potential in Q-switched laser applications, such as NiO/chitosan for EDFLs [14] and NiO/polyethylene oxide (PEO) for Q-switched EDFLs [15]. Furthermore, mode-locked pulse lasers with a 950 fs pulse duration have been achieved using NiO/PEO in fibre ferrule-based configurations [16]. All of the cited works above utilised the fibre ferrule configuration for the SA structure.

The choice of SA structure and deposition technique is crucial for optimising performance in fibre laser systems. Configurations such as fibre ferrules, tapered fibres, and D-shaped fibres enhance the interaction of the SA material with the light interactions, while techniques like chemical vapour deposition (CVD), pulsed laser deposition (PLD), and spin coating allow precise control over material properties, improving laser performance. In conclusion, femtosecond fibre lasers show great potential, and ongoing research is focused on developing robust SAs. The integration of nanomaterials with tapered fibre based structures is a promising approach to overcoming current limitations and achieving reliable ultrashort pulse generation for industrial use.

1.2 Problem Statement and Motivation

While Ni and NiO have been successfully employed as SAs in fibre ferrule configurations to generate Q-switched lasers, there remains a significant gap in advancing their capabilities for mode-locked lasers. Existing studies on Ni-based SAs, such as Ni/PVA composites, have focused solely on Q-switched pulse generation in EDFL and YDFL. Although NiO/PEO, have demonstrated mode-locking capabilities, they are limited to producing pulses with a duration of 950 fs. To address these limitations, this study proposes the use of Ni/PDMS and NiO/PDMS as alternative SA materials to achieve mode-locked lasers with significantly shorter pulse durations, pushing the boundaries of current research in this area. Furthermore, the deposition of SA materials onto fibre ferrules presents significant challenges in fibre laser applications. Uncontrollable material thickness often necessitates multiple trials to achieve short pulse generation, increasing complexity and time requirements. The thin-film placement process demands exceptional precision, and the restricted contact area inherent in fibre ferrule techniques limits the efficiency of light-matter interaction [17]. These limitations hinder the development of consistent and reproducible SAs for ultrashort pulse generation. To address these issues, the tapered fibre structure is chosen for its ability to confine and enhance light interaction as SA due to its reduced fibre diameter. Spin-coating method combined with tapered fibre offers a promising solution, enabling control of composite thickness and enhanced reproducibility of SAs.

The lack of effective dispersion management in laser systems significantly limits the control over nonlinear phase shifts, leading to undesirable pulse distortions. This results in reduced pulse energy levels and higher average peak power, which directly

affects the overall efficiency and performance of the laser system. To address this, it is crucial to develop and optimise techniques for managing dispersion, ensuring the balance between pulse broadening and compression. Achieving this balance is essential for enhancing laser performance, optimising pulse characteristics, and improving the efficiency of the system in both high-power and ultrashort pulse laser applications. Therefore, the second objective is to optimise dispersion by varying the length of single-mode fibres (SMFs) in a ring-cavity EDFL with a Ni/PDMS tapered fibre SA, and evaluate their impact on pulse characteristics.

The challenge of material concentration deposition lies in optimising the nonlinear characteristics of the SA. Insufficient or excessive concentrations of material can lead to ineffective saturable absorption, resulting in unstable mode-locking or excessive energy losses within the laser system. Recent studies have highlighted the importance of controlling the CNT concentration during SA fabrication to achieve desired optical properties [18]. However, challenges such as CNT agglomeration, light scattering, and uneven distribution within the polymer matrix limit their performances [19]. Additionally, the reaggregation of CNTs at higher concentrations can further impede the mode-locked fibre laser performance by increasing the losses and threshold [20]. These challenges highlight the need for improved approaches to address them, particularly by optimising the nonlinear optical (NLO) properties through varying NiO material concentrations, as proposed in the third objective of this study. Achieving such optimisation could significantly improve mode-locking stability, pulse duration, and overall laser efficiency.

1.3 Research Objective

To address the challenges as mentioned in problem statement above, this study aims to employ a tapered fibre SA incorporating nickel material using the spin-coating technique. The specific objectives of this research are as follows:

1. To fabricate and characterise Ni/PDMS and NiO/PDMS composite on tapered fibres using a spin coating technique as SA.
2. To analyse pulse performance of Ni/PDMS-SA based on varying the net dispersion in a ring-cavity EDFL.
3. To analyse the influence of varying NiO/PDMS-SA concentration in a ring-cavity EDFL on pulse performance.

1.4 Research Scope and Limitations

Figure 1.1 provides an overview of the research scope and delineates the key components and techniques employed in the study. This highlights the SA as the focal point for passive mode-locking pulse laser generation, particularly within the context of an EDFL. This study utilised a tapered fibre SA structure combined with a spin-coating technique to embed a polymer composite. The chosen dimension profile of the tapered fibre is based on previous work that emphasised the optimisation of moderate insertion loss in bare tapered fibres [21]. The tapered region was employed with a fixed waist length of 0.8 mm and an up/down taper length of 30 mm. For this proof-of-concept study using nickel materials, these dimensions were chosen based on the assumption that tapering loss could be minimised. These dimensions were consistently applied across all experiments involving tapered fibre fabrication to ensure uniformity in the results.

Furthermore, the material deposition onto the tapered fibre was performed using the spin-coating technique, with the speed and duration fixed at 4000 rpm and 6 minutes, respectively. These parameters were selected based on a previous study [21], which demonstrated that at a spin-coating speed of 4000 rpm and a duration of 6 minutes, the thickness of the BP/PDMS composite was optimized to approximately 5 μm. This thickness was found to be ideal for producing tapered fibre SAs suitable for pulse generation and effective SA operation. Therefore, the same spin-coating settings were used across all experiments for SA fabrication, assuming they would yield a similar optimum thickness of the nickel composite for effective SA.

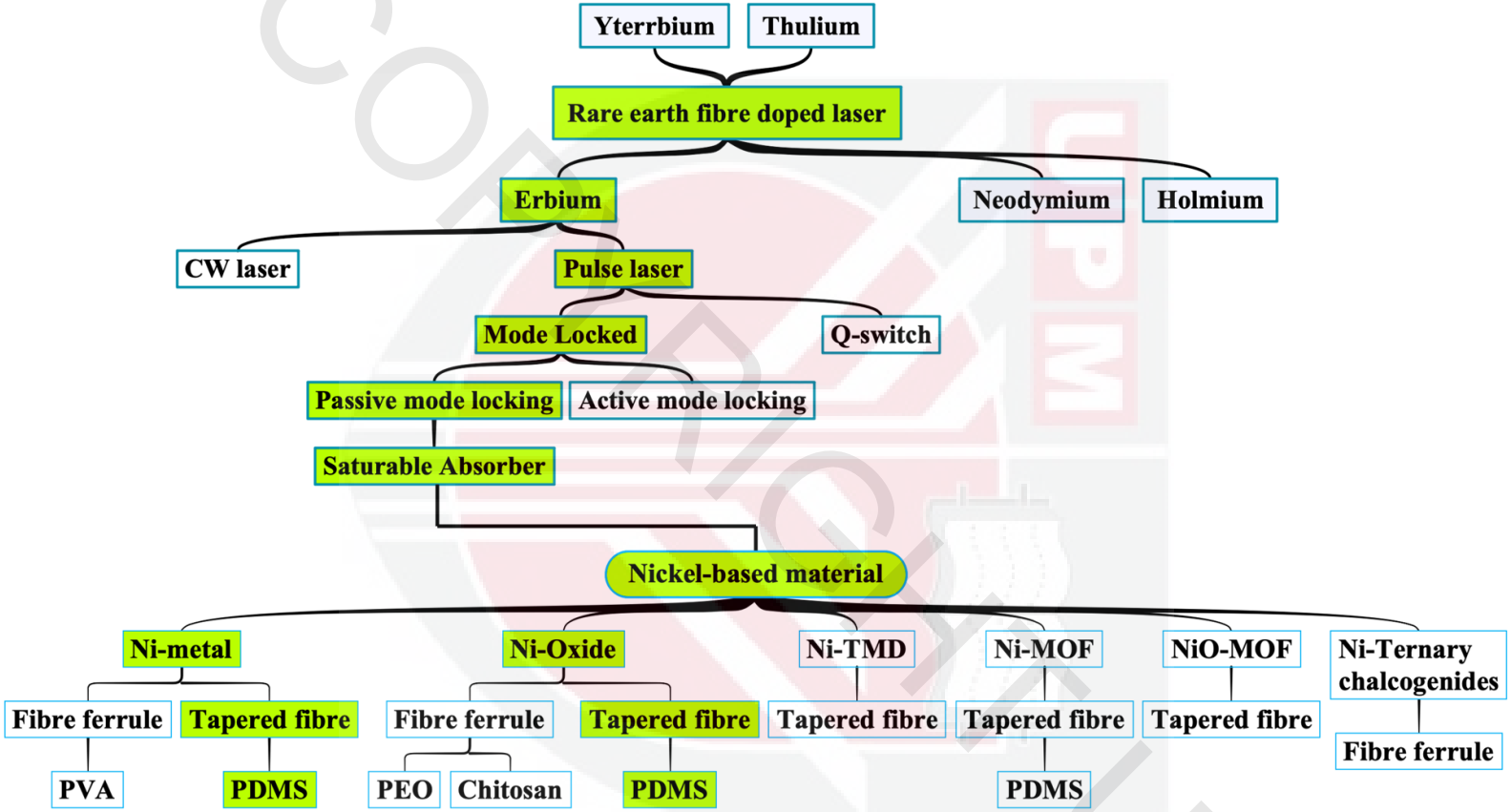

Figure 1.1 : Highlighted Are the Research Scope Encompases an Overview of Studies Focusing on Mode-Locking EDFL with SA the Study of SA Based on Ni-Based Materials, Including Ni-Metal and Ni-Oxide, Employing Tapered Fibre Technique

1.5 Material Selection and Rationale

In this study, Ni/PDMS and NiO/PDMS composites are used as SAs for integration into a ring-cavity EDFL system. The tapered fibre dimension profile and spin-coating settings (speed and duration) were explained in section 1.4 above for this proof-of-concept study using nickel materials. The selection of materials for objectives 2 and 3 is crucial for optimising the performance of the saturable absorber and ensuring the desired laser characteristics.

- **Nickel:** Nickel's ferromagnetic nature poses challenges for achieving uniform dispersion, as exposure to a magnetic field (e.g., when using a magnetic stirrer) causes Ni to aggregate, forming localised clusters near the magnetic source. This disrupts the homogeneity of the composite and leads to no clear trend in the variation of nickel concentration across the sample, resulting in non-representative SA characteristics. Despite the challenge posed by its ferromagnetic nature, nickel was selected for the second objective because its performance remains relatively stable without the need for concentration variation, as seen in objective 3. This characteristic makes Ni particularly suitable for optimising the SMF length and pulse characteristics, as the focus in this phase is on evaluating the impact of fibre length rather than material concentration.
- **Nickel Oxide:** In contrast, NiO offers greater consistency in composite dispersion and exhibits more predictable trends in SA properties with varying material concentrations. The investigation into different NiO concentrations enables a more detailed study of how concentration influences in EDFL performance. The ability to vary NiO concentration and observe its effect on pulse characteristics is central to objective 3, which seeks to optimise NiO concentration in PDMS.

Therefore, for objective 2, the performance of the Ni/PDMS tapered fibre SA is assessed with respect to its influence on the laser pulse characteristics and net

dispersion in the ring-cavity EDFL. For objective 3, NiO/PDMS samples with varying NiO concentrations are prepared to determine the optimal concentration for enhanced laser efficiency and dispersion management.

1.6 Thesis Organization

Chapter 1 provides a brief introduction to research topic and problem statement. The problem statement explains the knowledge gap that the research aims to address. The research objectives provide a clear outline of what the research aims to achieve, and the research scope defines the boundaries of the study. Finally, the thesis organisation explains how the thesis is structured, outlining the chapters and their respective contents.

Chapter 2 discusses the principles governing ultrashort pulse generation via passive mode-locking, as well as the utilisation of nickel-based saturable absorbers. The chapter begins with dispersion and nonlinear pulse propagation, encompassing phenomena such as the optical Kerr effect, Self-Phase Modulation (SPM), and soliton propagation. Subsequently, the discussion shifts to the fundamental principles underlying pulse-fibre laser generation, covering topics such as Q-switching and mode-locked pulse-fibre lasers. Following this, the discussion pertains to the application of saturable absorbers and various deposition techniques, including methods utilising fibre ferrules, D-shaped fibres, and tapered fibre techniques. Finally, this chapter discusses the development of nickel-based saturable absorbers in EDFL, which have been reported in various forms, including metals, metal oxides, TMDs, metal-organic frameworks (MOF), and ternary TMDs.

Chapter 3 explores Ni/PDMS as a SA for managing net dispersion in ring-cavity EDFLs with passive mode-locking technique. The chapter begins with the characterisation of Ni using various techniques, including scanning electron microscopy (SEM), X-ray diffraction (XRD), and ultraviolet visible near-infrared (UV-VIS-NIR) absorption. This is followed by a detailed description of the fabrication process of the Ni/PDMS-SA and its subsequent scanning electron microscopy energy-dispersive X-ray (SEM-EDX) characterisation. Subsequently, the Ni/PDMS-SA was integrated into the proposed ring-cavity EDFL for analysis of the output power, mode-locking stability, pulse duration, and spectral characteristics. Through a comprehensive examination of these parameters, the performance of the proposed ring-cavity EDFL is evaluated by studying the effective net dispersion management.

Chapter 4 describes the investigation of NiO-doped in the PDMS polymer as a SA, with the aim of assessing its performance with varying concentrations on the laser functionality. The concentration of the NiO was adjusted by altering its weight before incorporating into the PDMS polymer matrix. The performance of the NiO/PDMS-SA was thoroughly analysed, focusing on the output power, mode-locking stability, pulse duration, and spectral characteristics across different concentrations of the material. Through examination of these parameters, this chapter aims to ascertain the optimal concentration of NiO/PDMS for efficient operation in a ring-cavity EDFL.

Chapter 5 serves as the endpoint of the research efforts, offering a summary of the findings and drawing conclusions based on the results. Additionally, it provides recommendations for future research based on the insights gained throughout the study.

CHAPTER 2

LITERATURE REVIEW

2.1 Overview

In this literature review, the discussion begins with dispersion and non-linear pulse propagation, encompassing topics such as dispersion, optical Kerr effect, SPM, and soliton propagation. Following that, the subsequent section explores the principles underlying pulsed fibre laser generation, covering both Q-switching and mode-locking techniques. Furthermore, another segment of this review provides insights into SA structures, including fibre ferrule, D-shaped, and tapered fibre configurations, along with their respective deposition methods. The subsequent section investigates material-based tapered fibres as SAs, incorporating recent studies on various materials, deposition techniques in tapered fibres, and the associated nonlinear characteristics. Finally, this literature review discusses the advancement of nickel-based materials as SAs in fibre lasers, outlining the properties of Ni metal and NiO along with their utilisation in erbium pulse fibre lasers.

2.2 Dispersion and Non-Linear Pulse Propagation

In mode-locked fibre lasers, dispersion and nonlinearity are two key elements that significantly affect pulse dynamics. Dispersion, the phenomenon in which distinct light wavelengths propagate through a medium at varying speeds, leads to pulse compression or broadening [22]. The three primary types of dispersion that affect optical pulse propagation in fibre optics and laser systems are chromatic dispersion (CD), intermodal dispersion, and polarisation mode dispersion (PMD) [23]. The wavelength-dependent group index in optical fibres has a notable effect known as CD,

resulting in the temporal spreading of optical pulses as they propagate through the fibre.

In standard SMFs, CD consists of two primary components: waveguide dispersion, which is influenced by the physical structure of the fibre, and material dispersion, which arises from variations in the refractive index of the fibre with the wavelength [24]. This phenomenon is also known as group velocity dispersion (GVD), which is attributed to the wavelength-dependent group velocity of the wave [25]. GVD refers to the broadening or compression of a pulse resulting from different spectral components travelling at different speeds. It can be either anomalous (negative) or normal (positive) based on the sign of the dispersion coefficient. The parameter of β_2 known as total net cavity dispersions where positive values of β_2 indicate normal dispersion, where higher frequency components travel faster than lower frequency components, while negative values indicate anomalous dispersion, where the opposite is true [26].

Dispersion compensation is a critical component in optical fibre communication systems for mitigating the spread of optical or light pulses. The most commonly used methods for dispersion adjustment include employing a dispersion-compensating fibre (DCF) loop, where the negative dispersion matches that of the transmitting fibre [27]. Fibre bragg grating (FBG) devices offer smaller dimensions and lower insertion losses than DCF. Unlike DCF, FBGs can effectively compensate for CD across various wavelength variations, making them the preferred method for CD compensation [28].

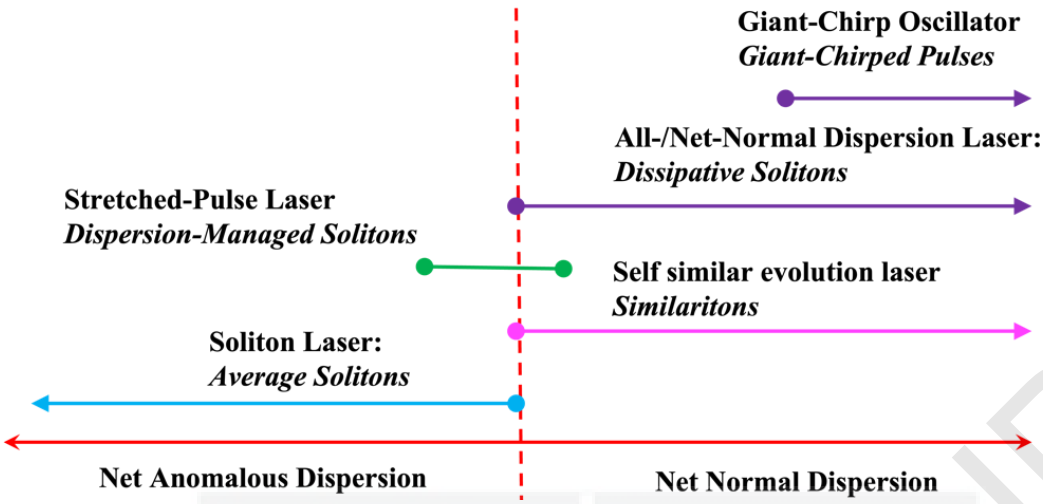

Figure 2.1 : Summary of Mode-Locked Fibre Laser Operating Regimes Sorted by Net Dispersion. Ref: [22]

Figure 2.1 illustrates various pulse-shaping regimes, such as solitons, dispersion-managed solitons, dissipative solitons (DS), giant-chirped pulses, and similaritons. In contrast, nonlinear pulse propagation describes the behaviour of light waves as they travel through nonlinear media, demonstrating a non-linear relationship between the electric field and polarisation of the medium [29]. This phenomenon is significant in various fields of science and technology, including fibre optics, laser physics, and nonlinear optics [30]. Its pivotal role in optical communication systems lies in its capability to facilitate the high-speed transmission of data over extensive distances.

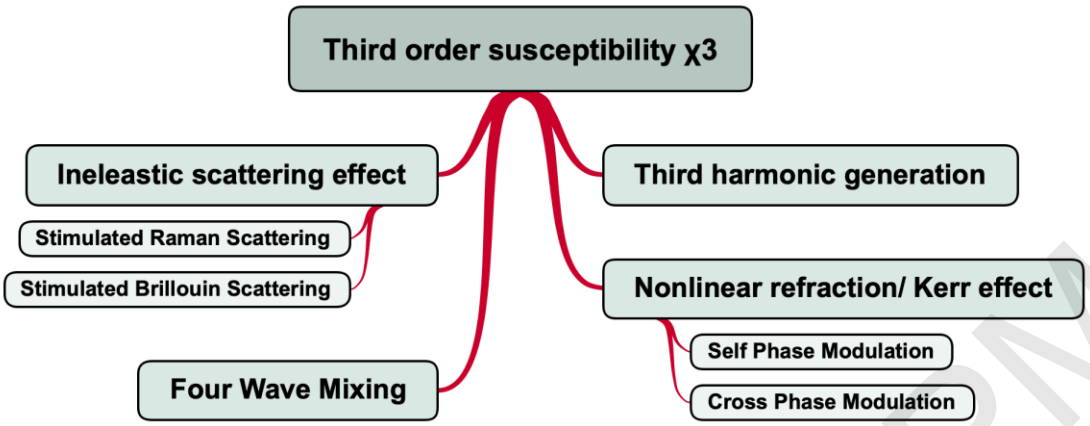

Figure 2.2 : Types of Third Order Susceptibility Ref: [31]

Figure 2.2 depicts various types of nonlinear effects classified under the category of third-order susceptibility (χ^3) in optical fibres. These effects, predominantly governed by third-order susceptibility, exert a significant influence on the behaviour of light waves as they propagate through the fibre. Some of the nonlinear effects depicted in this figure may include phenomena such as four-wave mixing (FWM), Stimulated Raman Scattering (SRS), Stimulated Brillouin Scattering (SBS), and other interactions that arise owing to the intensity-dependent properties of the fibre material.

2.2.1 Optical Kerr Effect

Nonlinear pulse propagation can arise from diverse effects, with the Kerr effect being a notable example. Fibre Kerr nonlinearity involves the alteration of the refractive index in an optical fibre in response to the incident light's intensity [32]. This phenomenon can induce distortion and signal degradation in optical communication systems, thereby restricting their capacities and ranges. To mitigate these effects, various digital signal processing techniques can be employed, including digital backpropagation, nonlinearity equalisation based on the Volterra series, nonlinearity

compensation grounded in perturbation theory, and phase conjugation. The basic equation for the Kerr effect in optical fibres can be expressed as follows [32]:

$$n = n_0 + n_2 I \,, \tag{2.1}$$

here, n represents the refractive index of the fibre, n_0 is the linear refractive index, n_2 stands for the Kerr coefficient, and I denotes the optical intensity. This equation elucidates the dependence of the refractive index on the optical intensity, which is a fundamental characteristic of the Kerr effect in optical fibres.

2.2.2 Self-Phase Modulation

SPM is a nonlinear optical phenomenon that arises when an ultrashort light pulse traverses a medium, eliciting a dynamic refractive-index change owing to the optical Kerr effect. This fluctuation in the refractive index induces a phase shift in the pulse, which ultimately alters its frequency spectrum [33]. The SPM arises from the pulse's inherent intensity modulation owing to the Kerr effect, contributing to phenomena such as spectral broadening and temporal compression. In optical fibre applications, SPM often has a predominant effect on ultrashort pulses, particularly under conditions of high peak power [34]. The SPM effect is encapsulated by the nonlinear Schrödinger equation (NSE), which encompasses both nonlinearity and dispersion terms. The comprehensive form of the NSE, accounting for both of these factors, is expressed as [35]:

$$i\frac{\partial A}{\partial z} + \beta_2 \frac{\partial^2 A}{\partial \tau^2} + \gamma |A|^2 A = 0, \tag{2.2}$$

where A is the pulse envelope, z is the coordinate along the propagation path, τ is the time variable, β_2 is the group velocity dispersion coefficient, and γ is the nonlinear

coefficient. When the dispersion term is removed from NSE, the equation is simplified to the basic SPM equation, for which a specific mathematical expression provides a solution. The simplified SPM equation is defined as [36]:

$$i\frac{\partial A}{\partial z} + \gamma|A|^2 A = 0, \tag{2.3}$$

The solution to this simplified SPM equation is expressed as [36]:

$$A(z,t) = A_0 \exp\left(i\emptyset(z,t)\right), \tag{2.4}$$

where A_0 is the initial pulse envelope and $\emptyset(z,t)$ is the phase of the pulse as it propagates through the nonlinear medium. This solution delineates the evolution of the pulse envelope, as it experiences SPM in the absence of dispersion effects. The phase of the pulse, denoted by ∅(z,t), undergoes changes as the pulse propagates, owing to the nonlinear interaction with the medium. This interaction results in spectral broadening and other nonlinear effects within the pulse. The spectral broadening resulting from the SPM can be described by the SPM equation, which provides a rough evaluation of the spectral broadening that the pulse experiences as it passes through the medium.The following formulas [36] can be used to estimate the spectral widening and chirp caused by SPM:

$$\Delta\boldsymbol{\omega_{SPM}} \approx \frac{\boldsymbol{P(z)\omega_0}}{\boldsymbol{\gamma\tau_0}}, \tag{2.5}$$

where $\Delta\omega_{SPM}$ represents the spectral broadening induced by SPM, $P(z)$ denotes the peak power of the pulse at position z, ω_0 signifies the central frequency of the input field, γ denotes the nonlinear coefficient, and τ_0 represents the input pulse width. This expression elucidates the relationship between spectral broadening due to SPM and parameters such as peak power, central frequency, pulse width, and nonlinear

coefficient [36]. The SPM effect promotes the expansion of the pulse bandwidth during its propagation through the medium, which results in spectral broadening and the appearance of new frequency components within the pulse.

2.2.3 Soliton Propagation

Soliton propagation is a phenomenon wherein a self-sustaining pulse of light, referred to as a soliton, traverses an optical fibre with minimal degradation. Solitons possess the remarkable ability to preserve their shape and energy over extended distances owing to the precise equilibrium between the influences of fibre dispersion and nonlinearity [37]. Soliton propagation plays a crucial role in optical communication by facilitating high-speed data transmission over extensive distances while minimising signal degradation [38]. Ultrafast fibre lasers with different cavity length parameters have produced a variety of soliton forms [39], such as dispersion-managed solitons [40], amplifier similaritons [41], DS [42] and conventional solitons (CS) [43]. These diverse soliton types offer versatile solutions for optimising optical communication systems [39].

A CS is a type of soliton characterised by distinct Kelly sidebands. These solitons typically emerge within the net anomalous dispersion regime, where a delicate equilibrium between the anomalous dispersion and nonlinearity is maintained. They are commonly distributed across the soliton spectrum [44], [45]. Sidebands are produced by constructive interference between the dispersive waves and the soliton pulse, which are then superimposed on the soliton spectrum. The overall cavity length, net dispersion, and pulse width can be estimated using these sideband positions [46].

Methods such as intracavity filtering have been implemented to address the challenges posed by sharp sideband generation. This technique aims to diminish the spectral sidebands without compromising pulse width. Furthermore, employing positive-dispersion fibres and other strategies to steer the soliton regime can effectively mitigate the adverse effects of sharp sideband generation [47]. While every soliton produced in a laser cavity experiences a unique pulse-shaping process influenced by nonlinear gain and loss, dissipative solitons are distinguished by pulses that experience significant energy dissipation within the cavity. They often take the form of up-chirped solitons generated in an all-normal or net-normal dispersion regime with high pulse energy. The interplay between gain, loss, dispersion, and nonlinearity is crucial for the formation of dissipative solitons [44], [45].

Temporal and spatial solitons are the two primary forms of solitons distinguished by their production methods. The relationship between pulse dispersion and refractive nonlinearity produces temporal solitons, whereas the relationship between nonlinearity and beam diffraction produces spatial solitons [48]. The mathematical formula for the temporal shape of soliton pulses can be expressed in terms of the sech^2 function, which describes the temporal intensity profile of the pulse. For a fundamental soliton, the temporal shape is that of an unchirped sech^2 pulse, given by [49]:

$$\boldsymbol{P(t) = P_p sech^2\left(\frac{t}{\tau}\right) = \frac{P_p}{cosh^2(\frac{t}{\tau})}}, \tag{2.6}$$

where P_p represents the peak power, τ denotes soliton pulse duration, and t represents the sech^2 fitted profile. The pulse energy E and soliton pulse duration, τ are required to satisfy the following conditions:

$$E = \frac{2|\beta_2|}{|\gamma|\tau}, \tag{2.7}$$

τ, is the soliton pulse duration and γ is the SPM coefficient in rad/ (W m) and β_2 is the GVD defined as derivative with respect to angular frequency.

2.3 Principle of Pulsed Fibre Laser Generation

2.3.1 Q-Switching

Q-switching is used to quickly change the cavity Q-factor from low to high to produce brief high-energy laser pulses. In fibre lasers, this process is typically accomplished by incorporating an optical modulator, such as an electro-optic or an acousto-optic modulator, into the laser cavity. In Q-switched lasers, a modulator is utilised to introduce significant loss into the cavity, effectively inhibiting lasing [50]. The population inversion within the laser medium is accumulated at a high level. When the modulator swiftly transitions to a low-loss state, the stored energy is discharged as a short, high-energy pulse. The cavity round-trip time and gain medium bandwidth determine pulse duration. Q-switched lasers can generate pulses with high peak powers and short durations, rendering them valuable for diverse applications including material processing, medical treatments, and light detection ranging systems.

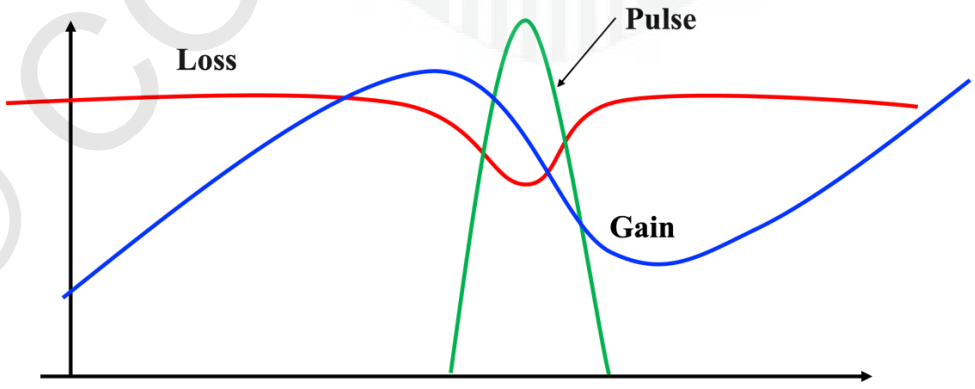

Figure 2.3 : Gain and Loss in the Passively Q-Switched Laser System [51]

The gain and loss dynamics of a passively Q-switched laser are shown in Figure 2.3 which emphasises how the SA modifies the intracavity losses to facilitate the creation of brief laser pulses via passive Q-switching. This mechanism was elaborated in [51]. The SA utilised in passive Q-switching introduces modulation of intracavity losses based on the intensity of the light passing through it. The modulation caused by the SA disrupts the relaxation oscillations, which involves periodic energy exchanges within the laser medium between the inversion and light fields [51]. The absence of a SA dampened these oscillations. Conversely, when the laser system experiences excess gain, the SA facilitates the rapid buildup of the light field.

The SA introduces losses that saturate based on the intensity of light, enabling the field intensity to increase until the gain saturates below the net loss. High-energy pulses are released because of this instability, which keeps the field intensity increasing as long as the gain is greater than the net loss. Short laser pulses (from nanoseconds to picoseconds) with high peak powers can be generated via Q-switching by adjusting the Q-factor (quality factor) of the laser resonator. The Q-factor, a dimensionless parameter, is defined as [52] :

$$Q = \frac{2\pi f_o \varepsilon}{P}, \tag{2.8}$$

where f_o is the resonant frequency, ε is the stored energy in the cavity, and $P = -\frac{dE}{dt}$ is the power dissipated.

2.3.2 Mode-Locked (ML) Fibre Laser

Mode locking is a technique used to generate ultrashort pulses in fibre lasers. It involves producing a train of incredibly short optical pulses by synchronising the

phases of the longitudinal modes of the laser cavity. This technique is essential for generating ultrashort pulses in the femtosecond and picosecond ranges and has numerous applications in fields such as spectroscopy, microscopy, and telecommunications [53]. In a mode-locked laser, the phases of different longitudinal modes are synchronised to generate short optical pulses with high peak powers. Figure 2.4 (a) illustrates the intensity versus time plot when the modes are perfectly locked. In such instances, the intensity profile demonstrates stable and periodic behaviour, leading to a well-defined pulse train with consistent characteristics. Conversely, Figure 2.4 (b) shows the intensity versus time plot when the relative phases of the modes are random. In this scenario, the intensity fluctuates randomly around its average value, resulting in an irregular intensity profile with fluctuations in the pulse train. The random phases of the modes introduce variability in the pulse timing and shape, thereby impacting the overall stability and coherence of the laser output.

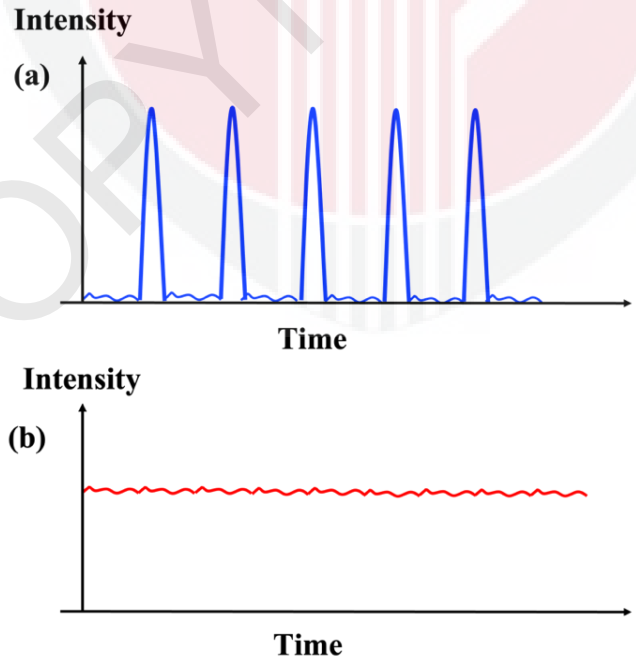

Figure 2.4 : Mode-Locked Laser Intensity: (a) Effectively Locked Phases; (b) Random Phases Ref: [51]

While passive mode-locking uses a SA to provide intracavity pulse modulation, active mode-locked pulses are generated by inserting an external loss modulator into the cavity. Figure 2.5(a) illustrates the active mode-locking in a laser featuring a gain medium and an optical loss modulator. Laser mode-locking is caused by the amplitude or phase modulation within the cavity of the optical modulator when an external signal is introduced. Figure 2.5 (b) shows that when the losses are low, the gain in the cavity can overcome them, thereby allowing the laser action to occur. Conversely, when the losses are high, the laser action is suppressed. This alternating pattern of high and low losses effectively imposes periodic modulation on the laser output, resulting in high pulse intensity [54]

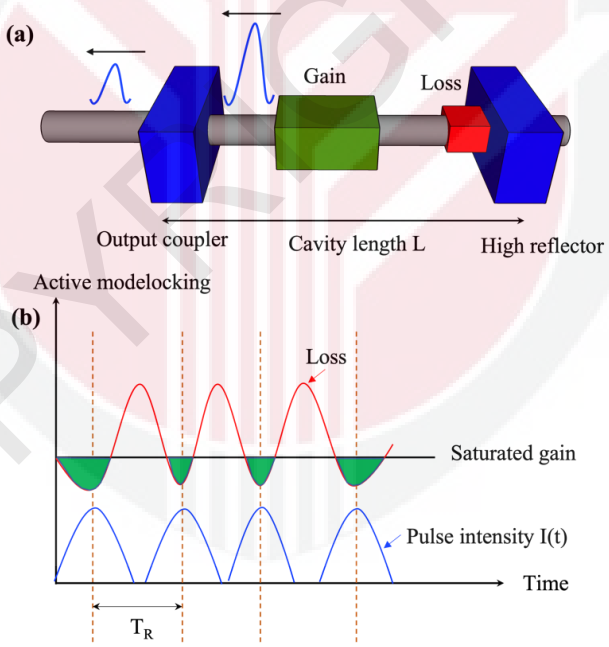

Figure 2.5 : Active Mode Locking (a) Resonant Cavity Mechanism (b) Modulating the Loss and Saturated Gain in the Cavity

The passive mode-locking mechanism produces a self-amplitude modulation of the field by inserting a discrete element or elements into the laser cavity. This includes shaping the pulses of a mode-locked laser using a passive SA. As illustrated in Figure

2.6. SA serves as a modulator in this procedure. When the loss modulation falls below the gain level, the pulse-envelope curvature becomes negative. This visually represents how the SA modulates the loss within the resonator, leading to the formation of ultrashort pulses. Additionally, the time dependence of the pulse and net gain is likely represented to illustrate the relationship between the pulse shape and the net gain within the laser cavity, highlighting the role of the SA in shaping the pulse and achieving mode-locking.

The inversion of the pulse envelope occurs at this point when the net gain and loss switch occurs. Comparatively speaking, mode-locking with a slow absorber is significantly harder to characterise than passive mode-locking with a rapid absorber. Analytical solutions were obtained using a basic approximation. When a window of the net gain opens, the leading edge of the absorber saturates the pulse. Next, gain saturation closes this window, creating a net loss decrease window that resembles that of a rapidly saturable absorption. The hyperbolic secant temporal envelopes of the electromagnetic field are the outcomes of this process [55].

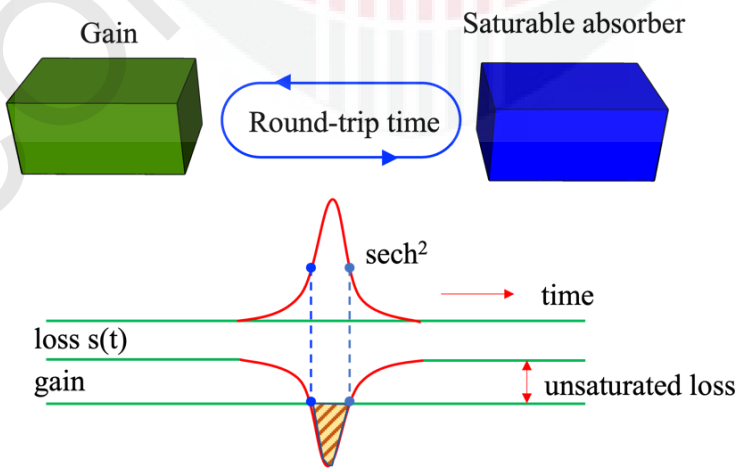

Figure 2.6 : Diagram of Passively Mode-Locking with Fast Saturable Absorber, Time Dependence, and Gain Ref: [55]

Steady-state ML is obtained when the absorption is partially saturated, and the gain recovers the initial value in the successive trip before the arrival of the following pulse. Additionally, absorption of the SA is inversely proportional to the laser intensity. Thus, passive ML depends on the effects of the pulse energy, pumping rate, cavity loss, and saturation energy of the gain and saturable absorption. The recovery times for both quantities determine the mode-locked pulse interval. Typical SA parameters that are considered crucial in SA fabrication are the saturation fluence, operating wavelength range, modulation depth, nonsaturable loss, and recovery time. The pulse formation process is complicated, in which fluctuations in spontaneous emission are increased by the SA during the number of round trips until the intense pulse saturates the SA. The pulse continued to shorten until the spectral width exceeded the gain bandwidth. For a fibre laser, the GVD and SPM have a vital effect on the formation of mode-locked pulses, and the theory of ML is highly based on the nonlinear Schrödinger equation. Laser light is usually collected as brief pulses around the minimal loss modulation using an intracavity loss modulator, with a period determined by the cavity round trip time [56]:

$$\mathrm{T}_R = \frac{2L}{V_g}, \tag{2.9}$$

where V_g is the group velocity and L is the length of the laser cavity (that is, the propagation velocity of the peak of the pulse intensity). Under certain circumstances, the repetition rate can be an integer multiple of the basic repetition rate. This phenomenon is referred to as harmonic mode-locking.

2.3.3 Saturable Absorber Structure and Deposition Techniques

2.3.3.1 Fundamental and Properties of Saturable Absorber

A SA device is usually integrated into a laser cavity to accomplish passive mode locking, as stated previously. The light entering the SAs is linearly absorbed up to a predetermined threshold intensity. When the material reaches this threshold, it saturates and is almost completely transparent to incident light [57]. When high-energy photons impact a material with a bandgap, they excite electrons from the valence band to the conduction band, as shown in Figure 2.7 (a). These electrons become hot Fermi–Dirac electrons owing to their rapid energy absorption. Figure 2.7 (b) illustrates the rapid transition of these hot electrons to a thermal equilibrium state facilitated by intraband scattering. During this process, energy is exchanged among the electrons, establishing a distribution of hot carriers. Figure 2.7(c) shows that, at sufficiently high light intensities, there was a dramatic increase in the number of photogenerated carriers. The Pauli-blocking effect is caused by this increase in the carrier population, which fills the states in the conduction band close to half of the photon energy. This effect effectively prevents further absorption of photons.

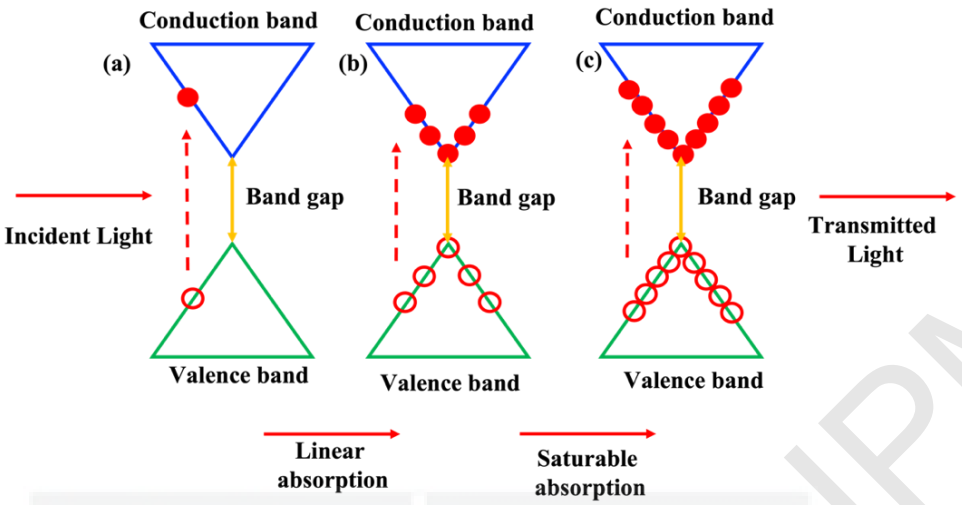

Figure 2.7 : Pauli Blocking Effect-Induced Linear Absorption and Saturable Absorption Processes (a) Illustrates the Photon Excitation of Electrons to the Conduction Band, Forming Hot Fermi–Dirac Electrons, (b) Rapid Electron Thermalization via Intraband Scattering, Establishing a Hot Carrier Distribution, and (c) an Increased Carrier Population at High Light Intensities, Triggering the Pauli Blocking Effect. Ref: [58]

In the context of SA, the modulation depth represents the maximum change in absorption induced by the incident light at a specific wavelength. The SA can effectively shape a pulse with a higher modulation depth, leading to shorter pulse durations and dependable self-starting, which makes this parameter essential for developing passively mode-locked lasers. The following formula [59] can be used to calculate the nonlinear absorption behaviour of a saturable absorber, which varies with the intensity of the incident beam:

$$\boldsymbol{T(I) = 1 - \alpha_{ns}\ - \Delta T\ \times\ \exp\left(\frac{-I}{I_{sat}}\right)} \qquad (2.10)$$

where, $T(I)$, α_{ns}, I_{sat}, and ΔT denote the nonlinear transmittance, non-saturable loss, saturation intensity, and modulation depth, respectively. An example of a nonlinear transmission curve for a saturable absorber is shown in Figure 2.8. The ΔT is

determined by calculating the transmission difference between the nonsaturable loss and background absorption loss (α_o).

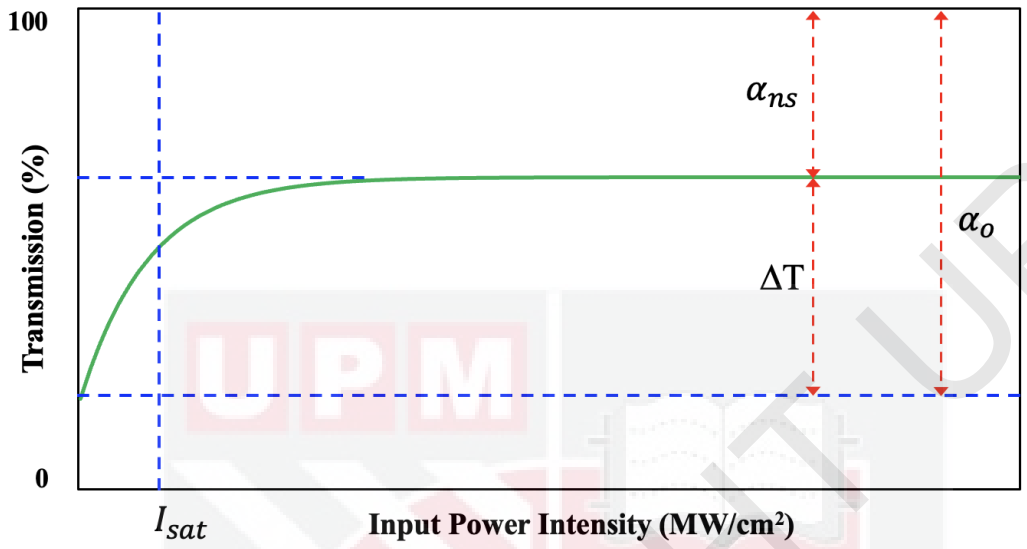

Figure 2.8 : Example of a Nonlinear Transmission Curve for Saturable Absorber

Jeon [36] conducted a numerical study to determine the minimum modulation depth of a SA for producing steady optical pulses from a passively mode-locked fibre laser cavity [59]. According to the study, for a dispersion lower than -0.08 ps^2, the minimum modulation depth needed varied between 1.5 and 2.5 percent in the anomalous dispersion regime. According to Liu et al. [60], SAs with a large modulation depth, particularly in laser cavities with near-zero cavity GVD, can contribute to stabilising the mode-locking operations in pulsed lasers. According to Lee et al. [62], there is an inverse relationship between the ΔT and temporal width, because a ΔT of the SA produces shorter pulse widths in mode-locked pulses. The findings from [63] suggest that in materials with high crystallinity, a smaller bandgap results in a more perfect crystal lattice and well-defined electronic structure.

This results in a higher carrier mobility and lower defect density, consequently leading to a stronger nonlinear response and resulting in a higher ΔT compared to the amorphous state [63]. Several studies have explored the impact of increasing material thickness or concentration on the properties of SAs. For instance, higher concentrations of CNT have been found to increase the absorption of CNT absorbers [64]. Several studies have explored the impact of increasing material thickness or concentration on the properties of SAs. For instance, higher concentrations of CNT have been found to increase the absorption of saturable CNT absorbers [64]. In contrast, Huang et al. [65] reported a lower α_s with increasing thickness of the graphene layer. Nevertheless, the author suggests that a thicker graphene layer should yield higher α_s. Further investigations may be necessary to reconcile these conflicting observations and establish a clearer understanding of the relationship between I_{sat} and graphene/PMMA layer thickness.

2.3.3.2 Fibre Ferrule Structure

The fibre ferrule structure offers a straightforward SA configuration, providing convenient fibre compatibility and flexibility. Figure 2.9 illustrates the fibre ferrule configuration diagram. The material for this structure is either deposited on the fibre end facet to act as the SA, or it is integrated between two fibre ferrules utilising a fibre connector in a sandwich configuration. Various techniques for depositing material onto a fibre ferrule have been proposed, including the mechanical exfoliation of indium tin oxide (ITO) powder onto the fibre ferrule [66], where the flrpic/PVA thin film can be transferred between two fibre ferrules [67]. Another method involves immersing the fibre connector for physical contact in a graphene solution with a continuous wave laser [68]. However, there are a number of drawbacks to the fibre

ferrule SA structure, such as laser scattering, weak absorption owing to the material's short interaction length, and mechanical and thermal damage from the direct contact of the fibre ferrule with the SA material particularly at high power [69]

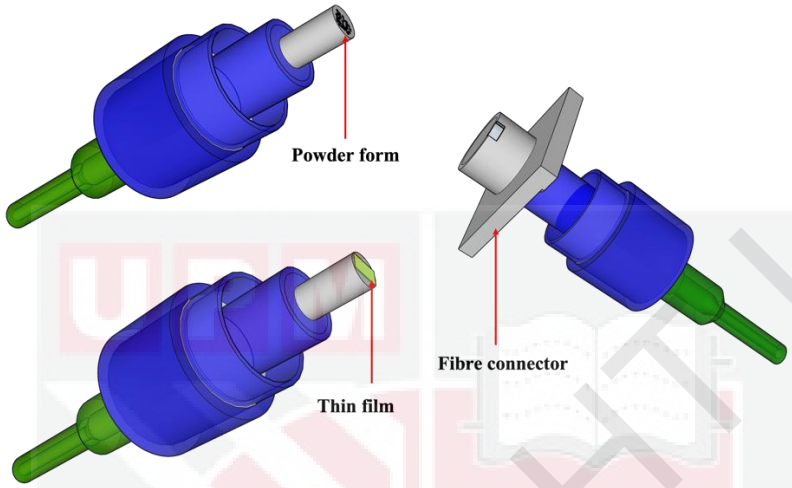

Figure 2.9 : Fibre Ferrule Techniques for SA in Both Powder and Thin Film Forms

2.3.3.3 D-Shaped Fibre Structure

Figure 2.10 shows a typical D-shaped fibre structure diagram. Several methods of material deposition on D-shaped fibres have been demonstrated, such as mechanical exfoliation of rhenium disulfide on the D-shaped fibre [70], drop casting with a Cadmium Telluride (CdTe) solution [71], film attachment [72] and optical deposition of nanosheet dispersion using a continuous wave laser with in-situ optical loss monitoring [73]. Furthermore, the D-shaped fibres have a robust structure as compared to a tapered fibre [74]. However, the asymmetrical design of the fibre cross-section inherently renders D-shaped fibres to be polarisation-sensitive. This can lead to polarisation-dependent losses (PDL), potentially affecting the overall performance of the system, especially in applications requiring precise polarisation control [75]. On

the other hand, transverse electric (TE) and transverse magnetic (TM) dominate, this selective interaction can supress unwanted polarisation states and it limits the ability of D-shaped fibre SA to produce PDL [76].

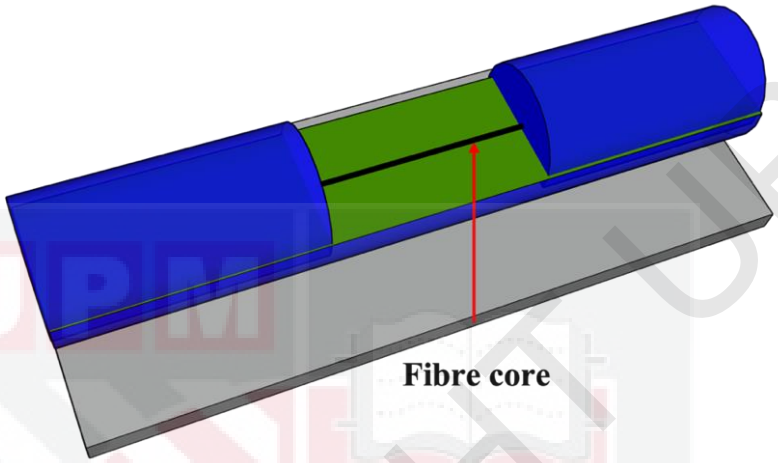

Figure 2.10 : D-Shaped Fibre with Material Deposition

2.3.3.4 Tapered Fibre

A traditional SMF is stretched to produce a reduced core diameter shape at the narrowest point, referred to as the waist, to produce tapered fibres. The waist functions as a transitional region as the SMF tapers down to the micrometre scale, with decreasing cladding and core sizes. Heating a brief segment of the fibre while concurrently pulling its two ends is the usual process for creating tapered fibres, as illustrated in Figure 2.11. Various heat sources can be employed for this technique, such as gas burner flames [77], high-power laser radiation [78], and arc discharge [79]. In addition to the tapered length, other factors such as waist diameter, and refractive index (RI) are equally important in influencing the optical properties of tapered fibres. Tapered fibres are generally categorised into two types: adiabatic and non-adiabatic.

Compared to nonadiabatic techniques, the adiabatic fibre tapering method ensures minimal transmission loss and intermodal coupling in tapered fibres [80].

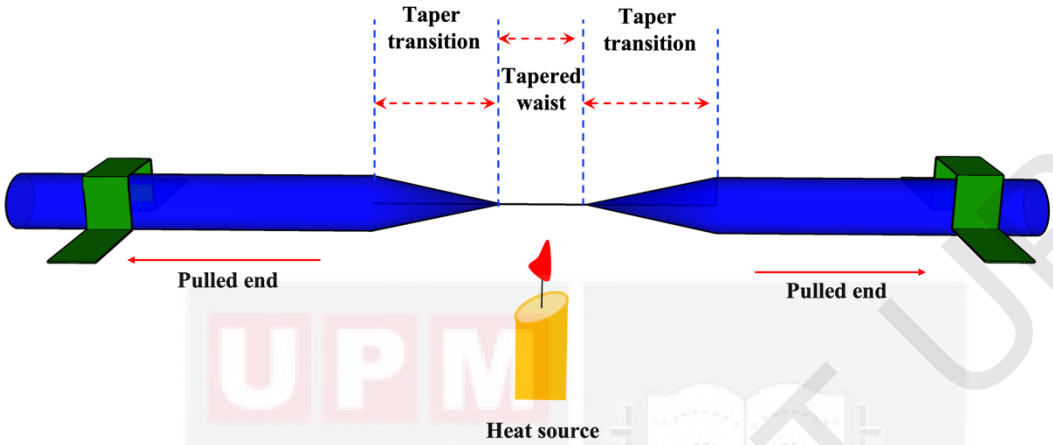

Figure 2.11 : Schematic Illustration of the Flame Approach Used for Fabrication of the Tapered Fibre. Ref: [81]

The evanescent field refers to the portion of the light wave that extends into the cladding material and diminishes exponentially away from the interface between the core and the cladding. Factors such as the angle of incidence, refractive indices of the cladding and core, and light wavelength affect the strength of the evanescent field [82]. The extent to which the evanescent field penetrates into the cladding material, denoted as the depth of penetration d_p is associated with the angle of incidence θ, the refractive index of the core n_1 and cladding n_2, and the wavelength of light λ, as:

$$\boldsymbol{d_p = \frac{\lambda}{2\pi\sqrt{n_1 sin^2\theta - n_2^2}}}, \tag{2.11}$$

Figure 2.12 illustrates the principle of optical evanescent-field deposition of material nanocomposites. One of the primary advantages is the robust interaction between the tapered fibre and its surrounding environment, which enables a high sensitivity to environmental changes. The evanescent field refers to a non-propagating

electromagnetic field present outside the fibre, which diminishes exponentially as the distance from the fibre surface increases [83]. The tapered fibre exhibits a robust evanescent field, facilitating an enhanced interaction between the fibre and its surrounding material. This characteristic renders it a suitable platform for the fabrication of SAs. The mode-locked fibre laser performance has been significantly improved by the use of tapered fibres in the construction of SAs. Compared with other SA designs, tapered fibre SAs exhibit better modulation depths, faster response times, and larger spectral bandwidths [84].

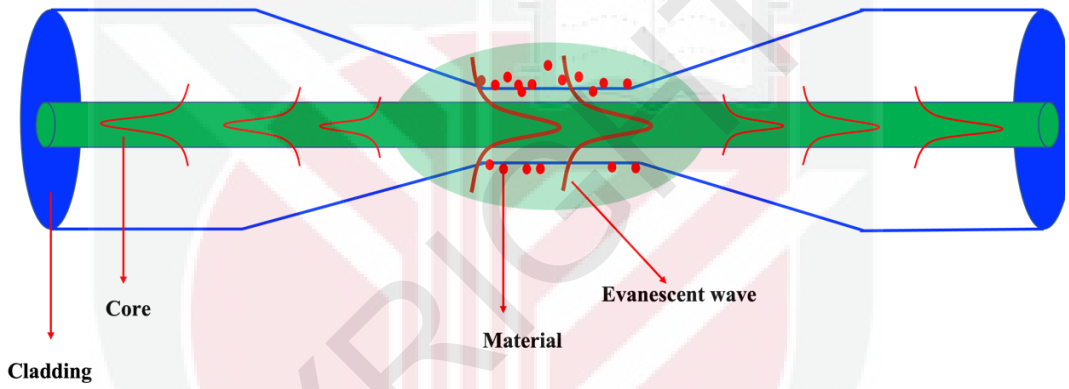

Figure 2.12 : Principle for Optical Evanescent-Field Deposition of Nanocomposites. Ref: [83]

The interplay between the evanescent field of a tapered fibre and a material in close proximity to its surface can change the optical characteristics of the material, such as adjusting its refractive index or absorption coefficient [83]. The degree of interaction between the evanescent field and the material is contingent upon both the distance between the fibre surface and the material, and the intrinsic properties of the material. For instance, materials with a higher refractive index exhibit a more pronounced interaction with the evanescent field than materials with a lower refractive index. This occurs because the evanescent field penetrates deeper into the surrounding medium when the refractive index of the medium closely matches that of the fibre.

Nonetheless, it is crucial to acknowledge that employing materials with high refractive indices may lead to augmented losses within the fibre caused by scattering and absorption. These factors can potentially reduce the overall effectiveness of the sensing system [83].

2.4 Material-Based Tapered Fibre Saturable Absorber

The adoption of tapered fibres as SA devices in fibre lasers has attracted significant attention in recent years. Table 2.1 compares recent studies that investigated tapered fibre SAs using various materials. This approach encompasses a wide range of materials including metals, metal oxides, metal dichalcogenides, Metal-Organic Frameworks (MOFs), and MXenes. Various techniques exist for depositing materials onto tapered fibres, as outlined in table. These methods include optical-induced deposition using a continuous-wave (CW) laser, spin-coating with a composite, magnetron sputtering, and drop-and-dry solutions.

The most commonly used tapered fibre deposition technique presented in the table was optical-induced deposition [85], [86], [87], [88], [89]. This process involves the application of a suspension containing the material around the waist of the tapered fibre. When the laser beam passed through the tapered fibre, the material reacted by moving in the direction opposite to that of the light transmission, thereby facilitating the attachment of the material onto the surface of the tapered area. This process effectively creates a coating of the proposed material around the waist region. The insertion loss of the tapered fibre SA was measured both before and after the deposition process. This technique allows precise control, ensuring that deposition ceases once the insertion loss reaches 3 dB, as outlined in [86]. The optical deposition

method discussed in [64] involves directly depositing CNTs onto the surface of tapered fibres. However, this process can lead to significant scattering losses, thereby limiting the interaction length unless larger waist diameters of tens of micrometers are employed.

Additionally, SA created through optical deposition are vulnerable to environmental exposure, resulting in rapid degradation, rendering them unsuitable for various practical applications. A similar optical deposition technique was proposed by [19], in which Telluride (Te) solutions were dropped and dried on a tapered waist region. The material attachment along the tapered fibre was then observed under a microscope. Finally, a low-refractive-index polymer was dropped onto the tapered fibre to act as an adhesive for the Te solution, which then became the SA. Even though Te nanowires [19] were evenly covered on the tapered fibre surface to form the Te-SA, achieving uniform and consistent coverage would be difficult in large-scale production. This approach offers several advantages over spray-coating and optical deposition techniques, including long-term reliability by protecting the tapered fibre from environmental factors, improves dispersion of CNTs in the polymer matrix, reduced scattering losses, and minimised bundling and agglomeration of CNT [64]. However the spin coating techniques with material and polymer suffers on controlling the material-polymer thickness on to the embedded tapered fibre SA. Therefore, the spin-coating deposition technique was proposed by [21] to optimise the thickness around the waist region, to ensure the optimum thickness of the black phosphorus/polydimethylsiloxane composite, and to guarantee the reproducibility of the SA. Based on the findings of [21], the SA fabrication process employed a spin-coating method for material deposition on a tapered fibre. PDMS was chosen as the

supporting material for NiO owing to its low refractive index (1.413), high adsorption capacity, and flexibility, as referenced in [90].

Furthermore, the spin-coating technique provides robust support for the delicate tapered region on the SA substrate [91] [92] [182] where the proposed material is attached to a low-refractive-index polymer. Simultaneously, the composite serves as a protective barrier, shielding the SA material from exposure to oxygen and humidity. In contrast to the spin-coating technique, magnetron sputtering [93], which is similar to the spray coating, involves the deposition of a thin film by bombarding a material target with high-energy ions. This leads to uniform condensation in the waist region of the tapered fibre. Careful optimisation of the deposition duration strikes a balance between the ΔT and α_{ns} [93]. It is important to note that this technique may require specialised equipment and conditions, and may not be suitable for all materials or applications.

The dimensions of tapered SA fabrication varied across studies, with fabrication techniques employing a tapered fibre machine. For instance, Chen et al. [86] proposed a fabrication dimension of tapered fibres as low as 6 µm, whereas [94] proposed a value as high as 16.5 µm. The evanescent field is high because light is tightly confined within the fibre core, despite the fragile structure caused by the thinner taper in small-diameter fibres. Additionally, the field extends further into the surrounding medium owing to the small size of the fibre [83]. According to [64], thinner tapers enable a higher proportion of the light pulse to penetrate the evanescent field, thereby making it more strongly influenced by the SA material. A decrease in diameter enhances the capacity of the SA to interact with incident light, intensifying the absorption process.

Moreover, increasing the interaction length of the tapered fibre allows light waves to interact with the material over longer distances [95]. However, the insertion loss of SAs can be increased using these methods. Achieving a compromise between minimal insertion loss and high ΔT requires determining the optimal length and waist diameter of the tapered fibre [17].

Table 2.1 : Latest Tapered Fibre Based SA Reported from 2022-2024

No	Year	Material	Deposition method on tapered fibre	Dimension tapered fibre	Laser Cavity Type	ΔT (%)	Saturation intensity (MW/cm^2)	Non-saturable loss (%)	Pulse performance	Ref.
1	2024	Iron Oxide Hydroxide (FeOOH)	Optical induced deposited	Diameter-N/A Length- N/A	EDFL/YDFL	YDFL-1.26 EDFL-2.61	YDFL-4.01 EDFL-7.16	YDFL-82.3 EDFL-89.5	YDFL-NLP-519 fs EDFL-Soliton-1.02 ps	[180]
2	2024	Vanadium Selenide (VSe_2)	Optical induced deposited	Diameter-10 µm Length- N/A	EDFL	1.12	710.00	58.00	Soliton- 680 fs	[181]
3	2024	Cerium oxide (CeO_2)	Spin coated- PDMS polymer composite	Diameter-10 µm Length-N/A	TDFL	3.40	44.00	54.00	Soliton- 1.49 ps	[182]
4	2024	Germanium Antimony Telluride ($Ge_2Sb_2Te_5$)	Optical induced deposited	Diameter-N/A Length- N/A	EDFL	6.69	109.71	52.00	Soliton-780 fs	[183]
5	2023	nickel 1,3,5-benzene-tricarboxylic acid (Ni-H_3BTC)	Spin coated- PDMS polymer composite	Diameter-10 µm Length-60.5 mm	EDFL	4.50	30.30	48.40	NLP- 148 fs	[91]
6	2023	InSb	Magnetron sputtering deposition method	Diameter-15 µm Length -1 cm	EDFL	1.93	7.84	51.57	Dissipative soliton 25.14 ps 14.91 MHz	[93]
7	2023	α-Al_2O_3	Spin coated- PDMS polymer composite	Diameter-10 µm Length-62 mm	TDFL	4.08	21.67	49.80	NLP- 198 fs	[92]

Table 2.1 : Continued

8	2023	Niobium disulfide NbS_2	Optical-induced-deposition	Diameter-13 µm Length- N/A	EDFL TDFL	10.20	0.46	55.30	EDF-Soliton-753 fs TDF- Soliton-5.77 ps	[85]
9	2022	Te (tellurium nanowires)	Solution drops and dry- UV curable adhesive	Diameter-10 µm Length- 8 mm	EDFL	27.00	8.90	54.90	Soliton 621 fs	[19]
10	2022	Perovskite Oxide (Ba_2LaTaO_6)	Optical induced deposition	Diameter- 16.25 Length- N/A	EDFL	24.00	2.66	54.00	Soliton-1.06 ps 12.3 MHz	[94]
11	2022	WSe_2	Optical induced deposition	Diameter - 6 µm Length - 600 µm	EDFL	15.00	100.58	41.50	Soliton-390 fs 24.5 MHz	[86]
12	2022	Ti_3C_2 Mxene	Optical induced deposition	Diameter-13 µm Length-10 mm	EDFL	4.80	183.00	91.60	Soliton- 1.18 ps DSR- 8.13 ns Repetition rate – 7.38 MHz	[87]
13	2022	Indium selenide (InSe) nanosheets InSe-Au	Optical induced deposition	Diameter-10 µm Length-10 mm	EDFL TDFL	7.18	63.41	52.22	EDF- 507 fs TDF- 2.51 ps Repetition rate- 19.17 MHz	[88]
14	2022	Vanadium carbide (V_2C)	Optical deposition method	Diameter- N/A	EDFL YDFL	1 µm - 18.3 1.5 µm- 20.2	1 µm- 81.4 1.5 µm- 100.2	70.00	EDF- 311 ps YDF- 571 ps Repetition rate- 18.22 MHz	[89]

Note: N/A = not applicable, EDFL = erbium doped fibre laser, YDFL = ytterbium doped fibre laser , TDFL = thulium doped fibre laser, NLP= noise like pulse

2.5 Development of Nickel-Based Saturable Absorber

2.5.1 Nickel Metal and Nickel Oxide Properties

Recent advancements in Ni-based materials have been reported in various forms, including pure nickel [96], metal oxides [97], TMD MOF [98], and ternary dichalcogenides [99]. This study examines the properties of Ni and NiO. Nickel, a ferromagnetic element found naturally in the Earth's crust as oxides and sulfides, is classified as a non-noble metal with localized surface plasmon resonance (SPR) properties [100]. Larger Ni particles enhance scattering-to-absorption efficiency and cause a red shift in the SPR peak [101][102]. However, due to their magnetic nature, nickel nanoparticles (NiNPs) tend to cluster, necessitating specialised techniques to achieve monodisperse particles [103].

Ni demonstrates notable linear optical properties, including high absorption in the visible and near-infrared regions, with absorption characteristics distinct from those of iron material [104]. Despite its potential, the NLO properties of transition metals, particularly Ni have been relatively underexplored, with only limited studies available [105]. One key nonlinear behavior observed in Ni is reverse saturable absorption (RSA), attributed to the two-photon absorption (TPA) process in nickel films. Studies by Zhang et al. [105] and Ganeev et al. [106] in the femtosecond regime confirmed the RSA behavior of nickel, also linked to TPA. Materials with positive and negative nonlinear absorption coefficients, such as Ni, are highly promising for optical limiting and saturable absorber applications. The TPA properties of Ni make it especially effective in optical limiter devices, where it helps absorb intense light, offering protection for optical detectors, sensors, and even human eyes.

Furthermore, Ni is a suitable alternative to expensive noble metals. However, plasmons in ferromagnetic materials generally exhibit stronger damping than noble metals such as gold. Few studies have been conducted on the comparatively modest SPR effects of Ni, gold (Au), and silver (Ag) nanoparticles. It should be noted that the polarisability of nickel is weaker than that of conventional noble metals, such as gold and silver. Because polarisability is dependent on the number of free electrons, nickel has fewer electrons than gold, leading to weaker surface plasmon resonances [107]. Kho et al. [108] investigated nickel catalysts for NIR absorption. The UV-VIS-NIR absorption spectra of the corresponding catalysts showed that Ni with single-phase oxides had higher light absorption capabilities in all three areas (UV, visible, and NIR).

Similarly, research shows that NiO exhibits both saturable absorption and RSA depending on the sample preparation and doping elements. Pristine NiO thin films display SA behavior, while RSA is observed after annealing, which is attributed to indirect TPA processes [109]. Additionally, the refractive index nonlinearity of NiO is significantly influenced by the oxygen partial pressure during deposition, with higher pressures enhancing the material's nonlinear optical response [110]. Furthermore, NiO can be used as effective Hole Transport Material (HTM), improving solar cell efficiency by extracting positive charges and reducing carrier recombination [111]. Its high contrast ratio, coloring efficiency, and stability make it a desirable electrochromic material [112]. Additionally, p-type NiO's ability to adsorb and ionize oxygen molecules enhances its gas sensing performance [113]. The electronic and optical properties of NiO, including conductivity, bandgap energy, and light

absorption, are influenced by crystal defects. These properties can be tailored through doping or adjusting deposition conditions for specific applications [114], [115].

2.5.2 Nickel-Based Material as Saturable Absorber

Table 2.2 presents a recent study highlighting the performance of Ni-based materials/composites as SA particularly in EDFL. Ni-based materials have been reported in diverse forms, including Ni-metal, Ni-metal oxides, Ni-TMDs, Ni/NiO-MOFs, and Ni-ternary chalcogenides. The literature generally identifies two distinct SA techniques: tapered fibre and fibre ferrule techniques, particularly for pulse lasers operating in the 1.55 μm spectral range. Ni/PVA [12], NiO/PEO [16], NiO/chitosan [14], Ta_2NiS_5 [116], and $NiPS_3$ [117] have been demonstrated in a fibre ferrule SA structure by sandwiching a thin film between two fibre ferrules. The SA thickness plays a critical role in its performance. A layer that is too thin may not provide sufficient absorption, leading to a lower ΔT [118]. Conversely, if the SA layer is too thick, it may result in excessive absorption loss, thereby limiting the effectiveness of SA. Consequently, fibre ferrule techniques exhibit weak absorption owing to their shorter interaction lengths, leading to a higher mode-locked threshold [17].

Tapered fibre techniques on Ni-based materials have been utilised by several researchers, including those employing NiS_2 [119], $NiTe_2$ [120], Ni-H_3BTC-MOF/PDMS [121], and NiO-Co_3O_4 [122]. Among these, the work on NiS_2 [119] demonstrated the lowest mode-locked threshold of 37 mW compared to the other tapered fibre SAs listed in the table. The lower saturable intensity of 6.8 MW/cm² in NiS_2 [119], as mentioned in [123], may contribute to reducing the mode-locked threshold rather than other influencing factors. Concerning the pulse performance, a

study utilising NiS_2 [119] achieved the shortest pulse duration of 524 fs with 30% ΔT, implemented alongside the shortest cavity length design with the highest repetition rate of 22.45 MHz. Although NiO/PEO [16] achieved an impressive ΔT of 39%, the pulse width was limited to 950 fs. This difference could potentially be attributed to the suboptimal cavity design in their experiments, which is influenced by factors such as cavity losses, gain medium properties, and SA properties.

The tapered fibre SA technique is well known for providing an extended nonlinear interaction length. Variations in tapered fibre geometry were observed among the tapered fibres, resulting in different waist diameters. For instance, NiS_2 [119] was fabricated with a waist diameter of 4.5 µm, NiO-Co_3O_4 [122] with 9 µm, and $NiTe_2$ [120] and Ni-H_3BTC-MOF/PDMS [121] with 10 µm. The waist diameter is a crucial parameter for the light interaction with surrounding materials through evanescent wave propagation. The thinner the waist diameter, the stronger the penentration depth of the evanescent wave. As a result, the light absorption is enhanced that lead to a larger value of ΔT [64]. However, having a tapered fibre with an excessively thin waist diameter can present drawbacks, notably in terms of the fragility of the fibre and the challenges encountered during the SA fabrication process which requires meticulous care and precision. Therefore, in order to address the performance of tapered fibre-based SA and its fragility, a balance approach is required. In this case, the waist diameter cannot be too thin, but at the same time, its NLO properties are satisfactory to generate ultrashort pulses.

Table 2.2 : Development of Ni-Based Materials as SA for Q-Switched and Mode-Locked in EDFL Cavity

Ni-based Composites	Nickel-based Composite SAs	Method of SA depositions	SA types	Laser types	Threshold power (mW)	Centre wavelength (nm)	Repetition rate	Pulse width	ΔT (%)	Pulse energy (nJ)	Ref
Ni-Metal	Ni/PVA	Thin film-Sandwiched	FF	QS	85.0	1563.10	56.79 kHz	1.50 µs	15.00	4.33	[12]
Ni-Oxide	NiO/ Chitosan	Thin film-Sandwiched	FF	QS	104.9	1562.00	42.66 kHz	2.02 µs	11.50	15.30	[14]
	NiO/PEO	Thin film-Sandwiched	FF	ML	98.0	1561.80	0.96 MHz	950 fs	39.00	1.14	[16]
Ni-TMD	NiS_2	Optical deposition	TF	ML	37.0	1560.20	21.10 MHz	524 fs	30.80	1.86	[119]
	NiS_2/PVA	Thin film-Sandwiched	FF	QS	25.6	1564.80	85.5 kHz	5.85 µs	3.50	114.70	[124]
	$NiTe_2$	Optical deposition	TF	ML	125.0	1567.30	22.45 MHz	1.07 ps	0.70	0.17	[120]
Ni-MOF	Ni-H_3BTC-MOF/ PDMS	Spin-coating	TF	ML	56.5	1557.72	10.00 MHz	907 fs	5.20	1.30	[121]
NiO-MOF	NiO-Co_3O_4	Optical deposition	TF	ML	54.3	1554.40	4.84 MHz	1.61 ps	5.60	-	[122]
Ni-Ternary chalcogenides	Ta_2NiS_5	Nanosheet-Sandwiched	FF	ML	150	1569.00	2.92 MHz	1.45 ps	11.95	72.11	[116]
	$NiPS_3$	Nanosheet-Sandwiched	FF	QS & ML	40-QS 440- ML	1564.60	5.117 MHZ-ML	8.52 µs -QS 6.52 ns	4.60	4.46	[117]

Note: QS = Q-switched pulse, ML = mode-locked pulse, FF = fibre ferrule, TF = tapered fibre, TMD = transition metal dichalcogenide, MOF = metal organic framework

2.6 Summary

The objective of this chapter is to provide a comprehensive review of the literature related to nonlinear pulse propagation, principles of pulse fibre lasers, mode-locked pulse fibre lasers, material-based tapered fibre SA, and the development of nickel-based SA. A literature review revealed that nonlinear pulse propagation is a complex phenomenon that involves the interaction between light and the medium through which it propagates. The performance of optical communication systems can be limited by nonlinear processes such as SPM, GVD, and four-wave mixing, which can also result in pulse distortion.

In pulse fibre lasers, mode-locking is a technique used to generate ultrashort pulses. This technique involves the use of a SA that allows the laser to operate in a mode-locked regime, producing pulses with durations in the femtosecond range. Material-based tapered fibre SAs have shown to be an effective mean of achieving mode-locking in fibre lasers owing to their high nonlinearity and ease of fabrication. Additionally, the development of Ni-based SAs has been reported in the literature. These SAs have demonstrated promising results in the production of ultrashort pulses for fibre lasers. These SAs have the advantage of operating at high repetition rates, making them attractive for applications such as frequency-comb generation and time-resolved spectroscopy.

CHAPTER 3

Ni METAL/PDMS AS SATURABLE ABSORBER FOR NET DISPERSION MANAGEMENT ON EDFL PERFORMANCE

3.1 Overview

This chapter focuses on the preparation and characterisation of a nickel-polydimethylsiloxane (Ni/PDMS) composite as a light absorbing material for the purpose as a SA. This device is integrated into a mode-locked erbium-doped fibre laser (EDFL) cavity to generate ultrashort pulses. This chapter begins with the fabrication of the Ni/PDMS composite and its subsequent material characterisation. Next, the Ni/PDMS-SA preparation, characterisation, and deposition processes are discussed thoroughly. The setup of the mode-locked EDFL cavity with Ni/PDMS-SA is demonstrated, and optimisation of the net dispersion to achieve the shortest pulse is presented and discussed in detail. This discussion provides insight into the potential use of Ni/PDMS as SA material in mode-locked EDFLs. The flowchart of the methodology for this chapter as illustrated in Figure 3.1.

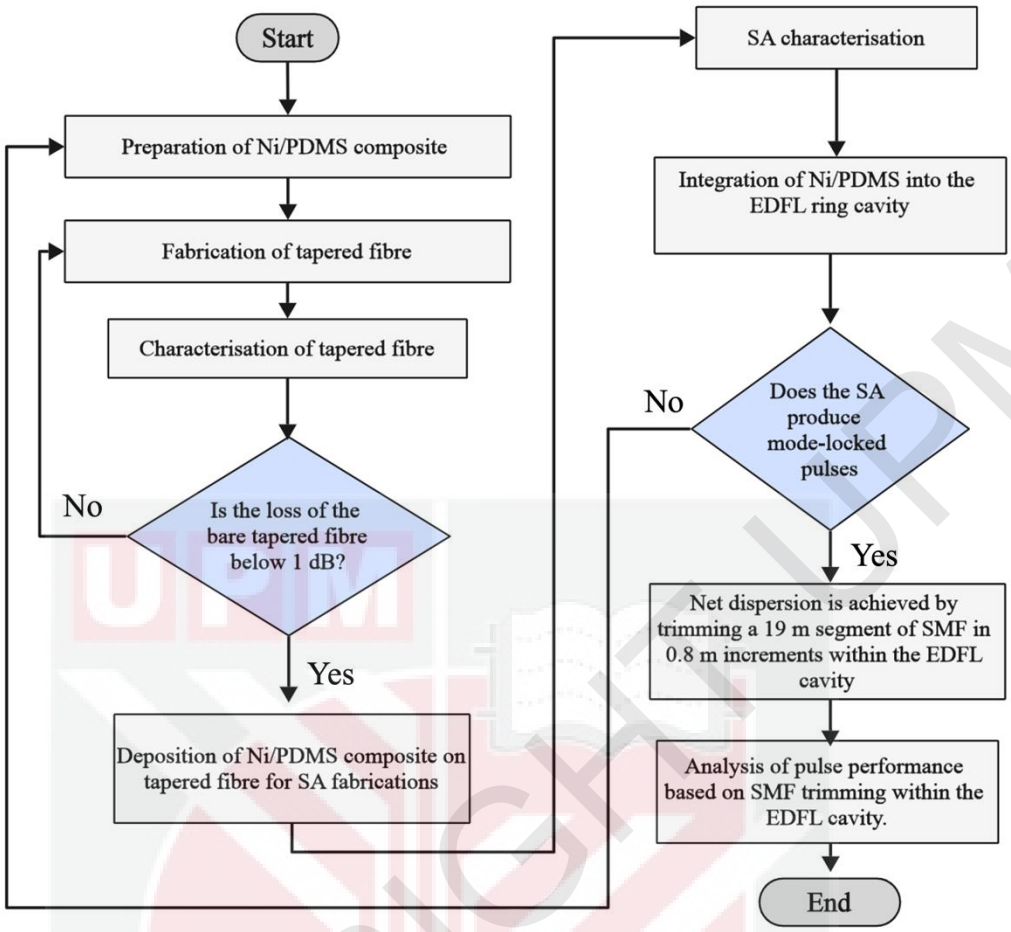

Figure 3.1 : Flowchart of the Methodology

3.2 Ni Metal Characterisation in SEM-EDX, XRD, and UV-VIS-NIR

Ni powder was purchased from ACS Materials and was used without any purifications. Ni particles were examined by SEM-EDX with a COXEM EM-30AX instrument to assess their surface morphology and elemental composition. To prepare for SEM-EDX analysis, a small amount of Ni powder was carefully affixed to a tape or substrate, ensuring a uniform distribution across the surface. Subsequently, the Ni powder sample underwent a gold coating process to enhance the conductivity and improve the imaging quality during the SEM-EDX analysis. The gold coating was applied using a sputter coater, which deposited a thin layer of gold on the surface of the sample. Figure 3.2 (a) depicts a distribution of Ni particles that can be identified

individually with very minimal agglomeration. In general, the shape of Ni particles is classified as spherical. Figure 3.2 (b) presents the size analysis of 50 Ni particles, and their diameters were measured using an imaging software (ImageJ 1.53k), which yielded an average size of approximately 0.9 µm. Figure 3.2 (c) shows the EDX spectra revealing the elemental composition of the sample, including Ni, gold (Au), and carbon (C) indicating that the sample comprised 88.69% by weight and 67.31% by atomic volume of Ni. The presence of C was likely originated from the sample substrate, while the presence of Au could be attributed to the 20-50 nm thick gold sputter coating applied during the sample preparation process.

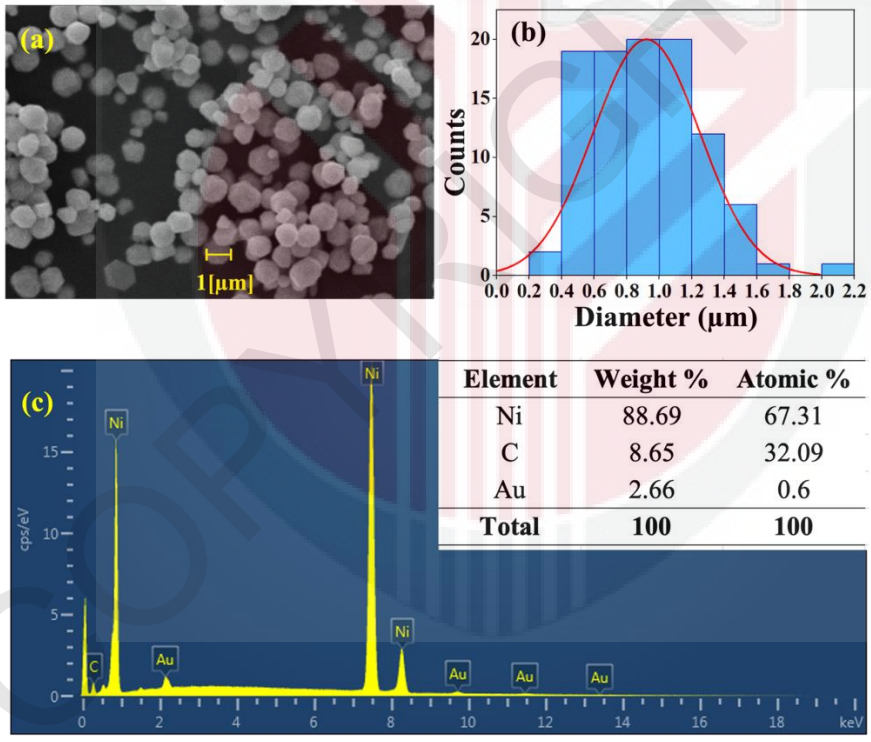

Element	Weight %	Atomic %
Ni	88.69	67.31
C	8.65	32.09
Au	2.66	0.6
Total	**100**	**100**

Figure 3.2 : (a) SEM-EDX Morphology Analysis (a) SEM Image of Ni Powder, (b) EDX Spectra of Elemental Composition (c) Elemental Mapping in Weight and Atomic Percentage, and (d) Measurements of the Diameter of Ni Particles in the Histogram Image

To verify the crystalline nature of the Ni powder, it was also characterised using an XRD, and then the phase structure and purity of the Ni powder were analysed. Figure 3.3 illustrates the positions and intensities of the peaks that can be used to determine the crystal structure of the Ni powder. The XRD pattern of the Ni powder shows a series of diffraction peaks that correspond to the different crystallographic planes of the Ni atoms in the sample. The strongest peak in the pattern occurs at a 2θ angle of approximately 44.5° and corresponds to the (111) plane of the face-centered cubic (FCC) crystal structure of Ni. Other prominent peaks in the pattern occur at 51.8° and 76.4°, which represent the (220) and (311) planes, respectively, as discussed in the literature [125] [126]. The XRD pattern of the Ni powder demonstrates that it is a single phase, with no other impurity diffraction peaks detected, except for the FCC peak.

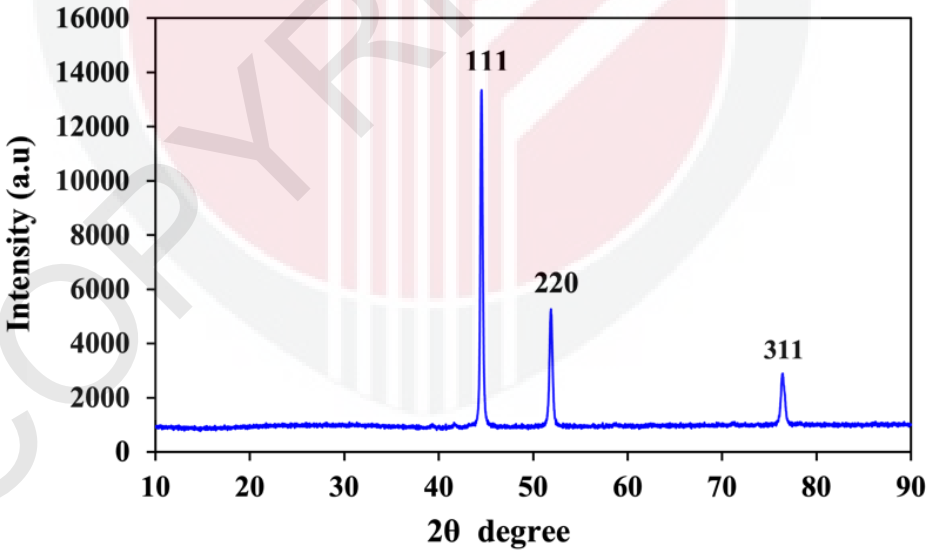

Figure 3.3 : XRD Peaks of Ni Powder

Another significant aspect of the material properties is the band gap energy of the Ni powder and the Ni/PDMS composite. The preparation process of Ni/PDMS composite can be found in Section 3.3.1 below. The band gap energy refers to the minimum

energy required for a photon to be absorbed by a material, exciting an electron from the valence band to the conduction band. This evaluation allows extrapolation of the optical band gap of the material using a Tauc plot. The absorption coefficient is related to the optical band gap, $\boldsymbol{E_g}$ and photon energy, $\mathbf{hv}$ according to the following equation [127]:

$$(\boldsymbol{\alpha hv})^{s} = \mathbf{A}(\mathbf{hv} - \boldsymbol{E_g}) \tag{3.1}$$

where $\boldsymbol{s = 2}$ is for direct transmission, $\boldsymbol{s = 0.5}$ is for indirect transmission and A is the constant of proportionality. The optical band gap (indirect) of pure PDMS has also been presented in the literature [129]. Figure 3.4 presents the band gap energies of both Ni powder and PDMS alone. The intercept indicated by the arrowhead has a distinct linear region that determines the onset of the absorption. From these figures, the band gap energies estimated for Ni powder and PDMS alone are 3.00 and 4.95 eV, respectively. The band gap of PDMS is similar to that reported in the previously presented study [129], indicating that neat PDMS has a well-defined and stable electronic structure without additional defect levels.

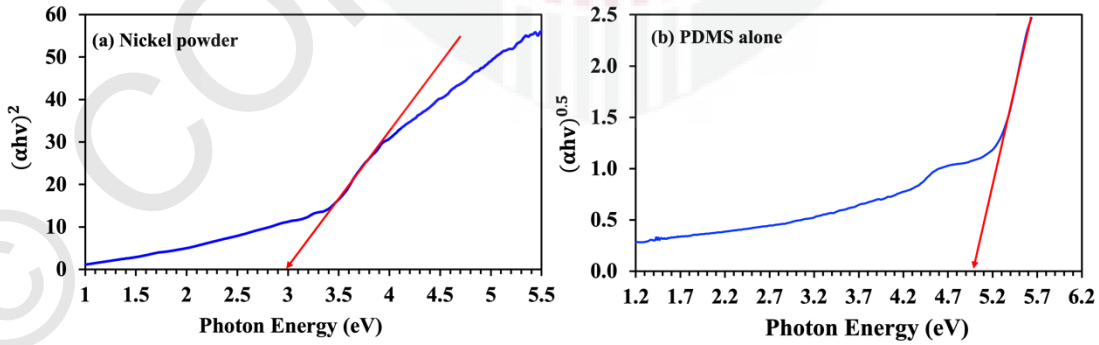

Figure 3.4 : Tauc Plot of (a) Ni Powder and (b) PDMS Alone for Band Gap Measurements

However, despite the band gap energy of the material, their absorption properties were also observed. This characterisation was performed in the wavelength range of 700-2000 nm using a PerkinElmer UV-WinLab, as depicted in Figure 3.5. Notably, the absorption intensity increased across the 700-2000 nm wavelength range for Ni/PDMS and Ni powder compared to that of the PDMS film alone. These results align with those reported by [108], visually confirming that Ni-loaded catalysts exhibit a black-colored appearance compared to the white or pale-yellow color of the neat supports. Additionally, both Ni powder and Ni/PDMS showed broader absorption characteristics within the erbium window, consistent with the literature findings from [128], which is usually attributed to the broader absorption characteristics of the metallic nickel.

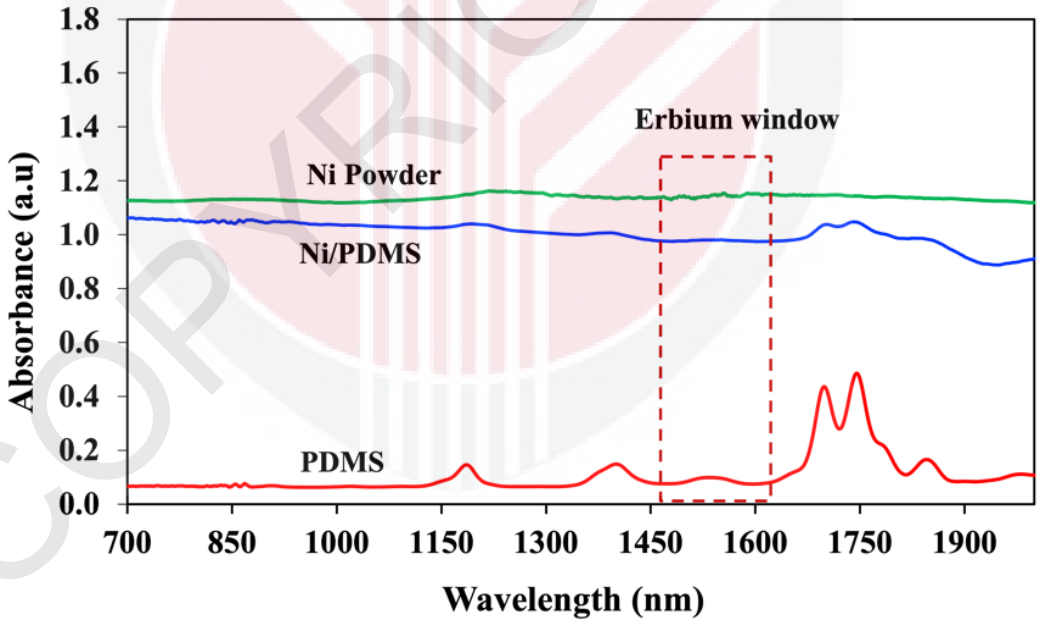

Figure 3.5 : Optical Absorbance of Ni Powder, Ni/PDMS, and PDMS

3.3 Ni/PDMS SA Fabrication Process

3.3.1 Preparation of Ni/PDMS Composite

In this study, all materials were utilised without further purification. As mentioned earlier, Ni powder was purchased from ACS Materials, and tetrahydrofuran (THF) was acquired from Sigma Aldrich. The silicone elastomer of PDMS (Sylgard®184) was obtained from Dow Corning. To fabricate a Ni/PDMS-SA, a liquid-phase exfoliation method was employed. Figure 3.6 shows the preparation of the Ni/PDMS composite, where THF served as a solvent to facilitate the exfoliation and uniform dispersion of Ni. Firstly, 6.0 mg of Ni powder was sonicated in 10 mL of THF using probe sonication (Hielscher UP200s) for 2 hour to ensure that the solution was well dispersed. Subsequently, 1 g of PDMS was mixed with a well-dispersed Ni solution, and the mixture was placed in a vortex mixer to prevent inhomogeneous dispersion of the material and polymer. To ensure a homogeneous solution of Ni particle dispersion in the polymer matrix, constant stirring was conducted using a hot plate at room temperature. Then, the stiring process was continued at temperature of 60°C for 24 hour to evaporate the solvent. After the completion of solvent evaporation, 0.1 g of a curing agent was mixed with the solution to cure the composite. It was then placed in a vacuum chamber for 1 hour to eliminate any trapped air bubbles.

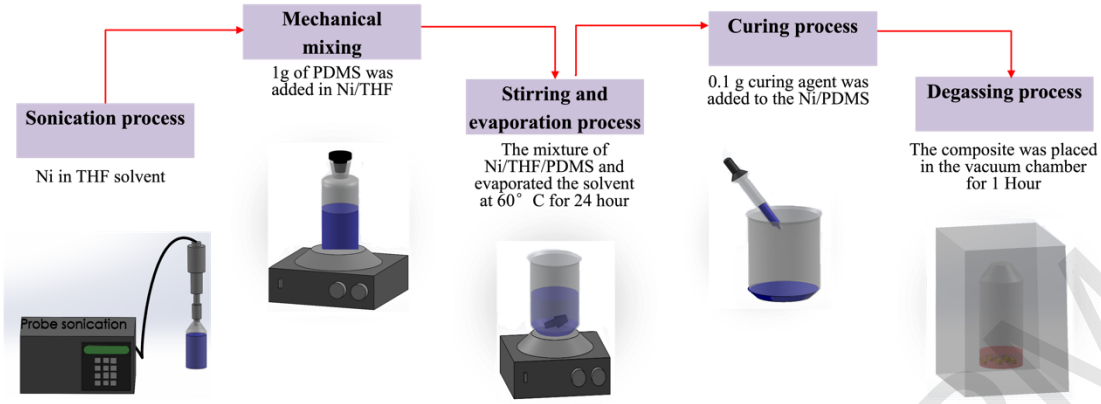

Figure 3.6 : Preparation Step for Ni/PDMS Composite

3.3.2 Preparation and Characterisation of a Tapered Fibre

A Vytran GPX-3400 optical processing workstation was employed to fabricate a tapered fibre. Figure 3.7 shows a Vytran optical processing workstation consists of a PC-based graphical interface and a coolant pump.

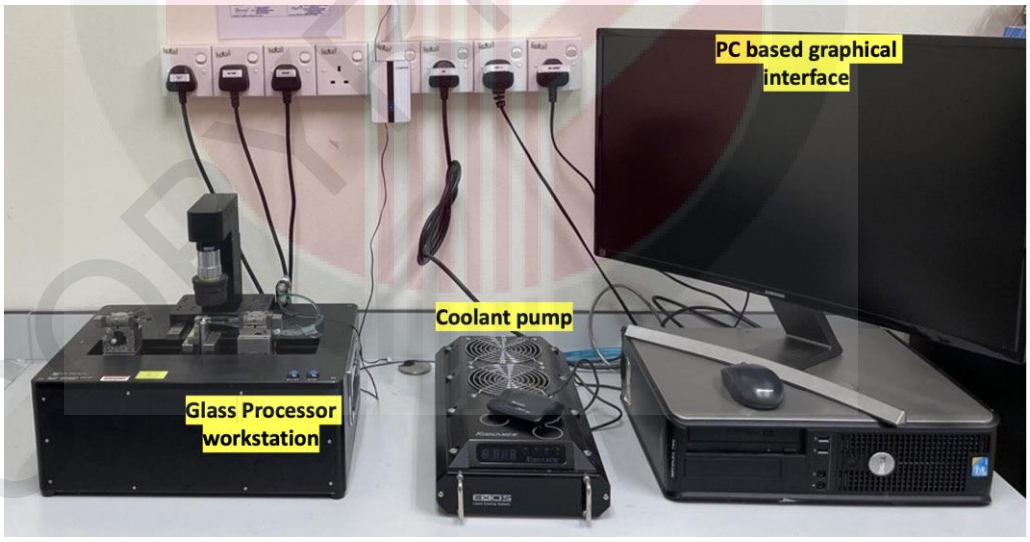

Figure 3.7 : Vytran GPX-3400 Optical Processing Workstation

In this work, a SMF was stretched during the fibre tapering process by heating and pulling at a speed of 1.0 mm/s [129]. The fabrication step started by stripping the outer polymer of a SMF, followed by a tapering procedure until the fibre diameter reached

10 μm in the waist region. Figure 3.8 demonstrates a schematic of the tapered fibre measurement for the down and upper taper lengths that were used in this study. The overall length of the tapered fibre was 60.8 mm, and the waist length was specified to be 0.8 mm. According to [130] an increase in the taper length or a reduction in the taper angle results in a more adiabatic mode evolution. This gradual adjustment of light to the tapering geometry ensures the efficient coupling of modes, enabling the energy to remain primarily in the fundamental mode throughout the transition. Consequently, this improves the transmission efficiency and minimises losses. The taper angle (θ) in the transition zones plays a crucial role in determining the optical transmission characteristics of tapered fibres. A taper angle below approximately 5 mrad is classified as adiabatic, whereas angles exceeding 5 mrad are considered nonadiabatic, as detailed in [130]. In this experiment, an adiabatic taper was chosen to benefit from its low propagation loss, strong evanescent field, and suitability for light-matter interactions. The dimensions of the tapered fibre were selected based on previous research [21], which focused on optimising the moderate insertion loss in the bare tapered fibres. The chosen profile featured a fixed waist length (0.8 mm and up/down taper length of 30 mm. Prior to the deposition process, the transmission loss of the bare tapered fibre was measured and found to be less than 1.0 dB.

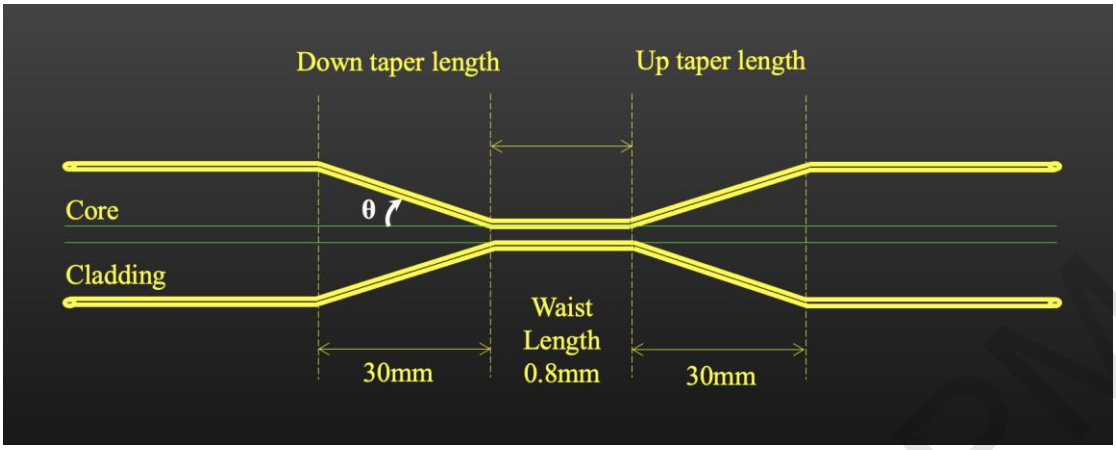

Figure 3.8 : Schematic Diagram of Tapered Fibre at the Upper Length, Lower Length, and Waist Length

Prior to the material deposition on the tapered fibre, it is essential to characterise the bare tapered fibre to ensure its minimum loss. In these steps, tapered fibre losses must be minimised to prevent significant extrinsic losses of tapered fibre caused by surface roughness or impurities [131], [132]. To begin the process, the fragile tapered fibre was placed on a flat substrate before the loss characterisation and material deposition onto the tapered fibre were conducted. The bare tapered fibre was characterised via a transmission measurement performed using an amplified spontaneous emission (ASE) as an optical source coupled to an optical spectrum analyser (OSA, Yokogawa AQ6370B), as shown in Figure 3.9 (a). The measurement was started by connecting the ASE source directly to an OSA with a resolution bandwidth of 0.02 nm to get a reference optical spectrum in the wavelength range of 1530-1590 nm. Subsequently, a bare tapered fibre was inserted between the ASE and OSA to sweep the second optical spectrum. Figure 3.8 (b) shows the transmission loss of the bare tapered before the material deposition. The transmission loss was calculated as the difference between the reference and bare tapered fibre spectra.

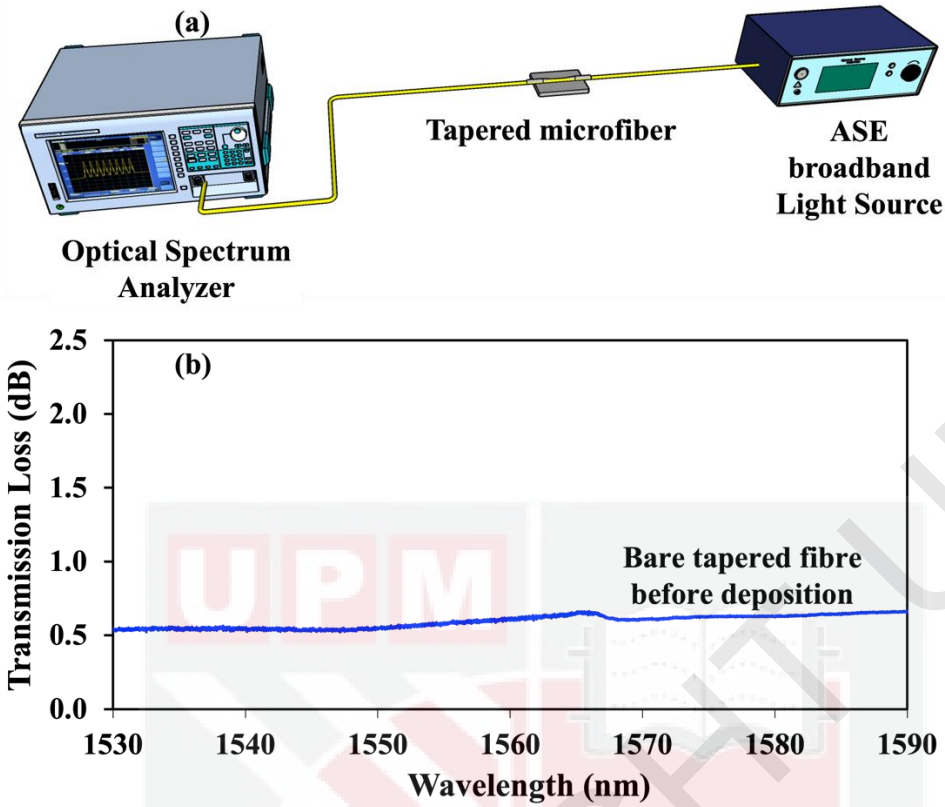

Figure 3.9 : (a) Measurement Setup of Tapered Fibre Loss and (b) Transmission Loss of Bare Tapered Fibre Characterisation

3.3.3 Deposition of Ni/PDMS SA and its Characterisation

After the characterisation of the bare tapered fibre, the Ni/PDMS composite was deposited. A small drop of the Ni/PDMS composite solution was poured into the waist region of the tapered fibre. A spin-coating technique was used to ensure that the prepared composite was evenly distributed on the tapered fibre [21]. In this study, a spin coater (TB616-SYSILE) was used at 4000 rpm for 5 minutes. These parameters were selected based on a previous study [21], explored spinning speeds ranging from 1000 to 5000 rpm and durations between 2 and 10 minutes. The spin-coating process was optimised to achieve the desired composite thickness on tapered fibres, and 4000 rpm for 5-6 minutes was identified as the optimal setting. This produced a tapered fibre SA with an effective thickness of less than 5 μm, which is suitable for ultrafast

pulse generation. Accordingly, the same spin-coating settings were adopted in this study to achieve similar nickel composite thicknesses. The reproducibility of the NiO/PDMS composite thickness further validated its effectiveness as an SA, enabling the generation of optical pulses instead of a CW laser output. Figure 3.10 shows the deposition process whereby the Ni/PDMS composite was dropped on the tapered fibre where it was positioned on the spin coater, and the process was followed by the spin-coating technique. The material attached to the tapered fibre was observed under a microscope. Figure 3.11 (a) illustrates the Ni/PDMS layer coated on the tapered fibre to form the SA. After the material deposition process, the Ni/PDMS SA was cured by drying under direct exposure to UV light for a few days. Once the SA was completely dried, it was necessary to characterise the transmission loss of the Ni/PDMS SA. Figure 3.11 (b) shows a comparison of the transmission loss for the bare tapered fibre and the Ni/PDMS SA. The transmission loss after the deposition process of the Ni/PDMS composite increased to 4.30 dB (average loss of 1530-1590 nm) owing to the material attachment on the tapered fibre and the light scattering effect compared to the 0.52 dB loss of the bare tapered fibre.

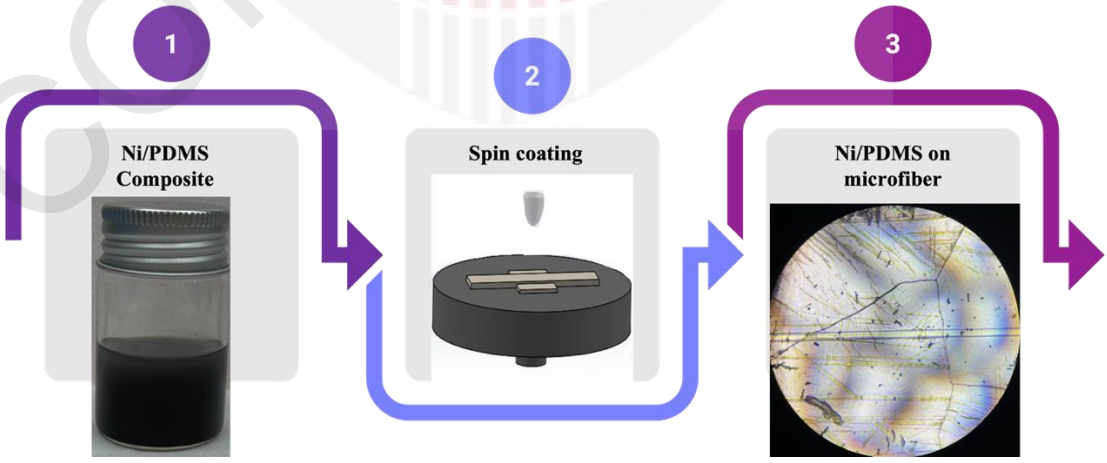

Figure 3.10 : Step Process of Deposition of Material to Tapered SA and Spin Coating Techniques

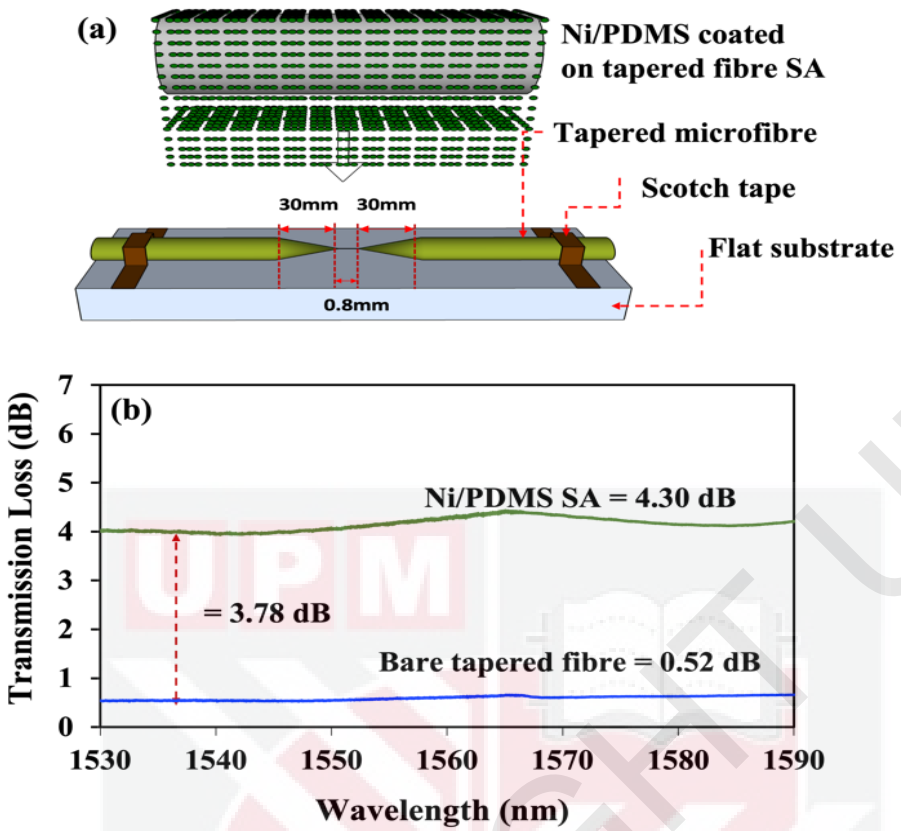

Figure 3.11 : (a) Illustration of Ni/PDMS Composite Deposition Process on the Tapered Fibre (b) Transmission Loss of Bare Tapered Fibre and Ni/PDMS SA

In the follow-up phase of Ni/PDMS-SA characterisation, SEM-EDX spectroscopy analysis was used to observe the surface topography of the Ni/PDMS-SA sample while identifying the elemental composition of the SA sample. Figure 3.12 (a) shows an image of the scattered particles of Ni materials attached along the waist region (10 µm in diameter) of the tapered fibre. Figure 2.12 (b) shows the distribution of the material composition in the Ni/PDMS-SA. According to the elemental analysis, 0.92% by weight and 0.31% by atomic volume of Ni were found in the SA sample. The EDX analysis also captured oxygen (O) and silicon (Si) from the glass substrate and silica fibre. Carbon (C) was also detected which is one of the fundamental elements of the PDMS. On the other hand, gold (Au) was found owing to the employment of a gold

sputter coating applied during the characterisation process. These findings confirmed the presence of Ni metal materials attached to the waist region of the tapered fibre.

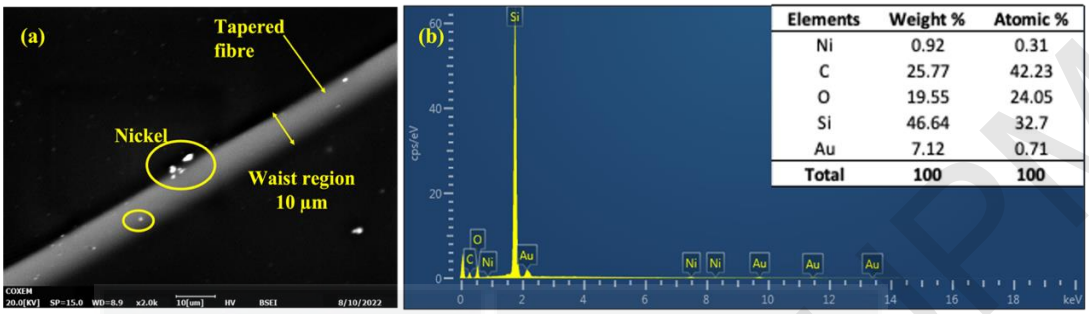

Figure 3.12 : (a) SEM Micrograph of Ni/PDMS SA along the Waist Region of the Tapered Fibre; (b) Material Composition Detected in Ni/PDMS SA

3.4 Nonlinear Saturable Absorption Measurement of Ni/PDMS-SA

NLO measurements are crucial for investigating the light-matter interactions of SA. The nonlinear transmission of Ni/PDMS-SA was measured using a balanced two-detector setup, as shown in Figure 3.13 (a). The pump light source used in the experiment was a femtosecond pulse laser source (PLS) with a central wavelength of 1560 nm, repetition rate of 60 MHz, and pulse duration of 150 fs. The output of the light source was connected to a variable optical attenuator (VOA) before splitting it using a 50:50 optical coupler (OC). One of the light paths was directed to an optical power metre (OPM-1) to serve as a reference signal. The other light path was spliced with the Ni/PDMS-SA under study, and its power was measured using another optical power metre (OPM-2). By varying the VOA settings, the transmitted power was recorded as a function of the incident optical power for Ni/PDMS-SA.

Figure 3.13 (b) depicts the nonlinear transmittance curve of the Ni/PDMS–SA fitted with Equation 2.1. Referring to the experimental findings, the ΔT, I_{sat}, and α_{ns} were

calculated to be 4.77%, 265 MW/cm^2, and 61.6% respectively. As stated in the literature, SA with at least 1.5% ΔT can produce a stable mode-locked pulse operating in the net negative dispersion region [134]. One of the many factors that influences the output pulse duration of the mode-locked cavity is the ΔT of the SA, where a higher ΔT value results in a shorter possible pulse [135].

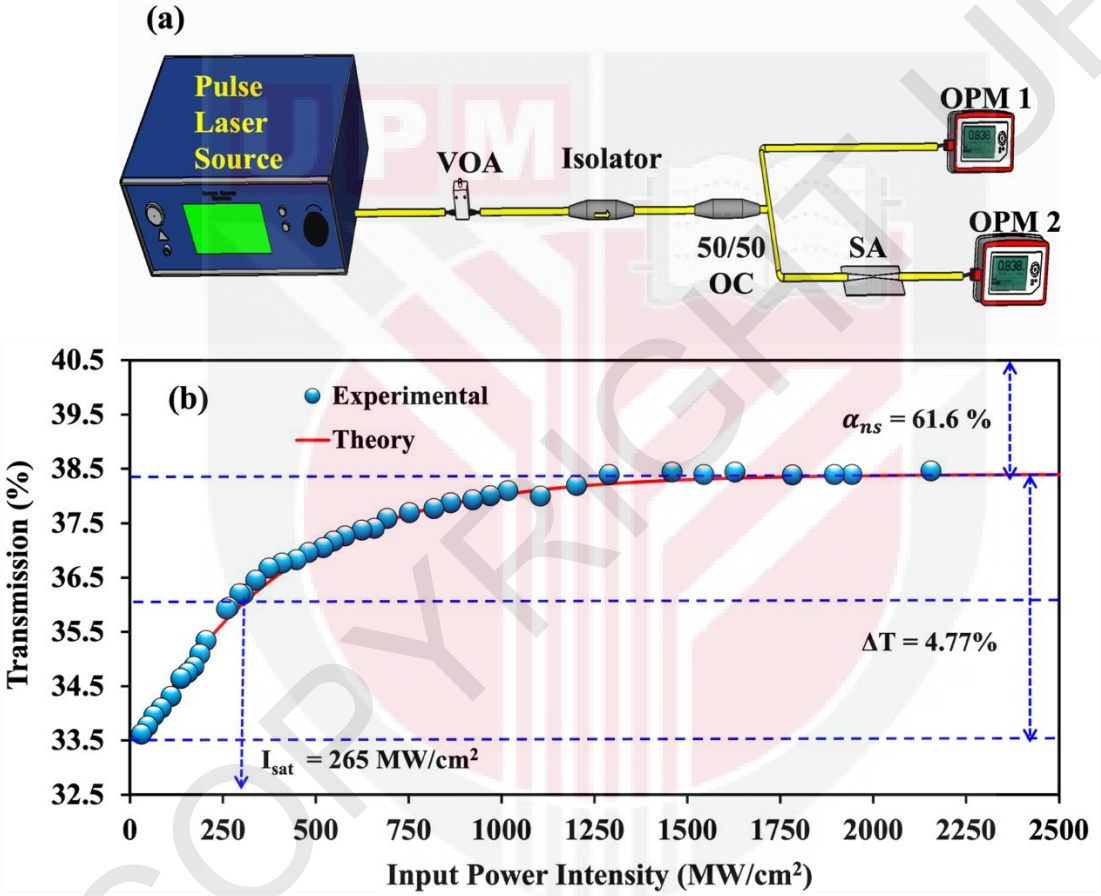

Figure 3.13 : Non-Linear Characterisation of SA; (a) Set-Up of the Balanced Two-Detector System and (b) Nonlinear Transmittance Curve of the Ni/PDMS-SA

3.5 Mode-Locked EDFL Cavity Setup

Figure 3.14 illustrates the configuration of the EDFL integrated with the Ni/PDMS-SA. The laser cavity configuration was composed of 0.65 m long erbium-doped fibre

(EDF, Liekki Er 110-4/125) with a peak absorption of 110 dB/m at 1550 nm and a GVD of 12 ps^2/km. The EDF was used as a gain medium, which was pumped by a 980 nm laser diode (LD) through a 980/1550 nm wavelength division multiplexing (WDM) coupler. A polarisation-independent isolator was connected to a 70:30 OC. The isolator was used for unidirectional propagation and to prevent unwanted back-reflection of light in the opposite direction. The 70:30 OC was placed between the isolator and a coil of the SMF, and 70% of the light was circulated back into the ring cavity. Thirty percent of the remaining light was extracted from the laser cavity and used to measure optical pulse performance. The Ni/PDMS-SA was then connected to the SMF coil and a polarisation controller (PC). In the setup, the PC was used to control the polarisation states of the circulating light [136]. The laser output was subsequently connected to a 90:10 OC to conduct simultaneous output measurements. Output 1 from the 90% leg of the OC was routed to an OPM (Thorlabs, PM100D, Thorlabs S148C), an oscilloscope (Tektronik TDS 3012C), a radio frequency (RF) spectrum analyser (GW Instek GSP-830), and an autocorrelator (APE PulseCheck). Output 2 from the 10% OC was connected to a Yokogawa AQ6370B OSA to analyse the optical spectrum across the desired wavelength range.

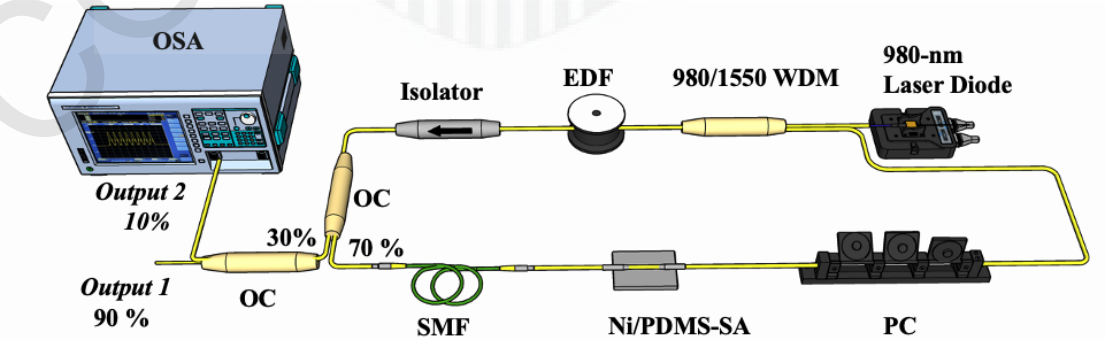

Figure 3.14 : Laser Configuration Setup of EDFL with Ni/PDMS-SA Tapered Fibre

3.6 Net Dispersion Calculations

In the context of this study, dispersion optimisation is the process of controlling the effect of pulse spreading within the laser cavity to attain stable and efficient mode-locking. The total cavity length, which was set at ~33.9 m including 32.2 m of SMF, 1 m of Hi-1060 fibre, and 0.65 m of EDF. The dispersion coefficients for SMF, Hi-1060 fibre, and EDF were -22, -7 and 12 ps^2/km respectively. A 19 m long segment of SMF, constituting part of the total cavity length and spliced between the Ni/PDMS-SA and the 70:30 OC, was trimmed at approximately 0.8 m intervals. The analysis involved the calculation of the net GVD at various SMF lengths, followed by an analysis of the mode-locked EDFL performance. This analysis covered various parameters; spectral bandwidth, pulse repetition rate, pulse duration, pulse stability, pulse energy development, and time bandwidth product (TBP).

To calculate the net GVD, each dispersion coefficient is multiplied by its length and then summed up to obtain the overall GVD value. The net GVD calculation considers the dispersion properties of all fibre components in the laser cavity, including the gain fibre, dispersion-compensating fibre, and any additional fibre components, such as SMF or polarisation-maintaining fibres. The formula for the net GVD calculation is as follows:

$$\boldsymbol{GVD_{net} = L_{SMF}\,\beta_{SMF} + L_{Hi-1060}\beta_{hi-1060} + L_{EDF}\beta_{EDF},} \qquad (3.2)$$

where, GVD_{net} is the total group velocity dispersion, L_{SMF} is the total length and β_{SMF} is the dispersion parameter for of the SMF-28 fibre, $L_{Hi-1060}$ is the total length and $\beta_{Hi-1060}$ is the dispersion parameter for Hi-1060 fibre, while L_{EDF} is the total length and β_{EDF} is the dispersion of EDF gain medium. Table 3.1 presents the estimated net

GVD for SMF lengths varying from 32.2 to 22.6 m. The results presented in the table demonstrate that increasing the SMF length leads to a higher anomalous dispersion. Increasing the length of the SMF to 32.2 m resulted in a higher net GVD with a negative value of -0.71 ps^2, compared to -0.49 ps^2 obtained with a 22.6 m SMF length inside the cavity. The increment in the anomalous dispersion value was attributed to the negative dispersion parameter of the SMF, which enhanced the overall negativity of the net GVD when added to the cavity [137].

Table 3.1 : Estimated GVD Values for the Laser Cavity Setup for Different Cavity Lengths according to the Experiment

Fibre Length (m)			Fibre GVD (ps^2)			
SMF-28	**EDF**	**Hi-1060**	**SMF-28**	**EDF**	**Hi-1060**	**NET GVD (ps^2)**
32.2			-0.71			-0.7083
31.4			-0.69			-0.6907
30.6			-0.67			-0.6731
29.8			-0.66			-0.6555
29.0			-0.64			-0.6379
28.2			-0.62			-0.6203
27.4	0.65	1	-0.60	0.0078	-0.007	-0.6027
26.6			-0.59			-0.5851
25.8			-0.57			-0.5675
25.0			-0.55			-0.5499
24.2			-0.53			-0.5323
23.4			-0.52			-0.5147
22.6			-0.50			-0.4971

3.7 Ni/PDMS SA at Alteration Net Dispersion for Pulse Laser Performance

3.7.1 Optical Spectrum for Mode-Locked Pulse Laser

To investigate the spectral characteristics of the laser output with respect to the length of the SMF within the laser cavity, optical spectrum analysis was performed for each tailored SMF length. The spectral bandwidth for the cavity length was measured at a pump power of 250 mW with a 0.02 nm resolution bandwidth of the OSA. The mode-

locking operation was achieved by adjusting the PC in the cavity. Figure 3.15 (a) illustrates the spectral bandwidth of SMF-22.6 m, and Figure 3.15 (b) depicts an enlarged view of the spectral bandwidth. The 3-dB bandwidth is calculated as the wavelength difference at the half of the peak power value of the optical spectrum, resulting in 3.98 nm. The spectral bandwidths for various SMFs were calculated and are presented in Appendix A. Figure 3.15 (c) summarizes the calculated spectral bandwidths for different SMF lengths, revealing a gradual decrease in spectral bandwidth as the cavity length increases. The widest spectral bandwidth of 3.98 nm, was achieved with the SMF length of 22.6 m, while the SMF length of 32.2 m resulted in a spectral bandwidth of 2.91 nm. This outcome may be attributed to the frequency offset, also known as spectral separation, between the soliton pulse and dispersive wave sidebands, which is inversely proportional to the cavity dispersion [138], [139]. This finding is further supported by the work of [140], where the 3-dB spectral bandwidth decreases gradually as anomalous dispersion increases.

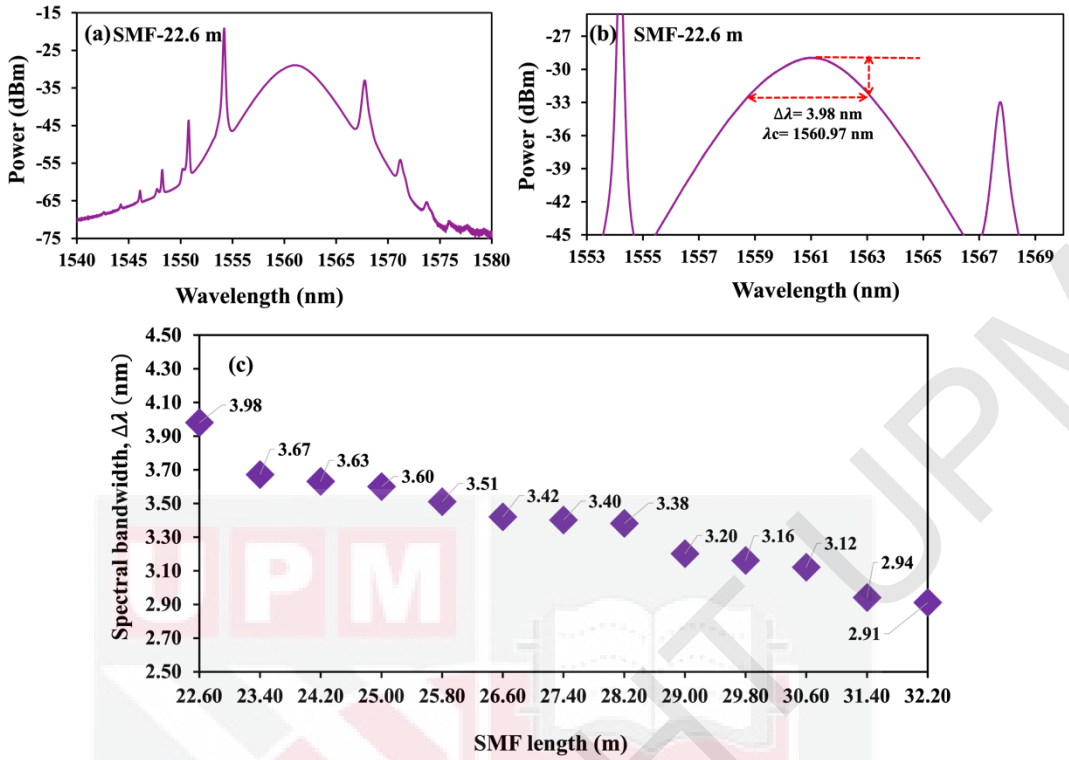

Figure 3.15 : (a) OSA Spectrum for the EDFL with 22.6 nm Length SMF and (b) its Enlarged Spectrum Indicating the Calculation of the Sepctral Bandwidth. (c) Laser Spectral Bandwidth against Variation of Total SMF Length in the EDFL Cavity

Following the observation of the optical spectrum, Figure 3.16 represents the Kelly sidebands comparison between SMF-22.6 m and SMF-25.8 m. The number of observable Kelly sidebands in the soliton increased when a longer SMF was used in SMF-25.8 m (k1, k2, k3, k4, and k5) compared to the SMF-22.6 m (k1, k2, k3, and k4). Theoretically, the Kelly sidebands order can be determined by the resonant conditions of phase matching between the dispersive wave and the soliton [141]:

$$N = \frac{1}{2\pi}(\phi_s - \phi_d) = \beta_s L - \beta_d L, \tag{3.3}$$

where N is the sideband order, ϕ_s is the phase shift of the soliton per round trip, ϕ_d is the phase shift of the dispersive wave per round trip, β_s is the mode-propagation constant of the soliton, and β_d is mode propagation constant of the dispersive wave.

When a longer cavity length is used, the cavity round-trip time is longer, leading to a narrower frequency spacing between the frequency of the comb lines. This narrower spacing results in a higher number of observable Kelly sidebands in the Stokes region, which can be observed experimentally [142].

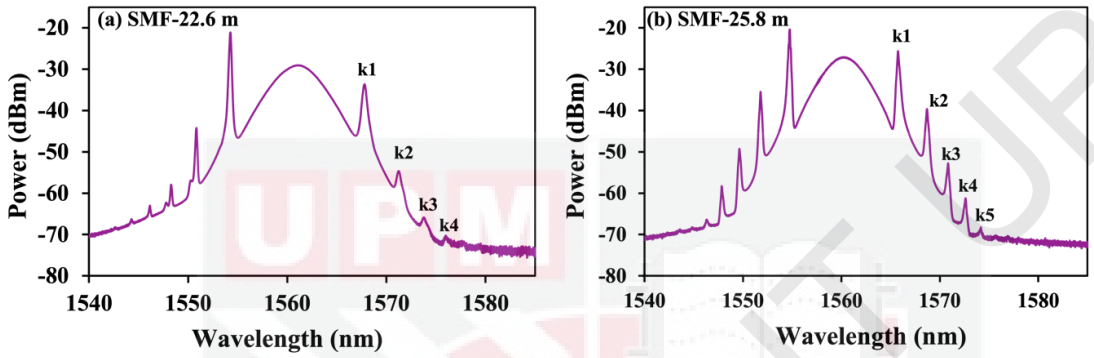

Figure 3.16 : Optical Spectrum of MLFL Employing Additional (a) SMF-22.6 m and (b) SMF-25.8 m

To further validate the SMF optimisation, its length was trimmed to 21.8 m, resulting in the appearance of a CW component. The existence of a CW component can induce modulation instability in the laser cavity. Even though the PC was oriented to detect the fundamental pulse, none of the pulses corresponding to the fundamental pulse appeared, unless there were multiple pulses with a CW component in the spectrum. During the experiment, by increasing the pump power to more than 60 mW and adjusting the orientation of the PC, multiple pulses were observed. Figure 3.17 (a) shows the threshold of the CW laser, the ML threshold, and the ML spectrum at the maximum pump power. Figure 3.16 (b) shows an enlarged image of the soliton spectrum with the appearance of the CW component. When the CW appears in the spectrum, it affects the temporal locking among multi-solitons, leading to the formation of a multi-soliton state [143]. Therefore, the oscilloscope trace served as an

evidence of multiple pulses, and it is presented in Appendix B along with the RF spectrum and AC trace.

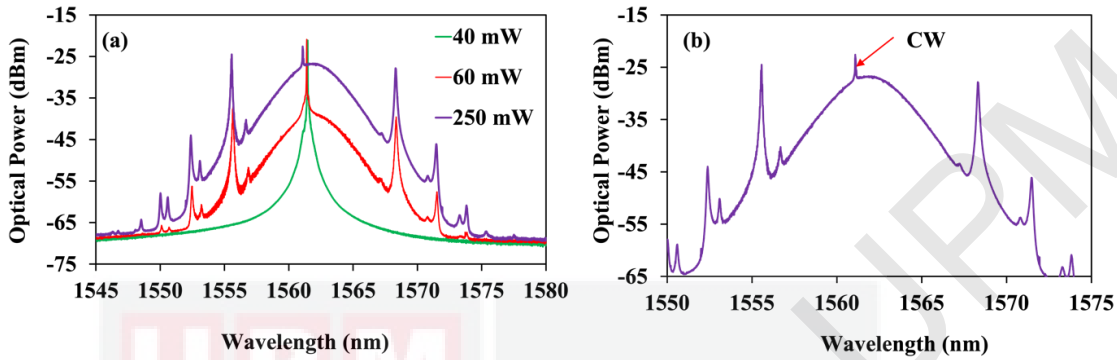

Figure 3.17 : Laser Output of EDFL with SMF-21.8 m; (a) OSA Spectrum at CW Laser Threshold, ML Threshold and ML at Maximum Pump Power, and (b) Enlarged View with CW Component at Maximum Pump Power of 250 mW

3.7.2 Oscilloscope Pulse Train

Further data collection was performed by observing the pulse from the oscilloscope trace across all the SMF lengths in the cavity. The pulse train was captured using an oscilloscope (Tektronik TDS 3012C) and a Thorlabs SIR5-FC 5 GHz photodector. To illustrate the captured oscilloscope trace,

Figure 3.18 (a) displays the pulse train generated during the mode-locking operation at a maximum pump power of 250 mW. Notably, two adjacent pulses were observed, separated by a duration of 117.23 ns, resulting in a repetition rate of 8.53 MHz at SMF-22.6 m. Other pulse train traces are appended in Appendix C.

Figure 3.18 (b) illustrates a gradual reduction of repetition rate, progressing from 8.53 MHz (SMF-22.6 m) to 6.03 MHz (SMF-32.2 m). This observation highlights the impact of the SMF length on the repetition rate of the laser pulses, indicating that

longer SMF lengths result in a lower repetition rate. This observation supports the hypothesis that an increase in the total path length results in a corresponding increase in the round-trip time, consequently leading to a lower pulse repetition rate. The repetition rate of the fundamental pulse of different SMF lengths should match the relation between the round-trip time (T_R), n is the refractive index of SMF and c is the speed of light as represented by:

$$T_R = \frac{nL}{c}, \tag{3.4}$$

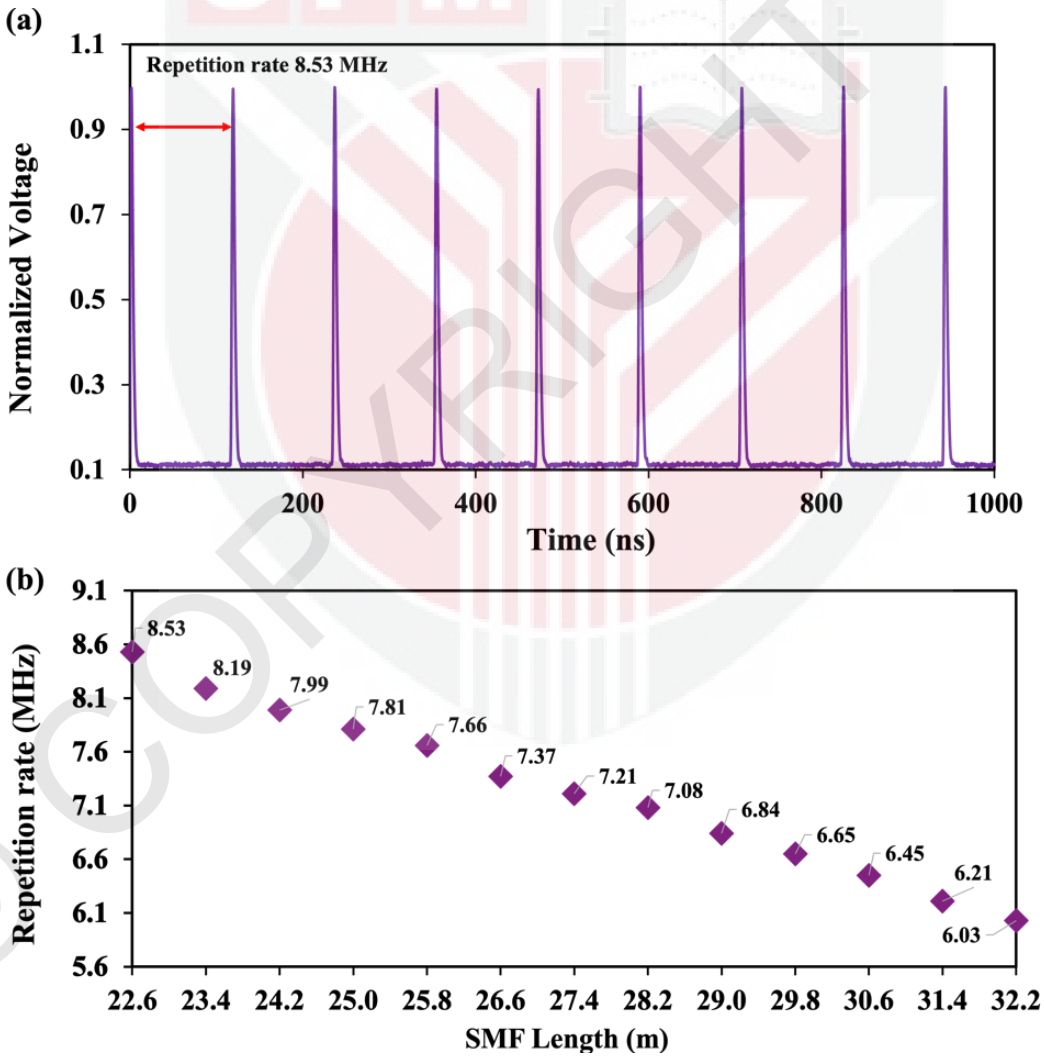

Figure 3.18 : (a) Osciloscope Trace for SMF-22.6 m and (b) Fundamental Repetition Rate Decrements Observed with SMF Alterations

3.7.3 Pulse Duration

Further analysis was conducted by measuring average pulse duration for all the SMF lengths. Pulse duration measurements were performed by using an autocorrelator (A.P.E. PulseCheck) with a constant pump power of 250 mW. To illustrate an example of a $sech^2$ profile-fitted measurement, Figure 3.19 (a) presents a $sech^2$ profile-fitted analysis with a decorrelation factor of 0.648 conducted to measure pulse durations within a span of 6 ps. The full width at half maximum (FWHM) of the pulse width, determined from the autocorrelation trace indicating a value of 1.15 ps, resulting in a pulse width of 745 fs for SMF-22.6 m. Other autocorrelator traces are appended in Appendix D. Figure 3.19 (b) demonstrates a continuous increase in pulse width duration (fs) with the additional length of the SMF within the cavity. The fastest pulse duration was attained with the shortest cavity length of SMF-22.6 m which stands at 746.00 fs compared with 886.87 fs of SMF-32.2 m. The net GVD coefficients for the shortest and longest SMF setups were distinctly recorded as -0.4971 and -0.7083 ps^2, respectively. This correlation emphasizes the direct proportionality between pulse duration and the GVD coefficient for a constant pulse energy and nonlinear index. This observation can be described by the relationship between pulse duration and GVD as $E\tau \propto \beta_2\eta_2$ where η_2 is the non-linear index as discussed in [144]. In simpler terms, larger absolute values of β_2 (indicating stronger anomalous dispersion) resulted in longer pulse durations.

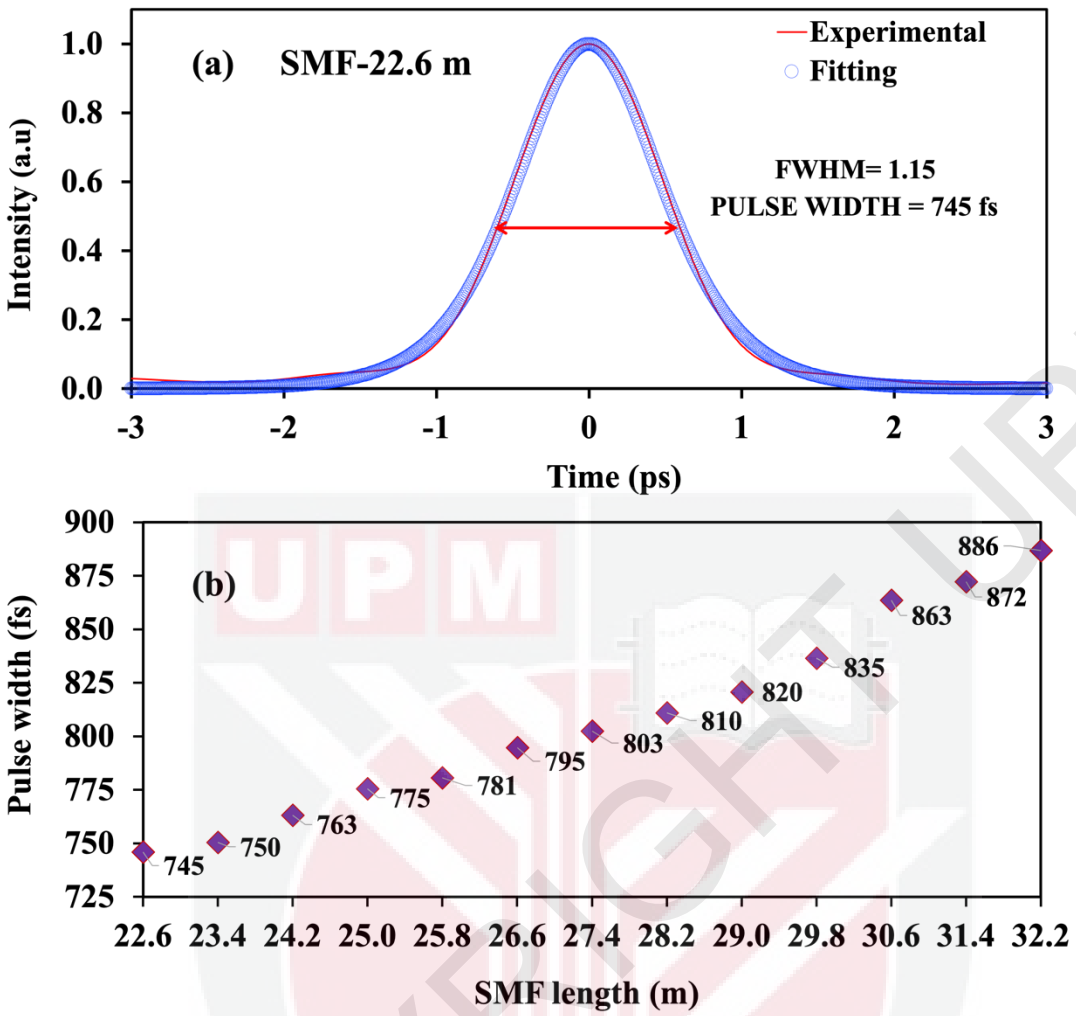

Figure 3.19 : (a) Autocorrelation Trace of the Generated Pulses at SMF-22.6 m (b) Pulse Duration Results Obtained by Employing Different Additional SMF Lengths

3.7.4 Peak-to-Pedestal Extinction Ratio

Pulse stability was measured using RF signals and was captured using an electrical spectrum analyser (GW Instek GSP-830) with a resolution bandwidth (RBW) of 300 KHz and a video bandwidth (VBW) of 300 Hz with a 100 MHz span. The RF measurements indicated that the laser operated in its fundamental regime at different frequencies across various SMF lengths. The following section discusses the peak-to-pedestal extinction ratio (PER) which is one of the features for the mode-locked pulse stability. Figure 3.20 (a) illustrates the PER calculation, determined by comparing the

pulse's peak power to the level of background noise, resulting in 56.9 dB for SMF-22.6 m. Additional PER calculations based on RF spectrum analysis can be found in Appendix E. Figure 3.20 (b) illustrates the PER values exhibit an uneven scheme pattern from SMF-22.6 m to SMF-32.2 m, with the highest PER of 57.55 dB observed at SMF-24.2 m and the lowest at 55.23 dB for SMF-32.2 m. In this work, all PER measurements represent a substantial improvement compared with the previous work reported by [145], which had an unsteady beat with a PER value of 54.1 dB. The experimental observation revealed no significant fluctuations in the PER value, indicating a good pulse-train stability of the generated mode-locked pulses.

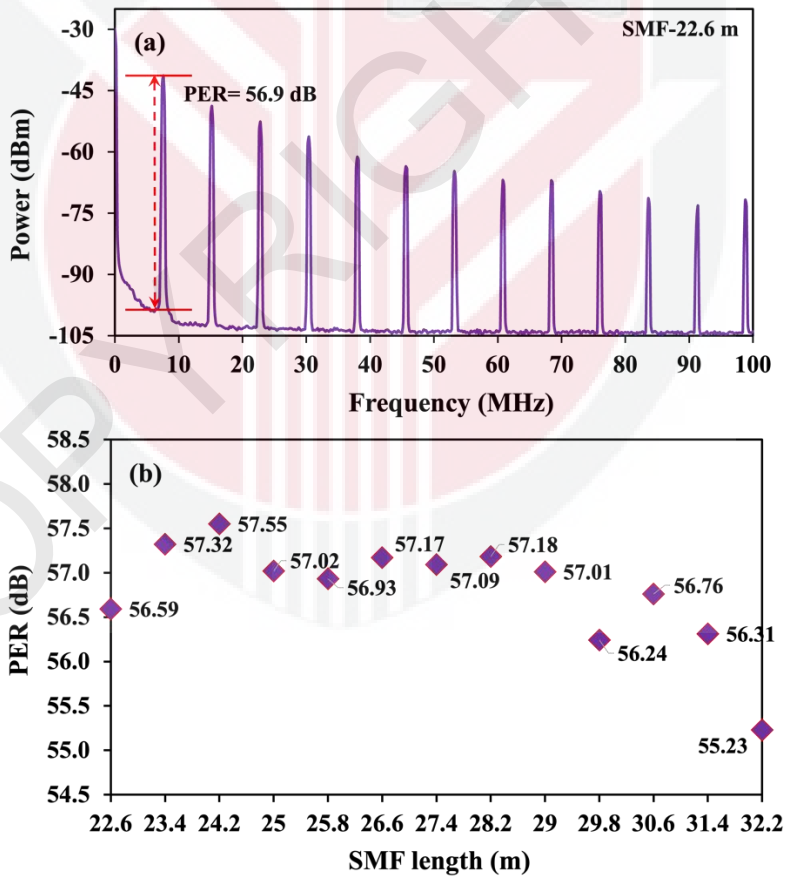

Figure 3.20 : (a) RF Spectrum of the Laser Output Measured with SMF-22.6 m and (b) Measurements of PER across the Additional SMF Length in the EDFL Cavity

3.7.5 Average Output Power and Pulse Energy

Figure 3.21 (a) depicts a discernible pattern which reveals a linear increase in average output power in tandem with the rise in pump power. Figure 3.21 b) shows the characteristic of pulse energy with respect to pump power at every SMF length. To closely examine the trend in average output power concerning SMF length, Figure 3.21 (c) highlights a subtle decrease in average output power when comparing SMF-22.6 m (5.98 mW) to SMF-32.2 m (4.94 mW), while maintaining a constant pump power at 250 mW. These results confirm a slightly higher cavity loss associated with longer SMF lengths compared to the shorter ones. To quantify the attenuation introduced by incorporating SMF into the laser cavity, the formula $\alpha = \alpha_o L_f$ was employed, where α_o is 0.21 dB/km for SMF at 1550 nm wavelength, and L_f represents the part of fibre length. The calculated attenuation values for SMF-22.6 m and SMF-32.2 m were 0.0047 dB and 0.0068 dB, respectively. This resulted in a noticeable decrease in output power for the longest SMF utilised in this cavity.

The secondary axis in Figure 3.21 (c) shows a subtle increase in pulse energy at maximum pump power. The longest SMF-32.2 m exhibited the highest calculated pulse energy at 0.91 nJ, while the shortest SMF-22.6 m recorded the lowest at 0.79 nJ. This observation underscores a linear correlation between cavity length and pulse energy, as expressed by the following equation:

$$\boldsymbol{E = P_{out} T_R = P_{out} \frac{nL}{c}}, \tag{3.5}$$

where E is the pulse energy, P_{out} is the average power output. Clearly, for a given section of optical fibre and average power, as the cavity length increases, a higher

pulse energy can be achieved [146]. Figure 3.21 (d) depicts the CW laser threshold at various SMF lengths, revealing a subtle increase in the CW laser threshold at shorter SMF lengths compared to longer ones. Similarly, the ML threshold follows the same trend, with the lowest threshold observed at shorter SMF lengths and the highest at longer SMF lengths. The ML threshold in a fibre laser refers to a minimum pump power required to initiate a stable mode-locking, which occurs when the laser output consists of a stable train of ultrashort pulses. The increase in the ML threshold can be attributed to the higher cavity loss, which requires higher pump energy to initiate mode-locking performance, as discussed in [147]. Table 3.2 summarizes the mode-locked laser performance parameters of average output power, mode-locked threshold, pulse energy, and slope efficiency.

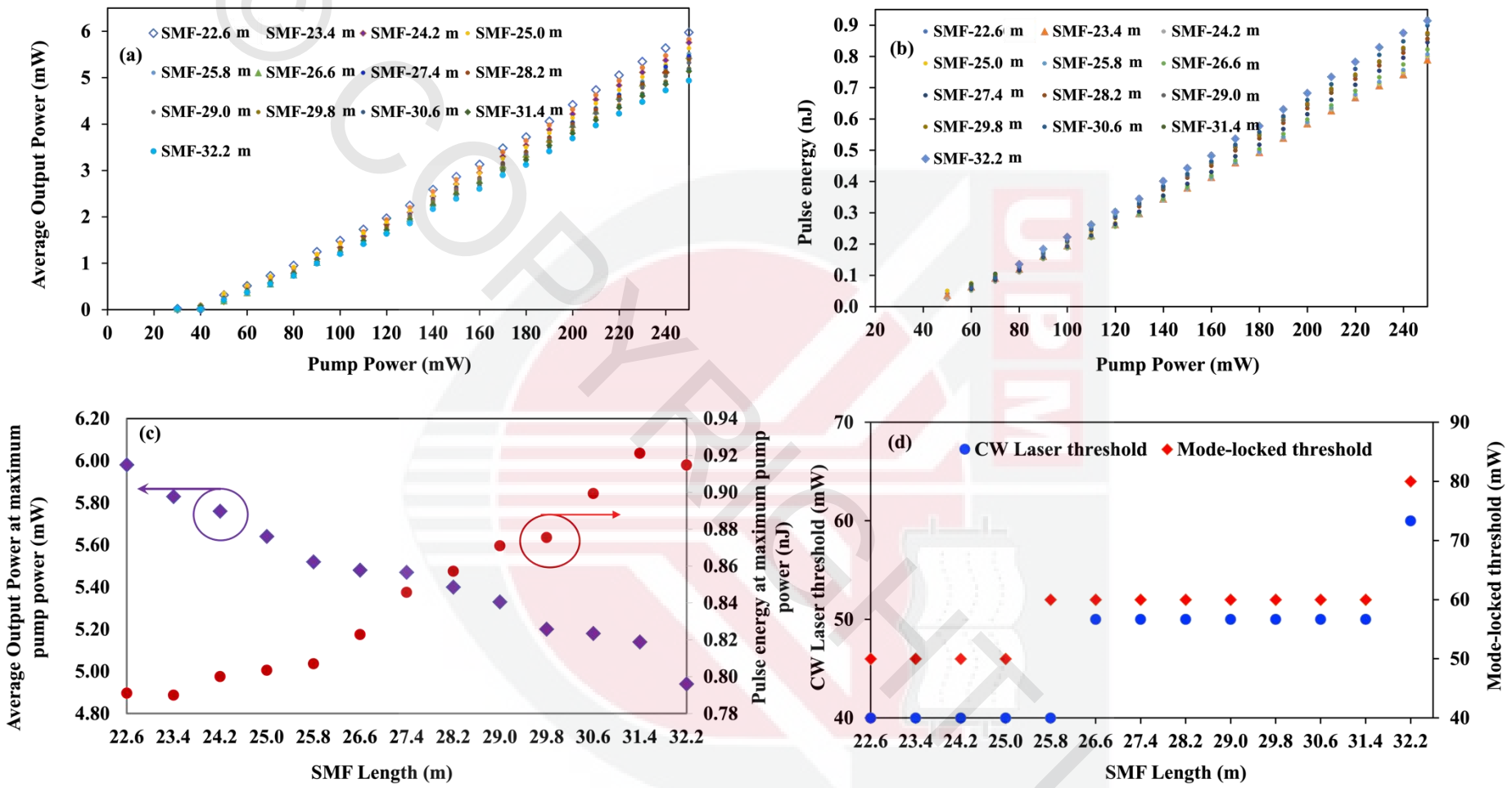

Figure 3.21 : (a) An Average Output Power Over Pump Power (b) Pulse Energy over Pump Power for Overall SMF Length (c) Average Output Power and Pulse Energy at Maximum Pump Power Plotted over SMF length (d) CW Laser and ML Treshold Power over SMF Length

Table 3.2 : Summarizes the Laser Performance for Different SMF Lengths

SMF length (m)	Mode-locked threshold (mW)	Maximum Output power (mW)	Maximum Pulse energy (nJ)	Output Power Slope Efficiency %	Pulse Energy Slope Efficiency (nJ/W)
22.6	50	5.98	0.79	2.70	3.57
23.4	50	5.83	0.79	2.65	3.59
24.2	50	5.76	0.80	2.66	3.70
25.0	50	5.64	0.80	2.52	3.59
25.8	60	5.52	0.81	2.55	3.72
26.6	60	5.48	0.82	2.56	3.84
27.4	60	5.47	0.85	2.53	3.95
28.2	60	5.40	0.86	2.50	3.96
29.0	60	5.33	0.87	2.46	4.01
29.8	60	5.20	0.88	2.39	4.02
30.6	60	5.18	0.90	2.41	4.19
31.4	60	5.14	0.92	2.37	4.24
32.2	80	4.94	0.91	2.34	4.33

3.7.6 Optical Spectrum Stability, Autocorrelator Stability and Time Bandwidth Product

In the final part of the result analysis, a long-term stability experiment was conducted by continuously recording the OSA spectrum and AC trace within a 3.5 hour and 1 hour durations, respectively. The Ni/PDMS-SA operated continuously in the CS region under laboratory conditions. The experimental setup was kept constant at a fixed polarisation state and maximum pump power of 250 mW. The optical spectrum was swept at a bandwidth resolution of 0.02 nm every 2 minutes within 3.5 hours. Figure 3.22 (a) shows a 3-D spectrogram of the OSA spectrum with respect to time. Figure 3.22 (b) represents the calculations of the 3 dB spectral bandwidth and central wavelength extracted from the CS stability within 200 minutes for SMF-22.6 m. Based on the findings, the average spectral bandwidth (3.98 ± 0.04 nm) and the average central wavelength (1560.95 ± 0.09 nm) were attained. Both parameters indicate a small standard deviation, confirming the operational stability of the developed laser. The stability of the remaining optical spectrum for various SMF lengths is presented in Appendix F.

Next, while the OSA spectrum was recorded, the AC stability was simultaneously captured during the first hour. The AC stability data were recorded and saved at 2-minute intervals for a total duration of 60 minutes. Figure 3.23 (a) depicts the 3-D spectogram of the AC stability recorded in this experiment. Referring to Figure 3.23 (b), the average pulse width value is 746.0 ± 5.4 fs. Based on the findings, no significant changes of the value of pulse width, indicating the generated pulse was stable during the experiment. While the stability of the remaining AC traces for various SMF lengths is presented in Appendix G.

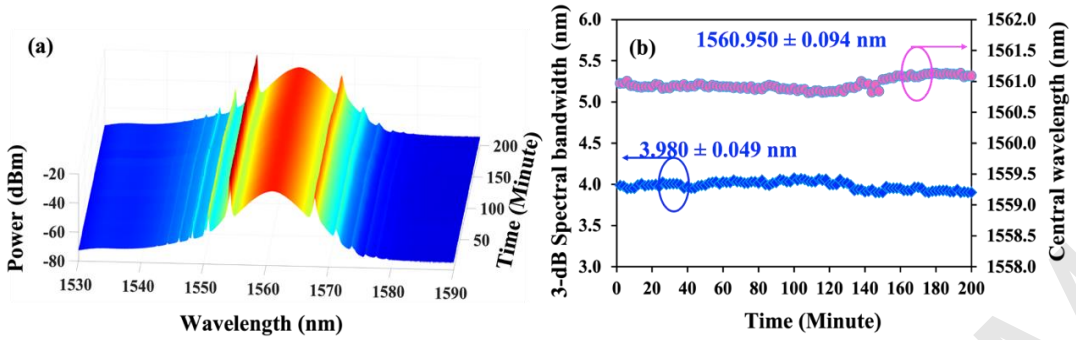

Figure 3.22 : OSA Stability Captured within 200 Minutes for SMF-22.6 m (a) 3-D Spectogram of Spectrum Stability, and (b) Spectral Bandwidth and Central Wavelength Extracted from the Spectogram

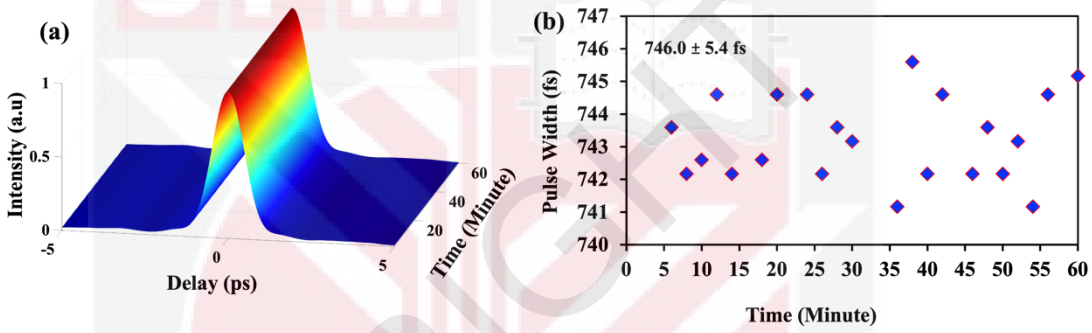

Figure 3.23 : AC Stability within 60 Minutes at SMF-22.6 m (a) 3-D Spectogram of AC Stability, and (b) Pulse Width of the AC Stability within 60 Minutes

TBP is calculated as the product of the pulse duration (Δτ) and the frequency bandwidth (Δν). The relationship between the TBP and pulse duration can be described as follows [148]:

$$\boldsymbol{TBP = \Delta f * \Delta \tau}\,, \tag{3.6}$$

$$\boldsymbol{\Delta f = \frac{C * \Delta \lambda}{\lambda^2}}\,, \tag{3.7}$$

where Δf is the frequency variance, Δτ is the time variance (FWHM of pulse intensity), Δλ is the 3-dB spectral width, and λ is the central wavelength. The estimated TBP values deduced from the experimental works are presented in Table 3.3. The minimum

value of TBP is 0.315 for the $sech^2$ hyperbolic pulse. A decrease in the TBP value was observed for a longer SMF length, which exhibited a longer pulse width and smaller spectral bandwidth. Chirped pulses do not maintain their TBP values and can exhibit changes in the pulse shape owing to the effect of chirp [149]. Hence, a minor chirp was observed, resulting in a shorter pulse width and broader spectral bandwidth when a shorter SMF was employed in this cavity. The TBP fluctuation is caused by variations in a few factors, including the filter bandwidth and optical and cavity dispersions [150].

Table 3.3 : TBP Estimation for ML-EDFL by Altering the Fibre Lengths

Additional SMF length	Average Centre Wavelength, λc (nm)	Standard Deviation, λc	Average 3dB Spectral bandwidth (nm)	Standard Deviation	Average Pulse width	Standard Deviation	TBP
22.6	1560.95	0.09	3.980	0.049	746.00	5.40	0.366
23.4	1559.20	0.07	3.660	0.051	750.50	6.80	0.342
24.2	1558.68	0.08	3.630	0.034	763.09	5.10	0.342
25.0	1559.28	0.06	3.610	0.033	775.55	3.00	0.345
25.8	1560.23	0.02	3.510	0.025	780.65	9.70	0.338
26.6	1560.18	0.02	3.420	0.033	794.77	1.60	0.335
27.4	1559.84	0.03	3.400	0.033	802.50	9.10	0.336
28.2	1559.35	0.04	3.380	0.022	810.91	3.20	0.338
29.0	1559.36	0.01	3.200	0.019	820.76	4.50	0.321
29.8	1559.66	0.02	3.170	0.057	836.20	2.30	0.323
30.6	1559.27	0.05	3.130	0.048	863.61	2.20	0.333
31.4	1559.40	0.01	2.950	0.039	872.24	7.60	0.317
32.2	1559.81	0.02	2.910	0.047	886.87	5.80	0.318

3.8 Summary

The optimisation of the ML-EDFL by adjusting the SMF length in the cavity is summarized in Table 3.3. A notable trend emerged as the SMF length increased in the cavity, resulting in a higher anomalous dispersion. This effect can be attributed to the dispersion properties of the cavity, where a longer SMF introduced additional

dispersion, leading to GVD values spanning from -0.4971 to -0.7083 ps^2. Longer SMF lengths caused the spectral bandwidth trend shrinks from 3.98 to 2.91 nm where narrower spectral bandwidth demonstrates larger pulse duration spanning from 746.00 to 886.87 fs, which is consistent with the Fourier transform theory. The longer SMF length not only amplifies attenuation loss but also precipitates an increase in the cavity loss, which can be observed from the changes in the average output power from 5.98 to 4.94 mW. An observable trend of central wavelength indicates a tendency toward shorter wavelengths with escalating additional losses within the intracavity. This phenomenon could probably correlates with population inversion theory, as it highlights the direct influence of the population inversion value at the threshold of the emitted wavelength [151]. Similarly an increase in the ML threshold corresponds to an elevation in cavity loss with longer SMF lengths integrated into the cavity.

Consequently, the decrease in pulse energy was observed, with changed from 0.91 to 0.71 nJ as attenuation loss increased. This observation suggests that there is an optimal SMF length within the cavity where the balance between dispersion effects and losses is favourable for achieving the best pulse characteristics. On the other hand, TBP values approached 0.315 as the SMF length increased to SMF-32.2 m, leading to longer pulse durations and a decrease in pulse repetition rates.

In terms of pulse stability, as evaluated from the PER measurements, an uneven pattern of PER values was observed against the length of the SMF, with the optimum PER value was achieved by using SMF-24.2 m length. Despite achieving the shortest pulse width of 746 fs with SMF-22.6 m, the PER value was only 56.59 dB, as compared to SMF-24.2 m. As a result, an additional SMF-24.2 m length was found to

be the optimum result, providing the highest pulse stability with a PER value of 57.55 dB, and a reasonably good pulse performance of 763 fs, where the pulse width is not excessively slow. Therefore, the additional SMF-24.2 m length was chosen as the optimum cavity length for subsequent experiments.

CHAPTER 4

NiO/PDMS SATURABLE ABSORBER FOR INVESTIGATING CONCENTRATION EFFECTS ON EDFL PERFORMANCE

4.1 Overview

This chapter focuses on analysing the effects of NiO concentration on the performance of ultrashort pulse generations. The experimental procedure involved in varying the concentration of NiO in a polymer composite. Figure 4.1 shows the flowchart of the methodology in this chapter. Initially, the preparation and material characterisation of the NiO/PDMS at different concentration ratios were performed, followed by the characterisation of the transmission loss. Subsequently, the nonlinear characteristics were discussed and comparative analysis was performed. Then SAs with different concentrations were integrated in an EDFL, and their pulse performances were assessed. The motivation is to explore the effect of NiO concentration on the nonlinear characteristics of the SA and the pulse performance of the EDFL in terms of the emission spectrum, pulse repetition rate, PER level, pulse duration, and overall pulse stability.

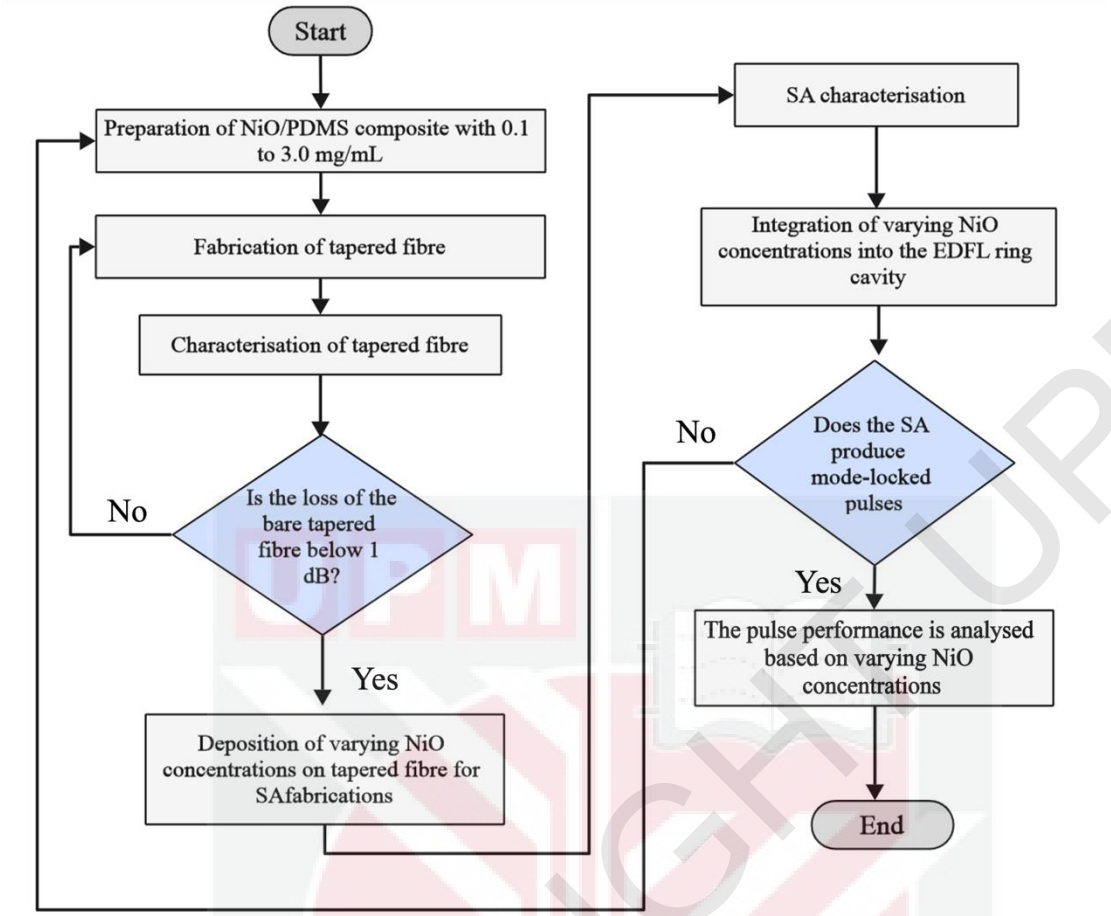

Figure 4.1 : Flowchart of the Methodology in Chapter 4

4.2 NiO Characterisation in SEM-EDX, XRD and UV-VIS-NIR

The morphological structures of the NiO particles were examined using SEM-EDX with a COXEM EM-30AX instrument. Figure 4.2 (a) presents a micrograph showing a high degree of particle aggregations, with smaller particles often aggregating or overlapping to form larger structures. Figure 4.2 (b) shows an analysis of 50 NiO particles, with diameters measured using an imaging software (ImageJ 1.53k). The average particle size was estimated to be approximately 3 µm. Figure 4.2 (c) presents the elemental composition analysis of the NiO powder and indicates the sample contained 60.31% by weight and 28.19% by atomic volume of Ni element along with 20.21% by weight and 34.75% atomic of oxygen in the sample. Additionally, the EDX

analysis detected carbon (C) likely originated from the sample substrate. The presence of gold (Au) can be attributed to the 20-50 nm thick gold sputter coating applied during the characterisation process.

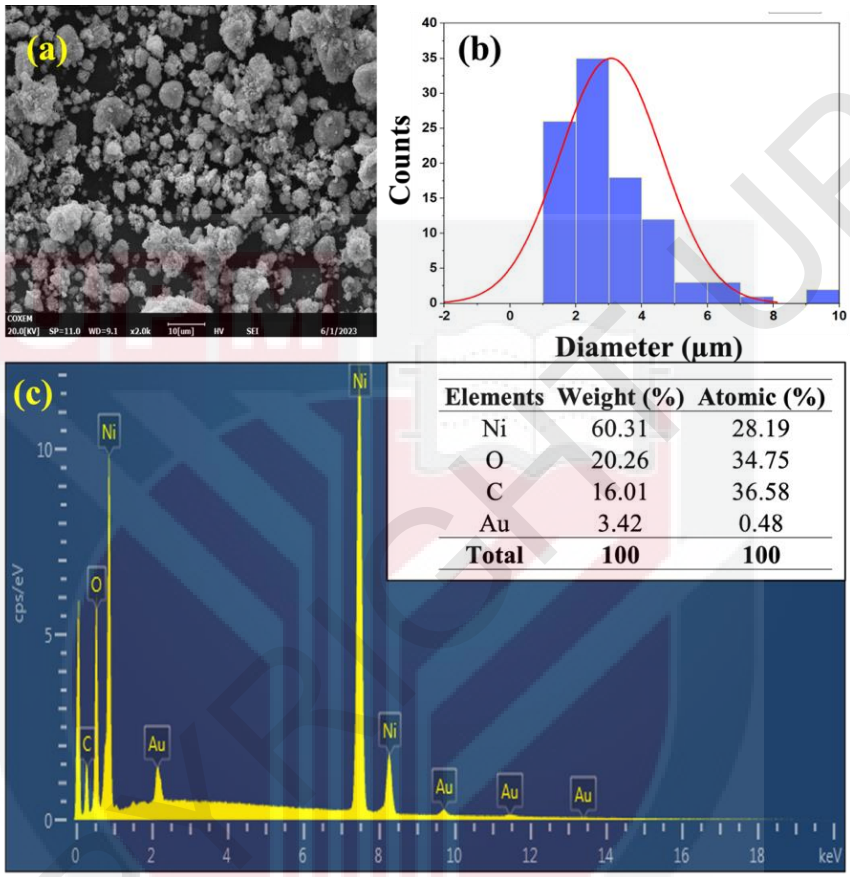

Figure 4.2 : Morphology Analysis (a) SEM Image of NiO Powder, (b) Elemental Analysis of NiO Powder, (c) Elemental Distribution in Percentage and (d) Counts of NiO Particles with Average Diameters

Following conformational analysis, it was necessary to characterise the NiO powder using XRD to verify its crystalline nature. The phase structure and purity of the NiO powders were analyzed from the XRD results. As shown in Figure 4.3, diffraction peaks at 37.2°, 43.2°, 62.7°, 75.4°, and 79.4° are determined for the NiO powder, which can be indexed to the (111), (200), (220), (311), and (222) planes of the cubic NiO structure, as reported in [152]. NiO was found to have a high degree of phase

purity, as there were no extra peaks in the spectrum. The XRD pattern of the NiO powder demonstrates that it is a single phase, with no other impurity diffraction peak detected, except for the peak indexed to the face-centered cubic structure.

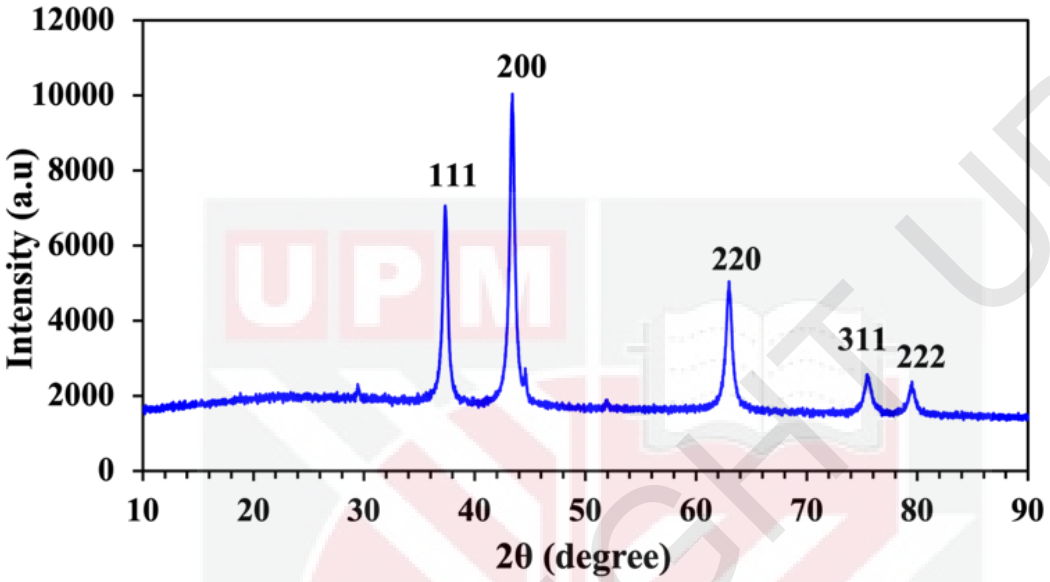

Figure 4.3 : XRD Peak NiO Powder Crystanality

Another significant aspect of the material properties is the band gap energy of the NiO powder. The absorption coefficient is related to the optical band gap, E_g and photon energy, hv according to Equation 3.1 as discussed in Chapter 3. Figure 4.4 a) shows the Tauc plot of the NiO powders, and the band gap energy value of 2.92 eV, which aligns with previously reported work [153]. To verify the feasibility of the NiO composite to be operated in the erbium wavelength range, an absorption in the wavelength range of 800 - 2000 nm was performed using a PerkinElmer UV-WinLab, as shown in Figure 4.4 (b). From the results, a comparison between the NiO powder, NiO/PDMS composite, and PDMS alone was performed. The preparation method of NiO/PDMS composite can be found in Section 4.3 below. It is apparent from the Figure 4.4 (b), the presence of NiO increased the absorption intensity across the NIR

light spectrum compared with PDMS alone or NiO/PDMS. It was found that when Ni ions doped into glasses, they act as absorption centers, leading to the appearance of absorption peaks in the optical spectra of the glasses [154]. The optical absorption of Ni ions in glasses is due to the optical transitions between the d orbitals of the Ni ions, as explained in [154].

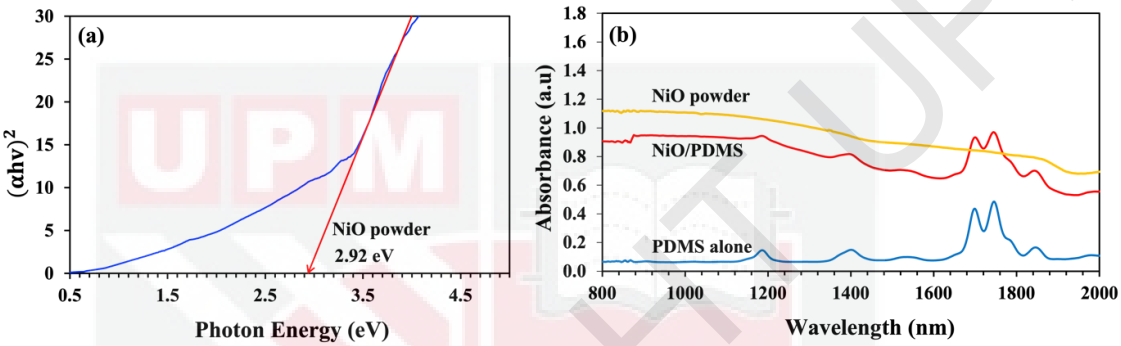

Figure 4.4 : (a) Tauc Plot of NiO Powder, and (b) Absorbance (a.u) of NiO Powder, NiO/PDMS and PDMS Alone Versus Wavelength

4.3 NiO/PDMS SA Fabrication at Various NiO Concentrations

NiO powder and THF were purchased from Sigma Aldrich, whereas silicone elastomer PDMS (Sylgard® 184) was obtained from Dow Corning. All materials used in this study were employed without further purification. The NiO/PDMS-SA was fabricated using a liquid-phase exfoliation method involving an ultrasonication of NiO powders. Initially, the NiO powder was precisely weighed in varying increments, ranging from 1 mg to 30 mg, with a 3 mg incremental value. Subsequently, each weight of NiO powder was sonicated with 10 mL of THF using a probe sonication (Hielscher UP200s) for 2 hour to ensure a thorough dispersion. For instance, the mass concentration of 6 mg NiO in 10 mL of THF solvent can be defined as follows [155]:

$$\textbf{Concentration}\left(\frac{\textbf{g}}{\textbf{mL}}\right) = \frac{\textbf{mass of solute (g)}}{\textbf{volume of total solution (L)}}\ , \tag{4.1}$$

$$= \frac{6mg\ of\ NiO}{10mL\ of\ THF\ solvent} = 0.6\ \mathrm{m}g/\mathrm{m}L \tag{4.2}$$

Subsequently, 1 g of PDMS was incorporated into well-dispersed NiO solutions of various concentrations. The fabrication of the NiO/PDMS composite, which included stirring, curing, and degassing, was performed using the same procedure as described in Chapter 3 (refer to Figure 3.6). The spin-coating technique was then consistently applied to all the NiO/PDMS SAs while maintaining a speed of 4000 rpm for 5 minutes. This is to ensure a uniform thickness of the NiO/PDMS composite applied onto a tapered fibre. Prior to the NiO/PDMS deposition process, bare tapered fibre characterisation was performed following the steps presented in Chapter 3, Section 3.3 (refer to Figure 3.9). The bare tapered fibre loss was maintained at approximately in the range of 0.2 – 1.0 dB. The deposition process for each NiO concentration was carefully performed by applying a small drop of the NiO/PDMS composite solution to the waist region of the tapered fibre. Then, followed by the application of the spin-coating technique, as detailed out in Chapter 3 (see Figure 3.10). After the deposition and spin-coating processes were completed, the decorated tapered fibre with NiO/PDMS was cured by drying it under direct UV light exposure. Table 4.1 shows the curing period for the NiO/PDMS on a tapered fibre from 0.1 to 3.0 mg/mL with their respective laser performance. The curing period ranged from 1 to 20 weeks, depending on the NiO concentration. Higher concentrations of material in a polymer composite can potentially influence the kinetics of crosslinking owing to interactions between the NiO particles and the PDMS polymer chains during the curing process. At higher mass fractions, the surface encounters more particles before complete

solidification is achieved [156]. Thus, longer curing times are expected for higher material concentrations in a polymer.

Table 4.1 : NiO/PDMS Decorated on Tapered Fibre with Different Concentrations

NiO mass concentration in THF solvent (mg/mL)	NiO/PDMS based concentration	Curing period under sunlight	Remarks
0.1	SA-01	1 weeks	Not available, only CW
0.3	SA-03	2 weeks	Not available, only CW
0.5	SA-05	3 weeks	Not available, only CW
0.6	SA-06	3 weeks	Mode-locked spectrum at C band
0.9	SA-09	4 weeks	Mode-locked spectrum at C band
1.2	SA-12	5 weeks	Mode-locked spectrum at C band
1.5	SA-15	10 weeks	Mode-locked spectrum at C band
1.8	SA-18	14 weeks	Mode-locked spectrum at C band
2.1	SA-21	16 weeks	Mode-locked spectrum at C band
*2.5	SA-25	20 weeks	*Due to the impractical curing period, these SAs
*3.0	SA-30	More than 20 weeks	were not considered for testing in EDFL.

4.4 NiO/PDMS SA Functionality at Various Concentration and its Characterisation

4.4.1 Integration onto EDFL and Transmission Loss of Various NiO/PDMS SA

To evaluate the functionality of the NiO/PDMS-coated tapered fibre, it must be integrated in a laser cavity. Therefore, this fabricated device, starting with a concentration of 0.1 mg/mL and followed by other concentrations, was spliced between the SMF and PC, constituting the cavity configuration described in Chapter 3 (refer to Figure 3.13). Table 4.1 displays the laser performance obtained for the fabricated NiO/PDMS SA at various concentrations in the remarks column. Upon experimental observation, fine-tuning the orientation of the PC led to the generation of a CW laser without any pulses detected from the oscilloscope, signaling that NiO/PDMS tapered fibres within the concentration range of 0.1 to 0.5 mg/mL were incapable of inducing mode-locking in the laser cavity. This observation suggests that despite an increase in pump power, the desired mode-locked pulse state was not achieved.

In order to validate the transmission loss of the NiO/PDMS-coated tapered fibre with a concentration in the range of 0.1 – 0.5 mg/mL, a linear characterisation was done by implementing the experimental setup as discussed earlier (see Figure 3.9. Figure 4.5 (a) exhibits the measured transmission loss of those SA devices. Figure 4.5 (b) depicts an enlarged view of the average transmission loss within 1530-1580 nm wavelength of 1.08, 1.42 and 1.92 dB for SA-01, SA-03 and SA-05, respectively. The transmission loss results suggest that lower SA transmission losses, measured below 2 dB, can be attributed to insufficient material attachment within the specified concentration range.

With limited material attached to the tapered fibre, the evanescent field exhibits minimal interaction with the material, thereby reducing scattering and absorption. In contrast, higher concentrations, such as up to 0.6 mg/mL, result in increased material attachment. This enhances the interaction between the evanescent field and the material but may also lead to higher transmission losses, as elaborated below.

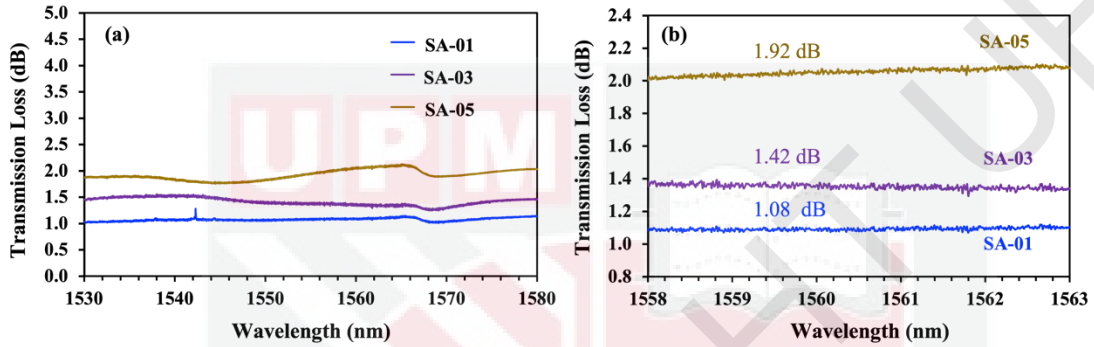

Figure 4.5 : Transmission Loss of (a) NiO SA-01 to SA-05 and (b) Enlarged Image of Wavelength 1558–1563 nm

Referring to Table 4.1, the mode-locking operation was attained for the concentration of NiO from 0.6 to 2.1 mg/mL. These findings support the evidence that the NiO material is able to induce mode-locking for the generation of ultrashort pulses. However, due to the extended curing time required for concentrations of 2.5 mg/mL and 3.0 mg/mL, these specific NiO concentrations were not considered for their integration into the EDFL cavity. Figure 4.6 (a) shows the transmission loss within the wavelength range of 1530-1580 nm for NiO/PDMS SA-06 to SA-21, which generated mode-locked pulses. Figure 4.6 (b) provides an enlarged view of the transmission loss of those devices. Specifically, the average transmission loss within the wavelength range of 1530-1580 nm increased from 2.74 dB (SA-06) to 5.03 dB (SA-18). The results indicated that with higher material concentrations in the composite, the transmission loss increased as well. This can be attributed to the fact that, as the

material concentration in the composite increases, both the scattering and absorption of incident light also increase, resulting in a higher transmission loss. However, the trend for SA-21 deviates due to significant agglomeration of the NiO/PDMS composite at this concentration, which will be further confirmed in the subsequenct section. The uneven particle distribution disrupted the uniformity of the coating, thereby altering the interaction between the evanescent field and the material. As a result, SA-21 exhibited a slightly lower transmission loss of 4.16 dB compared to the 5.03 dB loss observed for SA-18. Details on particle agglomeration, including images and justification, are provided in the SEM-EDX characterisation results presented below.

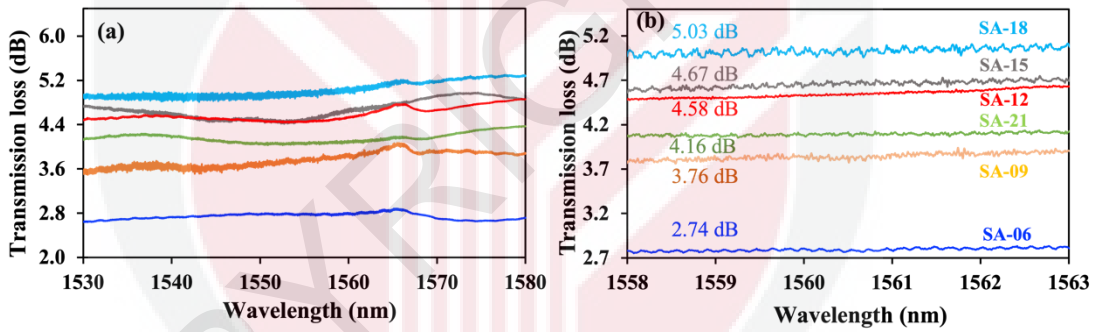

Figure 4.6 : Transmission Loss of (a) NiO/PDMS SA-06 to SA-18 and (b) Enlarged Image of y-axis (2.74 to 5.03 dB)

4.4.2 SEM-EDX Characterisation of Various Concentration NiO/PDMS SA

To further investigate the presence of NiO along the tapered fibre, NiO/PDMS samples with concentrations ranging from 0.1 to 0.5 mg/mL were chosen for the SEM-EDX characterisation. Figure 4.7 (a)-(f) show the SEM micrograph and EDX analysis along the tapered fibre for SA-01, SA-03, and SA-05. Based on the Figure 4.7 (b),(d) and (f) elemental analysis did not reveal the presence of NiO along the tapered fibre, indicating minimal or no material attachment. Previous studies have indicated that

insufficient concentrations of CNTs fail to induce the necessary saturable absorption, while excessively high concentrations result in significant agglomeration and bundling, leading to background losses and hindering the achievement of short pulses [157].

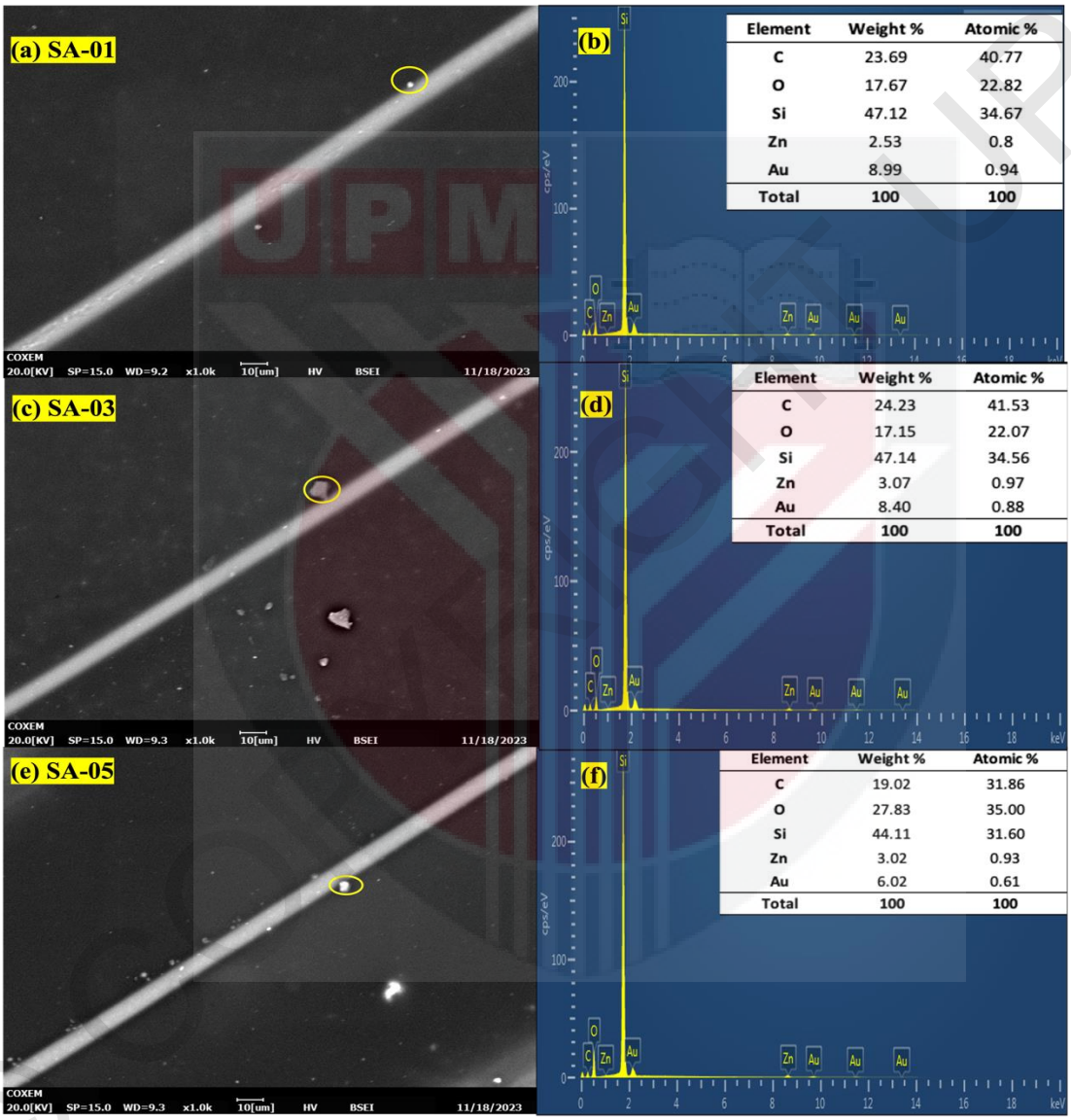

Figure 4.7 : SEM-EDX for SA-01, SA-03 and SA-05 (a) SEM Micrograph of NiO/PDMS with 0.1 mg/mL in Tapered Fibre, (b) Material Composition Detected in SA-01; (c) SEM Micrograph of NiO/PDMS in Tapered Fibre with 0.3 mg/mL (d) Material Composition Detected in SA-03 (e) SEM Micrograph of NiO/PDMS in Tapered Fibre with 0.5 mg/mL (f) Material Composition Detected in SA-05

Next, the NiO/PDMS-SA with 0.9, 1.5 and 2.1 mg/mL were selected for SEM-EDX characterisation. Figure 4.8 (a) shows that a few particles of NiO were detected along the waist region of the tapered fibre, highlighted by the yellow arrows in SA-09. The corresponding EDX analysis shown in Figure 4.8 (b) confirms the elemental composition. Notably, the Ni content with the weight percentage of 0.46%. Oxygen (O) and silicon (Si) were detected which originated from the glass substrate and silica fibre, respectively. The presence of carbon (C) is attributed to its common element in PDMS and carbon tape during sample preparations. Additionally, the detection of gold (Au) resulted from the gold sputter coating applied during the preparation of sample for the characterisation. Figure 4.8 (c) shows that several NiO particles were observed along the waist region, indicating an increment in the presence of NiO for SA-15. Figure 4.8 (d) presents its elemental analysis, verifying the successful deposition of NiO/PDMS onto the tapered fibre SA with a measured Ni content by its weight percentange of 0.63%.

Upon investigation, it was observed that at a concentration of 2.1 mg/mL, NiO particles had a higher tendency to agglomerate within the PDMS polymer composite than at lower concentrations. As shown in Figure 4.8 (e), larger particles were observed along the tapered fibre, whereas a few smaller particles were observed in the waist region. This phenomenon occurred because of the unique configuration of the waist region, where the tapered fibre sat on a substrate. Consequently, the NiO/PDMS composite accumulates in the free space between the fibre and the substrate, forming as a 'mountain ridge' structure [158]. Owing to gravitational forces, larger particles with a higher mass density tend to slide down from the top surface of the tapered fibre, leaving only smaller particles adhered to the waist region. Figure 4.8 (f) illustrates the

elemental composition of NiO, revealing a Ni content of 5.63% by weight percentage and other elements consistent with the elemental composition of the samples. Therefore, increasing the NiO concentration to 2.1 mg/mL possibly leads to greater agglomerations, which might have contributed to the escalated scattering losses within the SA, resulting in a total loss of SA functionality.

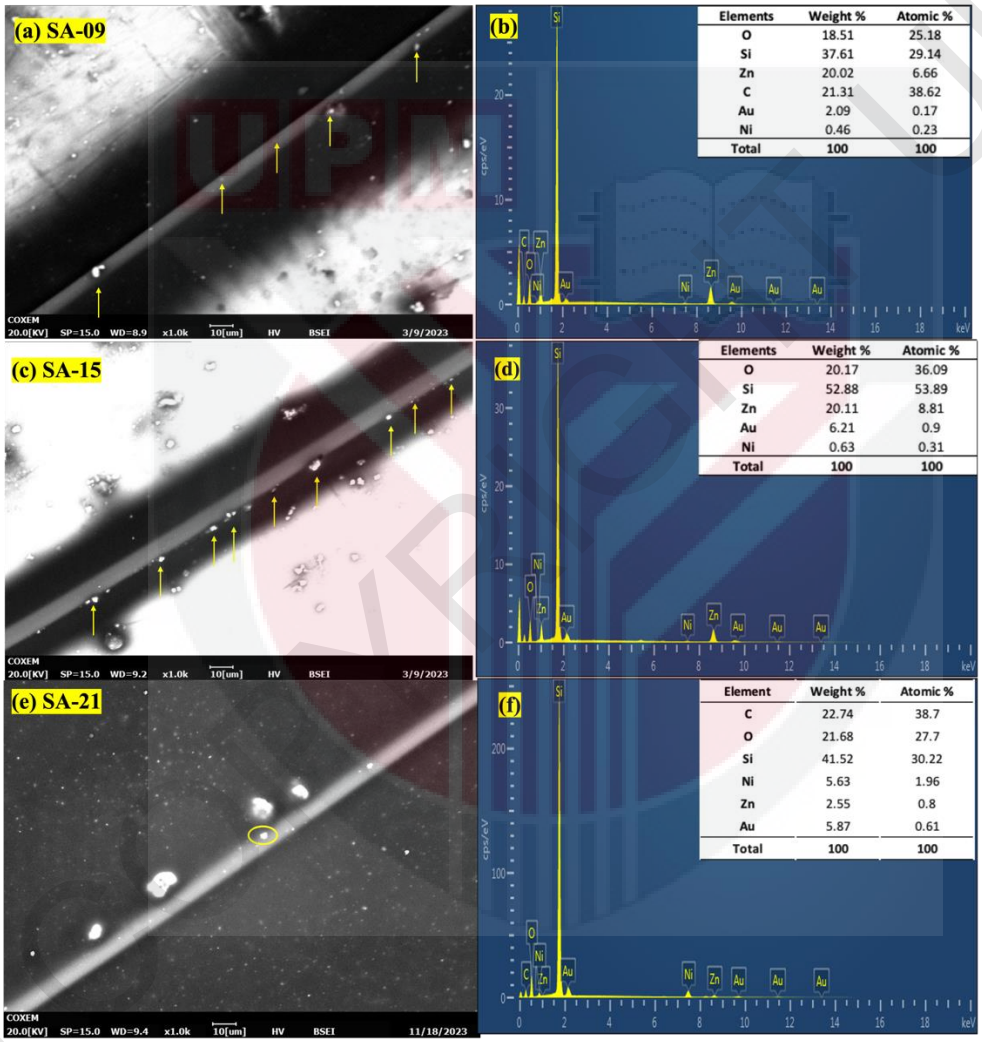

Figure 4.8 : SEM-EDX Analysis of NiO/PDMS SA at Different Concentrations: (a), (c), and (e) SEM Micrographs of NiO/PDMS SA along the Waist Region of Tapered Fibre for Concentrations SA-09, SA-15, and SA-21, Respectively. (b), (d), and (f), Corresponding Material Composition Detected in SA-09, SA-15, and SA-21, Respectively

4.4.3 Nonlinear Saturable Absorption Properties of Various Concentration NiO/PDMS SA

Subsequently, the nonlinear saturable absorption of the fabricated NiO/PDMS SA, from SA-06 to SA-21 that were succesfully induced ultrashort pulses, were measured using a balanced two-detector setup outlined in Chapter 3 (refer to Figure 3.12). Figure 4.9 demonstrates a slight increase in ΔT as the NiO concentration increased from SA-06 to SA-21. Table 4.2 summarizes the properties of the SA devices: ΔT, saturation intensity, and nonsaturable loss. The lowest ΔT value of 2.4%, was attained for SA-06, whereas the highest ΔT was obtained at 5.6% for SA-18.

This finding indicated that higher concentrations led to greater particle attachment onto the tapered fibre. When light propagates through an optical tapered fibre, the evanescent field extends beyond the fibre core and interacts with the surrounding medium [83]. As a result, an extensive absorption process occurs because of the interaction between the material properties and evanescent field [159]. This interaction saturates the NiO/PDMS-SA, resulting in a higher nonlinear absorption compared to SAs with lower NiO concentrations. Although increasing the concentration enhances the ΔT, it can also lead to higher α_{ns} [160]. This observation is supported by prior studies where higher concentrations of CNTs improved the ΔT [64], yet excessive amounts increased the scattering losses, thereby impacting the laser performance and which adds additional loss to the cavity and consequently, degrades laser performance [161].

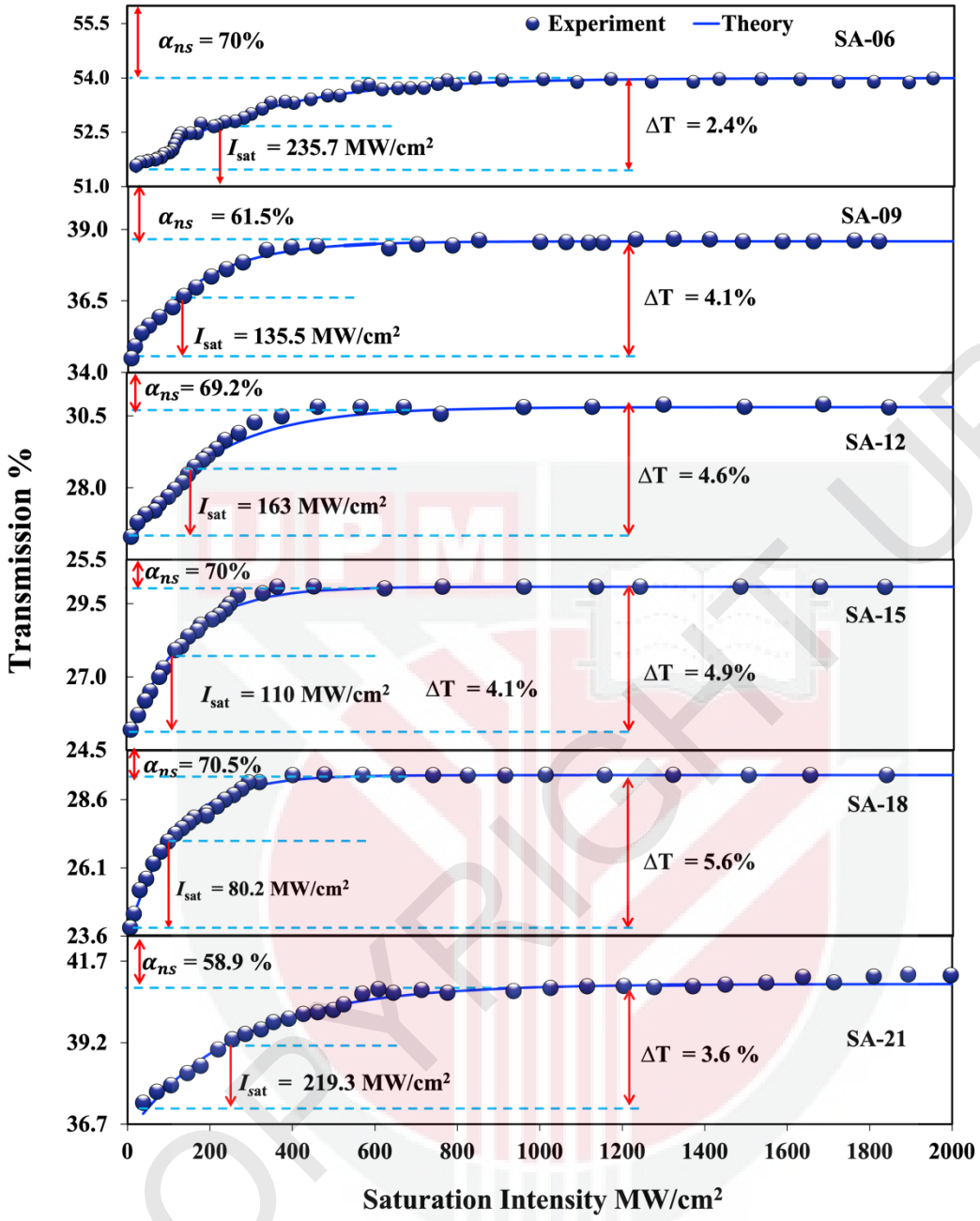

Figure 4.9 : Nonlinear Saturable Absorption for Different Concentrations of NiO/PDMS SA

Table 4.2 : Modulation Depths for Different NiO Concentrations of SA

SA	Modulation depth, ΔT (%)	Saturation intensity, I_{sat} (MW/cm^2)	Non-saturable loss, α_{ns} (%)
SA-06	2.4	235.7	46.1
SA-09	4.1	135.5	61.5
SA-12	4.6	163.0	69.2
SA-15	4.9	110.0	70.0
SA-18	5.6	80.2	70.5
SA-21	3.6	219.3	58.9

The value of α_{ns} started to enlarge from 46.1% (SA-06) to 70.5% (SA-18). These α_{ns} values were consistent with the transmission losses as depicted in Figure 4.9, highlighting the increase in SA loss with the increment in NiO concentrations. Regarding saturation intensity, the highest value recorded was 235.7 MW/cm² for SA-06, while the lowest one was 80.2 MW/cm² for SA-18. Notably, it was observed that I_{sat} experienced a slight decrease with an increase in ΔT. These results were similar to those reported in [162], where increasing the number of graphene layers increased the effective modulation, whereas the I_{sat} decreased with increasing number of graphene layers.

4.5 Effect of NiO Concentrations on Pulse Laser Performance

This section describes the analysis of ultrashort pulse generation using the fabricated NiO/PDMS-SA from 0.6 to 2.1 mg/mL of the NiO concentration. The goal is to investigate the influence of varying the NiO concentration on mode-locked pulse characteristics. The analysis encompasses an examination of the pulse spectrum, duration, and energy was evaluated by integrating the fabricated NiO/PDMS-SA in an EDFL. For this experiment, the laser cavity setup was kept constant throughout the study, as shown in the Chapter 3 (see Figure 3.13). A net GVD of -0.5323 ps^2 with an additional 24.2 m SMF length was implemented in this experiment.

4.5.1 Optical Spectrum of Continuous Wave Laser

Figure 4.10 (a) depicts the CW spectrum emission of NiO-SA ranging from SA-06 to SA-21, measured using an OSA with a resolution bandwidth of 0.02 nm. For all concentrations (SA-06, SA-09, SA-12, SA-15, SA-18, and SA-21), the CW laser emission began at 40 mW pump power. Figure 4.10 (b) shows an enlarged view of the lasing peaks at approximately 1558 - 1564 nm. Notably, there was a slight shift in the CW spectrum towards shorter wavelengths (from 1561.84 - 1558.82 nm).

The phenomenon of wavelength shift can be understood by the laser theory, whereby the laser emission is influenced by the net gain and loss in the laser cavity. When the laser cavity encountered high intracavity loss, the rate of population inversion enhanced correspondingly to compensate the total losses and achieve lasing [163]. In this circumstance, the emission wavelength shifted towards the region of higher gain (shorter wavelength). The finding of blue-shift in wavelength emission aligns well with the NiO/PDMS-SAs' loss characterised in Figure 4.6 and Table 4.2. However, the SEM image presented in Figure 4.8(e,f) show particles agglomeration of SA-21, leading to the reduction of material attachment onto the ultrathin tapered region and relatively lower loss as compared to SA-18 counterpart. Therefore, the CW emission of SA-21 and SA-18 are 1559.79 and 1558.82 nm, respectively.

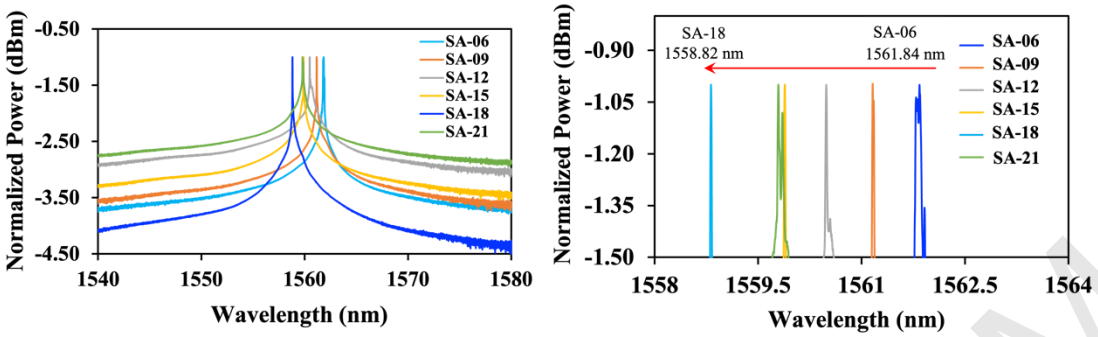

Figure 4.10 : (a) CW Laser Wavelength Spectrum for SA-06 to SA-21 and (b) Enlarged Spectrum from 1558 to 1564 nm Wavelength Range

4.5.2 Optical Spectrum of Mode-Locked Pulse Laser

Figure 4.11 and 4.12 present the optical spectrum for SA-06 to SA-21 along with their respective 3-dB spectral bandwidths under two conditions at; mode-locked threshold power and maximum pump power. Table 4.3 shows the specific values of the spectral bandwidth for SA-06 to SA-21. In the investigation, measurement of the 3-dB spectral bandwidth, involving a comparison between two distinct pump powers: mode-locked (ML) threshold and maximum pump power. The deviation values (Δ3dB bandwidth (nm)) in the table were derived from the difference between the ML threshold and maximum pump power. Notably, the spectral bandwidth exhibited minimal expansion with lower NiO concentrations of SA-06, at 0.06 nm compared to SA-21 at 0.30 nm (maximum spectral deviation).

Regarding the mode-locking threshold, Figure 4.11 (a)-(b) for SA-06 exhibited a mode-locked spectrum when the pump power reached 100 mW, whereas SA-21 (Figure 4.12 (e)-(f)) achieved mode-locking at 80 mW pump power. While SA-09, SA-12, SA-15, and SA-18 achieved mode locking at the lowest pump power of 50 mW. This variation in the mode-locking threshold may correspond to the I_{sat}

characteristics as discussed in Section 4.4.3. For SA-06 and SA-21, the measured I_{sat} were 235.7 MW/cm² and 219.3 MW/cm², respectively. These measured I_{sat} align with the higher ML threshold powers observed for both SAs (SA-06, 100 mW) and (SA-21, 80 mW). On the other hand, the I_{sat} values for SA-09 up to SA-18 were in the range (80 MW/cm^2 to 163 MW/cm^2) which justified the ML threshold power of 50 mW. According to [123], a lower I_{sat} indicates the requirement of a lower power threshold to achieve mode locking.

Overall, based on Figure 4.11 and 4.12 the comparison of Kelly sideband strength demonstrates that at the highest pump power of 250 mW, the spectral broadening was notable compared to the spectral behavior observed at the threshold pump power of 50 mW. Increasing the pump power causes the dispersive waves to build up and become strong, leading to a shift in the position of the new spectral component [164]. As mentioned in [165], the spectral broadening is caused by the complex interaction of gain, loss, dispersion, nonlinearity, and other effects that occur when the pump power is increased. The higher the pump power, the stronger the dispersive wave energy, which causes sub-sidebands to emerge at the maximal Kelly sideband. In terms of the lasing wavelength, SA-06 in Figure 4.11(c) has a central wavelength of 1561.94 nm, whereas the lasing wavelength for SA-18 in Figure 4.12(c) shifted to 1558.68 nm. The effect of wavelength shift is due to the increment of the cavity loss, that leads to a higher population inversion. As reported in a previous study [166], this was attributed to increased intracavity losses caused by the α_{ns} in the thicker layer of the graphene SA.

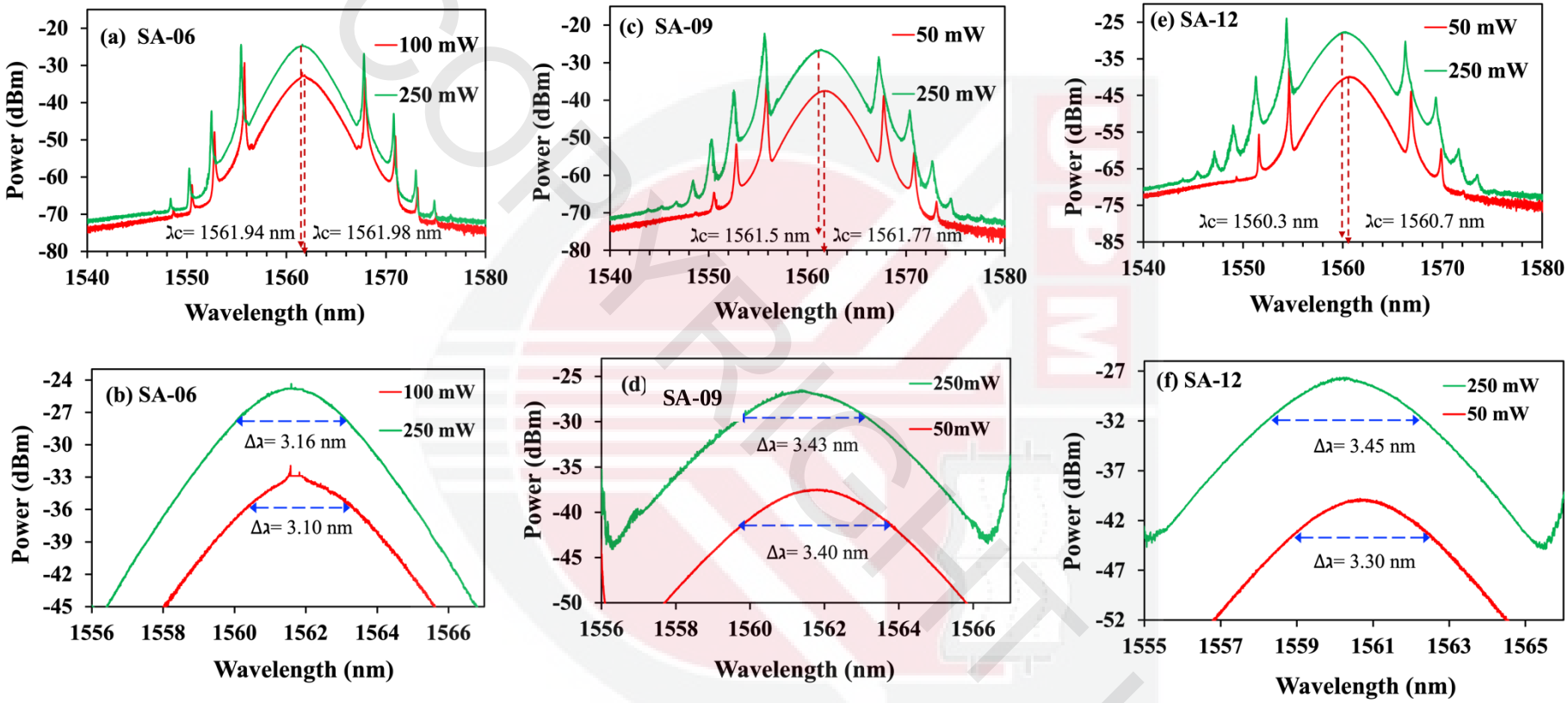

Figure 4.11 : Optical Spectrum for Threshold and Maximum Power Mode-Locking and its Respective 3-dB Bandwidth for (a) SA-06 (b) Enlarged View of SA-06 (c) SA-09 (d) Enlarged View SA-09 (e) SA-12 and (f) Enlarged View of SA-12

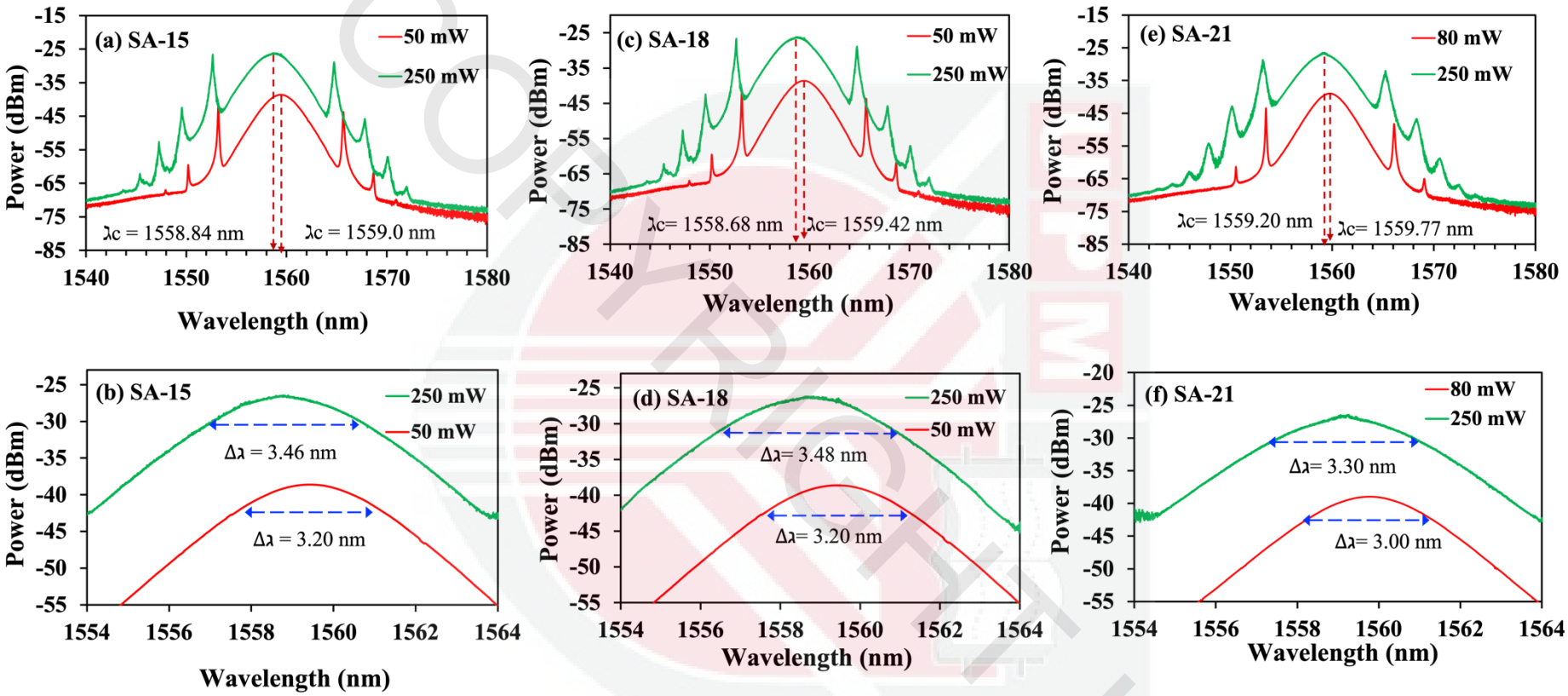

Figure 4.12 : Optical Spectrum for Threshold and Maximum Power Mode-Locking and its Respective 3-dB Bandwidth for (a) SA-15 (b) Enlarged View of SA-15 (c) SA-18 (d) Enlarged View SA-18 (e) SA-21 and (f) Enlarged View of SA-21

Table 4.3 : Optical Spectrum Properties of All SAs

SA	CW laser threshold power (mW)	Parameters at the mode-locked threshold power			Parameters at the maximum pump power		Δ3dB Bandwidth (nm)
		Threshold Power (mW)	Central Wavelength (nm)	3dB Bandwidth (nm)	Central Wavelength (nm)	3dB Bandwidth (nm)	
SA-06	40	100	1561.98	3.10	1561.94	3.16	0.06
SA-09	40	50	1561.77	3.40	1561.50	3.43	0.06
SA-12	40	50	1560.70	3.30	1560.30	3.45	0.15
SA-15	40	50	1559.02	3.20	1558.84	3.46	0.26
SA-18	40	50	1559.42	3.20	1558.68	3.48	0.28
SA-21	40	80	1559.77	3.00	1559.20	3.30	0.30

The investigation was extended to examine the optical spectrum concerning to pump power variations. Figure 4.13 and Figure 4.14 illustrate the optical spectrum behaviour from SA-06 to SA-21. These spectra were recorded as the pump power increased incrementally, around 10 mW intervals, up to a maximum value of 250 mW. Kelly's sidebands were evident across all spectra, confirming the operation of the generated soliton pulses within the anomalous dispersion regime [167]. Based on the findings, there were three different levels of threshold power to induce mode-locked pulses; 100 mW (SA-06), 50 mW (SA-09, SA-12, SA-15, SA-18), and 80 mW (SA-21). Subsequently, the pump power was elevated to its maximum value of 250 mW. This translated to higher circulating powers in the cavity that saturate the SA, resulting in a spectral broadening. This spectral broadening was attributed to the SPM effect, which concurrently resulted in achieving optimal pulse width durations [52]. Moreover, it can be seen that the general tendency of centre wavelength towards shorter wavelengths with the increase of the additional losses from SA-06 to SA-21. This trend aligns with the laser theory, illustrating how the population inversion condition directly impacts the emitted lasing wavelength [163].

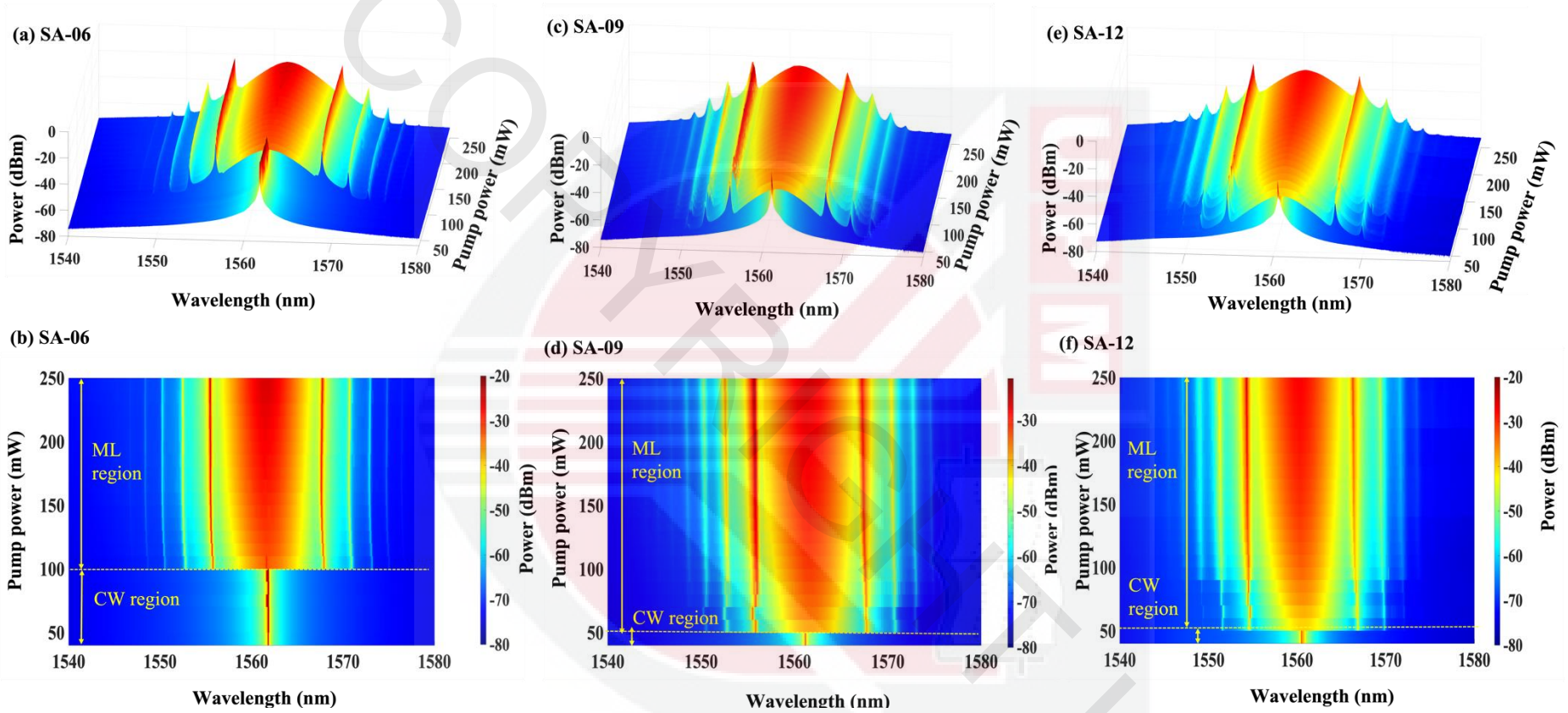

Figure 4.13 : Spectrogram of Mode-Locking Spectrum for (a) SA-06, (b) Top View of SA-06, (c) SA-09, (d) Top View of SA-09, (e) SA-12, and (f) Top View of SA-12

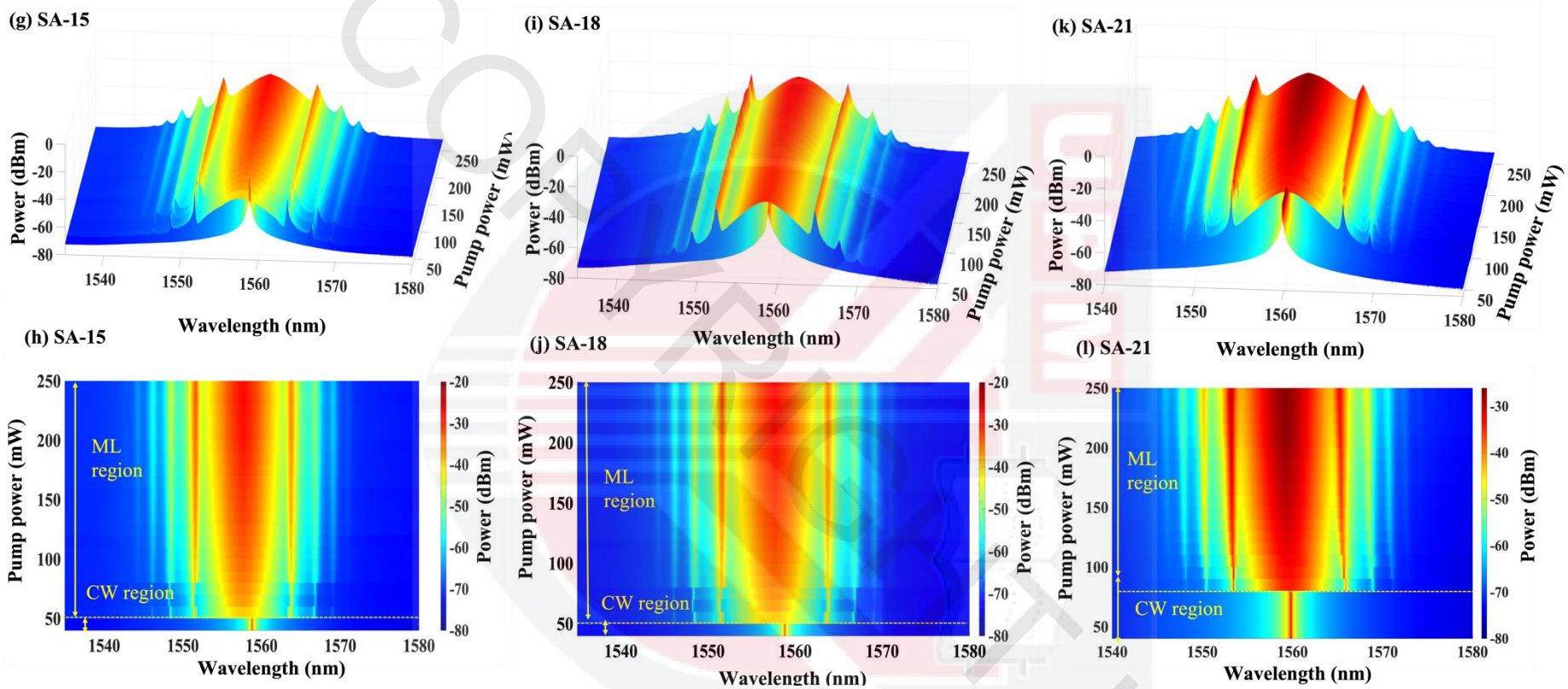

Figure 4.14 : Spectrogram of Mode-Locking Spectrum for (g) SA-15, (h) Top View of SA-15, (i) SA-18, (j) Top View of SA-18, (k) SA-21, and (l) Top View of SA-21

.

4.5.3 Oscilloscope Pulse Train

Figure 4.15 displays the oscilloscope trace of the mode-locked fibre laser for SA-06. A fundamental pulse train was achieved with a cavity length of ~ 24.2 metres, resulting in a repetition rate of 8.0 MHz (125 ns). The oscilloscope trace revealed no significant noise or fluctuations, indicating a stable laser operation. In addition, there were no indications of multiple pulsing or Q-switching effects. The measured pulse repetition rate remained the same throughout the experiment, despite the increment of the pump power. Observations also showed that all oscilloscope traces of different SA concentrations obtained a similar repetition rate of 8.0 MHz since no significant changes were observed in the fibre length. Further oscilloscope traces for different NiO concentrations of the fabricated SA are provided in Appendix H.

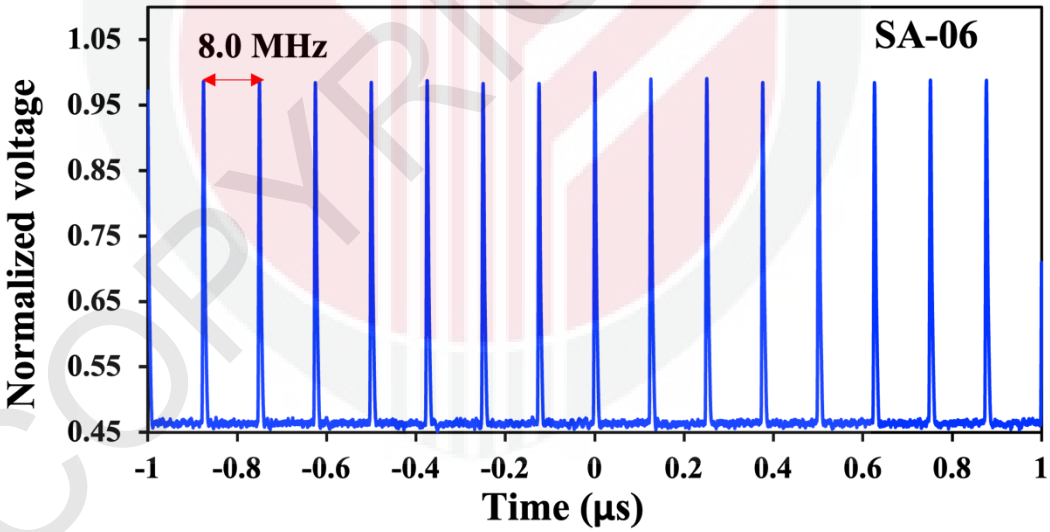

Figure 4.15 : Oscilloscope Trace of Pulse Laser Output Using SA-06

4.5.4 Peak-to-Pedestal Extinction Ratio (PER)

The stability of the mode-locked pulses for SA-06 was also assessed by measuring the PER of the RF spectrum, as shown in Figure 4.16. The RF spectrum analyser was configured with a 100 MHz scanning span and a 300 kHz resolution bandwidth for this experiment. From Figure 4.16, the first order peak has a PER value of 54.45 dB, indicating that the mode-locked fibre laser operated with good stability since its value is over 45 dB [168]. No Q-switching fluctuations were observed even when measured at the threshold pump power. Table 4.4 presents the values of the repetition rate and PER for all the NiO concentrations. The repetition rate was maintained at 8.0 MHz throughout all experimental sets, as carefully as possible. Based on these findings, similar repetition rates were obtained for all NiO/PDMS-SA, and the differences between the subsequent setups were very small. In addition, the highest PER value was obtained for SA-12 at 56.51 dB compared to the other PER values for different NiO concentrations. The experimental results of the RF spectrum for other NiO concentrations are attached in Appendix I.

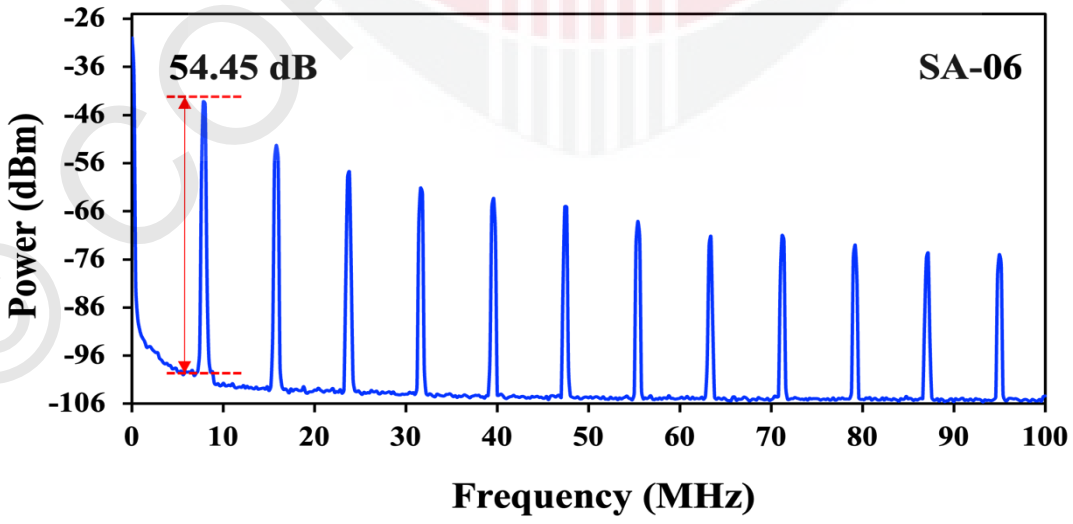

Figure 4.16 : RF Spectrum of Mode-Locked for SA-06

Table 4.4 : Repetition Rate and PER of the RF Spectrum for Each NiO Concentration SA

NiO/PDMS SA	PER (dB)
SA-06	54.45
SA-09	55.91
SA-12	56.51
SA-15	55.44
SA-18	55.92
SA-21	53.69

4.5.5 Pulse Duration and Time Bandwidth Product

Figure 4.17 (a)–(f) show the autocorrelator trace of the generated pulse at the threshold and maximum pump powers (250 mW) attained from SA-06 to SA-21, respectively. All the measured pulses were well fitted with the $sech^2$ fitting profile as presented in Table 4.5. The findings show that there were a slight decrease in the value of pulse widths (fs) when the NiO concentrations were increased from 0.6 to 1.8 mg/mL. The pulse width varied between 781 fs (SA-18), representing the shortest duration, and 858 fs (SA-6 mg), indicating a slower pulse. This trend aligns with higher NiO concentrations, showcasing shorter pulse widths attributed to the increment in the ΔT. According to [169], by adjusting the ΔT of the SA, the output pulse duration can be varied by more than a factor of three. However, the trend of shorter pulse widths was disrupted at the NiO concentration of 2.1 mg/mL. This interruption occurred due to the accumulation of NiO particles in SA-21, resulting in a smaller ΔT compared to SA-18 and other concentrations. Consequently, this led to a slightly slower pulse width of 820 fs, in contrast to the 781 fs observed in SA-18.

Table 4.5 provides the information of TBP, along with the corresponding pulse width, center wavelength, and 3-dB spectral bandwidth. The minimum TBP for bandwidth-

limited pulses is 0.315 for sech²-shaped pulses, indicating a minimal chirp tolerance. The correlation between the pulse duration and 3-dB bandwidth is crucial, as expressed in Equation 3.7 (Chapter 3). The inter-relationship between these two terms determines whether the pulse is near the ideal transform-limited pulses or heavily chirped. From this work, the SA-09 exhibited the highest TBP value of 0.340, indicating that the pulse was slightly chirped [170]. Nevertheless, the calculated TBPs showed a minimal variation, achieving a TBP value close to the transform-limited value. Additionally, it could indicate a well-maintained balance between the nonlinear and dispersive effects within the system [171].

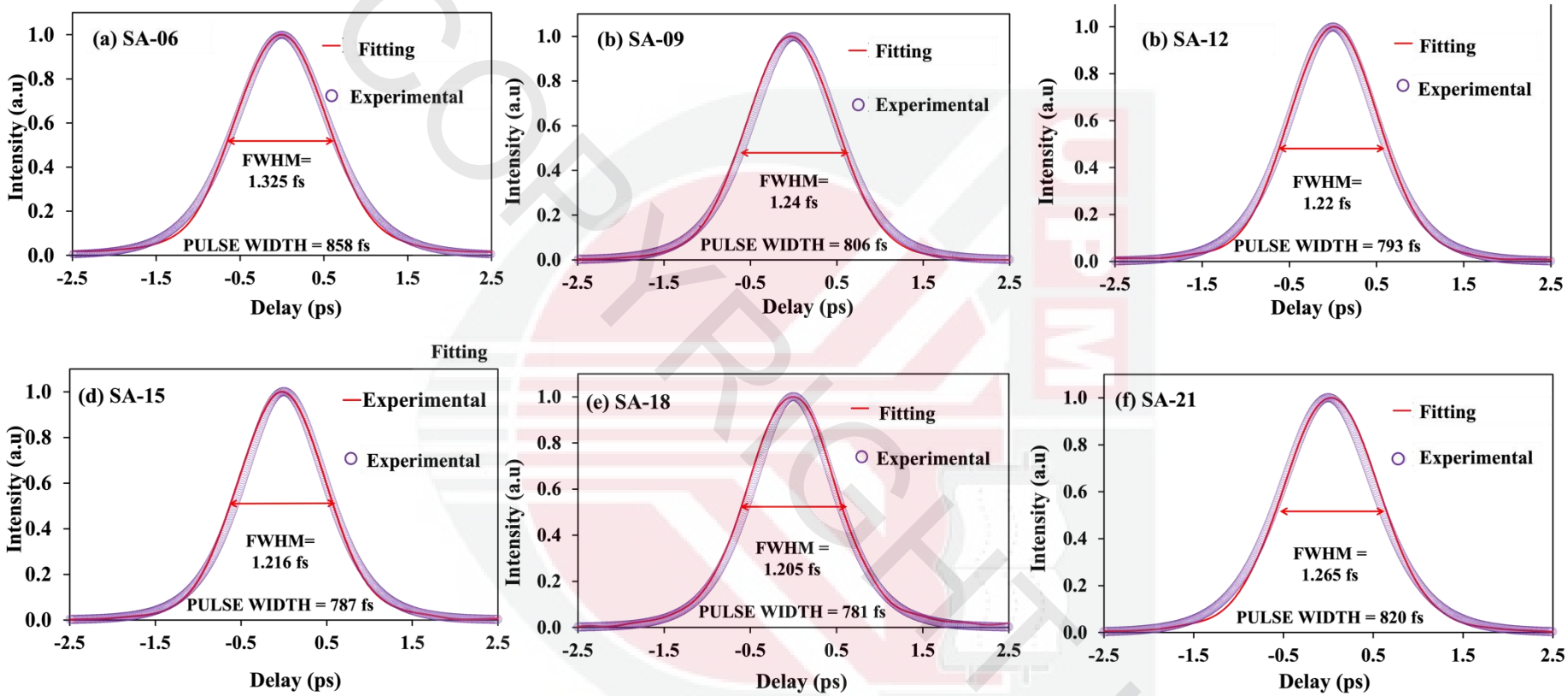

Figure 4.17 : Autocorrelation Traces at Maximum Pump Power for (a) SA-06, (b) SA-09, (c) SA-12, (d) SA-15, (e) SA-18, and (f) SA-21

Table 4.5 : Pulse Width, Spectral Bandwidth, Central Wavelength, and TBP at Maximum Pump Power

NiO/PDMS SA	Pulse width at maximum pump power (fs)	3-dB Spectral bandwidth at maximum pump power (nm)	Central Wavelength at maximum pump power (mW)	TBP
SA-06	858	3.16	1561.98	0.333
SA-09	806	3.43	1561.50	0.340
SA-12	793	3.45	1560.30	0.337
SA-15	787	3.46	1558.84	0.336
SA-18	781	3.48	1558.68	0.336
SA-21	820	3.30	1559.20	0.334

4.5.6 Average Output Power and Pulse Energy

Figure 4.18 (a)–(f) show the average output power and pulse energy against pump power for all the fabricated SAs with variation of NiO concentrations. The experimental results indicated a linear increase in both the average output power and pulse energy with a higher pump power. In addition, the CW lasing threshold is marked as a reference point in the figures. Notably, the SA-06 demonstrated the highest threshold power of 100 mW for mode locking, potentially attributed to its high I_{sat}, despite having the lowest transmission loss among the SAs.

The pulse energy was determined using Equation 3.6 (Chapter 3). SA-06 yielded the highest pulse energy at 0.91 nJ under maximum pump power, while the lowest pulse energy of 0.69 nJ was observed with SA-18. The reduction in the output power and pulse energy can be attributed to the increased insertion loss associated with higher NiO concentrations. By computing the gradients of the linear curves, the slope efficiencies for both the output power and the pulse energy can be plotted. These results indicated the highest slope efficiency at 3.18% and 4.42 nJ/W for the output

power and pulse energy, respectively, when SA-06 was utilised. As expected, the SA-18 exhibited the lowest slope efficiency owing to its higher transmission loss compared to the other concentrations, as outlined in Table 4.1.

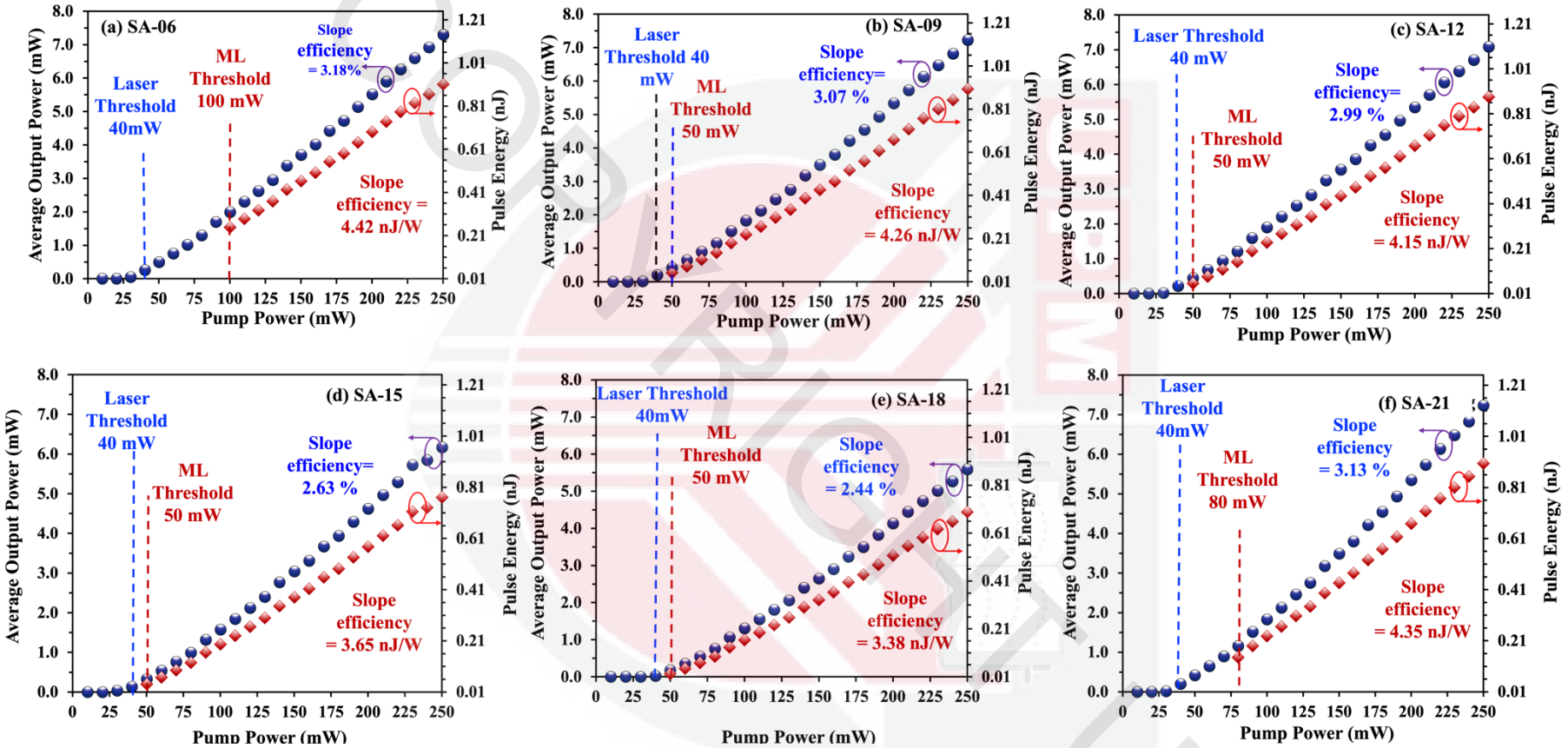

Figure 4.18 : Average Output Power and Pulse Energy against Input Pump Power for: (a) SA-06, (b) SA-09, (c) SA-12, (d) SA-15, (e) SA-18, and (f) SA-21

4.5.7 Optical Spectrum Stability and Autocorrelator Stability

To further assess the operational stability of the NiO/PDMS SA, the EDFL setup was operated at the maximum pump power with a constant polarisation state for a duration of 200 minutes. Throughout this period, the optical spectrum was recorded for every two minutes, as shown in Figure 4.19. For the purpose of discussion, only results obtained using the SA-06 are presented in this chapter. Based on the observation window, the corresponding 3-dB bandwidth and central wavelength were determined to be 3.29 ± 0.06 nm and 1561.44 ± 0.06 nm, respectively. Concurrently, the autocorrelator stability for pulse width performance was also assessed solely during the initial 60 minutes. Figure 4.20 (a) shows 3-D spectogram of normalised autocorrelator traces within 60 minutes. Figure 4.20 (b) depicts the average pulse width of 854.8 ± 4 fs for SA-06.

Table 4.6 depicts a summary of the averaged 3-dB spectral bandwidth, central wavelength, and pulse width, along with their respective standard deviations (SD), for all the NiO/PDMS SAs at different concentrations. The findings were consistent, without any significant variations within the observation window. Therefore, the stability of the proposed mode-locked EDFL with the NiO/PDMS SA was confirmed. Appendix J and Appendix K show the optical spectrum and auto correlator trace stability of the remaining NiO/PDMS SA at different concentrations respectively.

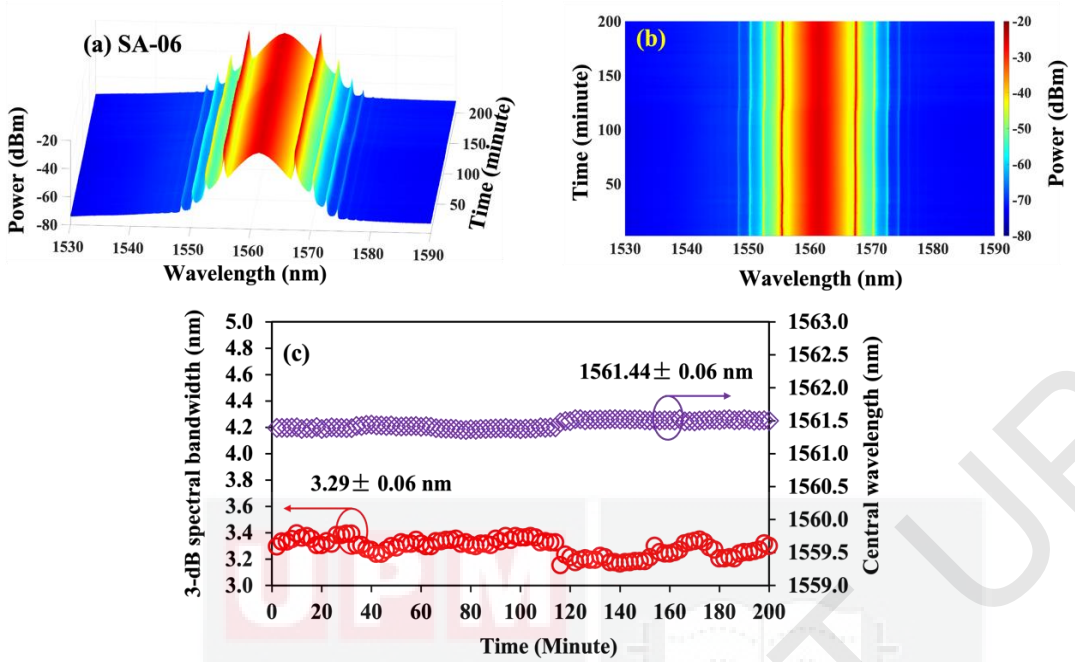

Figure 4.19 : Spectrum Stability for SA-06 (a) 3-D Spectrogram within 200 Minutes (b) Overview of (c) Measurements of 3-dB Bandwidth and Central Wavelength over 200 Minute

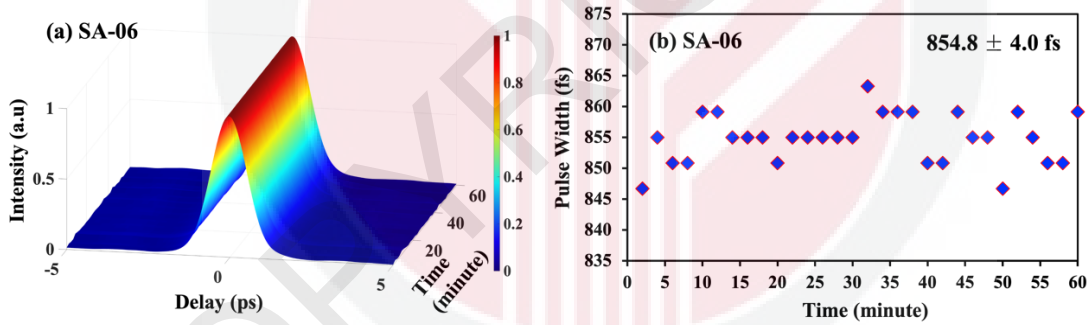

Figure 4.20 : Autocorrelator Trace Stability for SA-06 (a) 3-D Spectogram of Normalised Autocorrelator within 60 Minutes. (b) Pulse-Width (fs) Measurements within 60 Minutes

Table 4.6 : Summary of Optical Spectra and Auto-Correlator Stability for All NiO/PDMS Samples with Different Concentrations of SA

SA-NiO Concentr-ation	Average 3-dB spectral bandwidth (nm)	SD of Average 3-dB spectral bandwidth (nm)	Average Central Wavelength (nm)	SD of Average Central wavelength (nm)	Average Pulse Width (fs)	SD of Pulse width (fs)
SA-06	3.29	0.06	1561.44	0.06	854.8	4.0
SA-09	3.43	0.11	1561.29	0.07	804.7	2.7
SA-12	3.44	0.02	1560.28	0.01	798.1	4.2
SA-15	3.44	0.03	1558.62	0.03	793.3	3.9
SA-18	3.46	0.04	1558.90	0.06	788.5	6.0
SA-21	3.30	0.03	1559.26	0.04	809.4	6.6

4.6 Summary

The fabrication process of SAs with different NiO concentrations and their optical characterisation are discussed thoroughly in this chapter. The NiO concentration in THF was increased incrementally at intervals of 0.3 mg/mL from 0.1 to 3.0 mg/mL. The deposition of different concentrations of NiO/PDMS onto the tapered fibre surface was accomplished using a consistent spin-coating process; 4000 rpm at 5 minutes. The curing period of the NiO/PDMS composite on the tapered fibre was highly dependent on the NiO concentration. The optimal curing period, with a maximum of 4 weeks, was found for NiO/PDMS concentrations below 0.9 mg/mL. Previous reports had fabricated SA within 3-4 days to perform the thin-film casting method [172], whereas the thin film drop cast in the previous study dried within 3 days [173]. Increasing the NiO concentration further led to an excessively prolonged curing process, making it impractical for SA fabrications.

The characteristics of different NiO/PDMS SA concentrations are summarized in Table 4.7. The results show a slight increase in ΔT with higher NiO concentrations. The highest ΔT 5.6%, was recorded for SA-18. However, the ΔT for a NiO

concentration of 2.1 mg/mL was 3.6%, which is lower than the ΔT for 1.8 mg/mL. These findings indicated that excessive amounts of NiO can lead to material wastage owing to the particle agglomeration, thereby restricting attachment of smaller particles on the tapered fibre. Figure 4.21 (a) depicts the α_{ns} and ΔT as a function of the NiO concentration. This indicates that the nonsaturable loss is linearly related to the ΔT and increases proportionally with the loss of the SA. In addition, the size of the bubbles in the graph represents the curing time of the NiO/PDMS SA. As observed in the figure, higher concentrations of NiO correspond to longer curing times, and the increase in curing time for the SA is directly associated with the higher α_{ns} observed.

Table 4.7 : Summarize of Non-Linear Characteristics and ML-EDFL Performances of Differents NiO Concentrations

Characteristics	SA-06	SA-09	SA-12	SA-15	SA-18	SA-21
NiO Concentration in 10 mL THF	6 mg	9 mg	12 mg	15 mg	18 mg	21 mg
Transmission Loss (dB)	2.74	3.76	4.58	4.67	5.03	4.16
ΔT (%)	2.4	4.1	4.6	4.9	5.6	3.6
α_{ns} (%)	46.1	61.5	69.2	70.0	70.5	58.9
I_{sat} (MW/cm^2)	218.0	135.5	163.0	110.0	80.2	219.3
ML Threshold power (mW)	100	50	50	50	50	80
3dB bandwidth at highest pump power (nm)	3.16	3.43	3.45	3.46	3.48	3.32
Central wavelength (nm) at highest pump power	1561.98	1561.50	1560.30	1558.84	1558.68	1559.20
Pulse duration (fs) at highest pump power	858	806	793	787	781	820
Average TBP	0.333	0.340	0.337	0.336	0.336	0.336
Output power (mW) at highest pump power	7.30	7.23	7.08	6.17	5.59	7.23
Pulse energy (nJ) at highest pump power	0.91	0.90	0.89	0.77	0.69	0.90
Slope efficiencies: Average output power (%)	3.18	3.07	2.99	2.63	2.44	3.13
Slope efficiencies: Pulse Energy (nJ/W)	4.42	4.26	4.15	3.65	3.38	4.35

Note: THF= tetrahyrofuran, ΔT = modulation depth, α_{ns}= non-saturable loss, ML = mode-locked , TBP = time-bandwidth-product

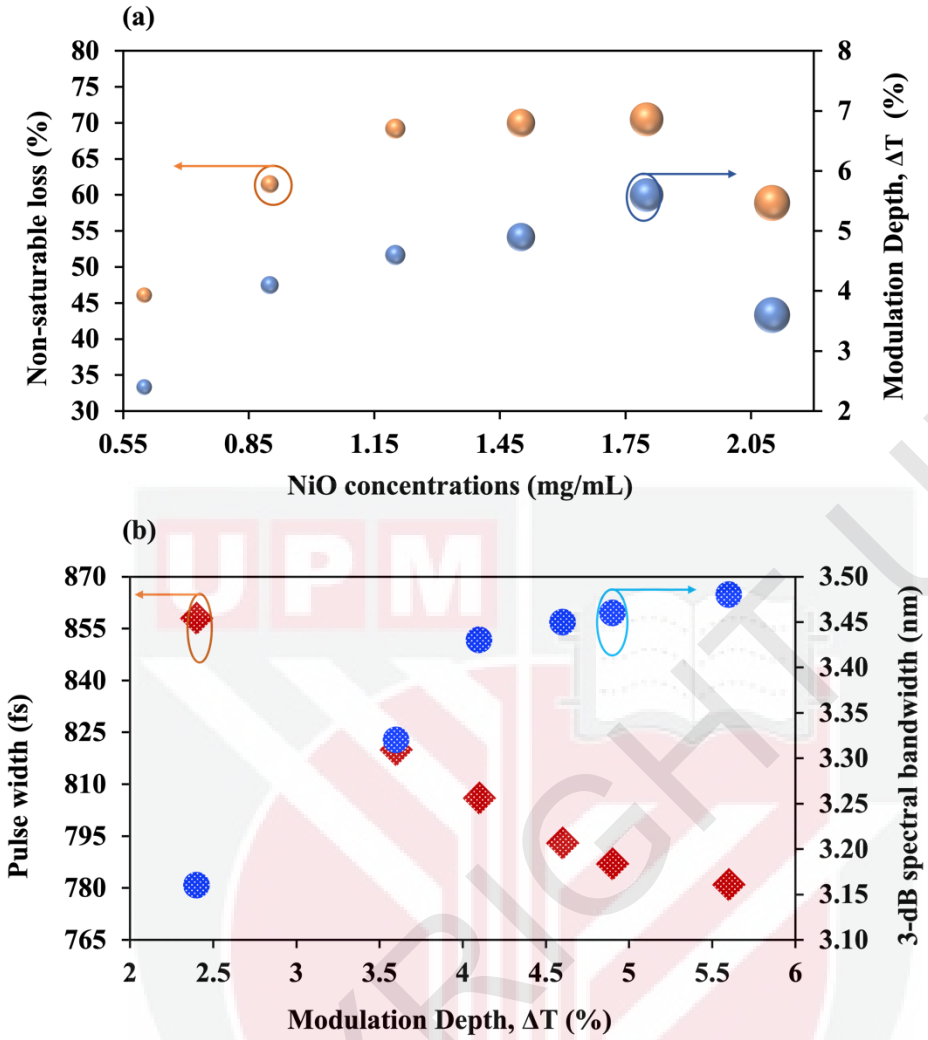

Figure 4.21 : Modulation Depth of NiO/PDMS SA Relationship (a) SA Transmission Loss (dB) and Non-Saturable Loss %. (b) Pulse Width Shortening (fs) and 3-dB Spectral Bandwidth Broadening (nm)

As the transmission losses of the SA increased, the pulse energy decreased accordingly. These results are similar to those reported by [174] [157], which highlighted the dependence of a SA's modulation depth on variables such as the thickness and concentration of the CNT. Another finding is that the optical spectra and pulse width evolution versus the ΔT are shown in Figure 4.21 (b). The 3-dB spectral bandwidth of different NiO/PDMS SA broadened from 3.16 nm (SA-06) to 3.48 nm (SA-18). In contrast, the corresponding pulse width decreased from 858 fs (SA-06) to 781 fs (SA-18). The relationship between the pulse width and spectral bandwidth can

be explained by Fourier transform, whereby in the frequency domain, the pulse duration is inversely proportional to the spectral bandwidth [148]. In terms of the ML threshold for different NiO concentrations, the findings revealed that the pump power threshold was the highest for the sample with the lowest NiO concentration and decreased for samples with higher NiO concentrations. As the ΔT increased with the concentration, the I_{sat} decreased. This can be seen the ΔT increased from 2.4% (SA-06) to 5.6% (SA-18) while the I_{sat} obtained lower from 235.7.0 MW/cm^2 (SA-06) to 80.2 MW/cm^2 (SA-18), respectively. The lower I_{sat} indicates that the mode-locking is easier to induce ins the fibre laser cavity. The higher ML threshold of SA-06 and SA-21 might be translated from the higher I_{sat} in the nonlinear characteristic of SA. A lower I_{sat} indicates the requirement of a lower threshold to achieve mode-locking [123]. In terms of stability, all samples demonstrated good stability, with SA-12 exhibiting the highest PER value. Although a larger ΔT is often associated with a better PER, in this case, it is also associated with a larger α_{ns}.

CHAPTER 5

CONCLUSION AND FUTURE RECOMMENDATION

This chapter summarises the overall research work and findings of this study. The major findings, research contributions and suggestions for future work are outlined.

5.1 Conclusion

This study has successfully met its objectives by fabricating and characterising Ni/PDMS and NiO/PDMS composites on tapered fibres using the spin-coating technique to serve as SAs. This study thoroughly analysed the pulse performance of Ni/PDMS-SA by varying the net dispersion in a ring-cavity EDFL, providing insightful data on the effect of dispersion on the laser performance. Additionally, an investigation into the influence of varying NiO/PDMS-SA concentrations within the ring-cavity EDFL revealed critical information about the impact of different SA concentrations on pulse performance.

The major findings of this study are as follows:

- Ni/PDMS and NiO/PDMS SAs were successfully fabricated on tapered fibres using spin-coating techniques. As a result, Ni/PDMS produced mode-locked pulse lasers with femtosecond durations ranging from 745 to 886 fs, while NiO/PDMS achieved durations between 781 to 858 fs. Performance evaluation showed that the Ni/PDMS-SA at a concentration of 0.6 mg/mL achieved a ΔT of 4.77%, demonstrating its strong capability to modulate pulse lasers. In contrast, the NiO/PDMS-SA at the same concentration exhibited a ΔT of 2.4%.

- By varying the net dispersion in the EDFL revealed that longer SMF lengths led to a narrower 3-dB spectral bandwidth and longer pulse widths, from 3.98

to 2.91 nm and 745 to 886 fs, respectively. The optimal result, achieved with an additional SMF length of 24.2 metres, yielded the highest PER measurement of 57.55 dB, demonstrating good pulse stability. This length was then utilised in the EDFL cavity to address the third objective of this study. Consequently, this EDFL cavity with the Ni/PDMS SA could achieve a fundamental pulse with an SMF length of at least 22.6 metres.

- The effect of NiO concentrations ranging from 0.1 to 3.0 mg/mL, on laser performance was investigated. The optimal concentration range was identified as 0.9 to 1.2 mg/mL, striking a balance between the increased NiO concentration, SA transmission loss, curing time, and the NLO characteristics of the SA. At lower NiO concentrations (0.1 to 0.5 mg/mL), insufficient deposition of NiO along the tapered fibre led to inadequate interaction with the evanescent field, which prevented the SA from inducing mode-locking. On the other hand, higher concentrations of NiO (above 2.5 mg/mL) significantly enhanced the crosslinking kinetics with the polymer matrix. This resulted in excessively prolonged curing periods, often exceeding 20 weeks, rendering these concentrations impractical for efficient SA fabrication and use.

- Therefore, the concentration range of 0.9 to 1.2 mg/mL was deemed optimal as it provided sufficient NiO deposition for mode-locking, moderate transmission loss, and reasonable curing times without compromising the nonlinear performance of the SA. Additionally, employing a 2.1 mg/mL concentration of NiO resulted in a ΔT value of 3.6%, which was slightly lower than that of 1.8 mg/mL (SA-18). These findings suggest that excessive NiO concentrations can lead to material wastage owing to particle agglomerations, which restricts particle attachment to the tapered fibre.

4. The findings also highlight the significant impact of increasing NiO concentration on ΔT, which directly influences the pulse width. As the NiO concentration increased from 0.6 to 1.8 mg/mL, there was a corresponding rise in ΔT, as evidenced by the increase in ΔT from 2.4% for SA-06 to 5.6% for SA-18. These resulted in a broadening of the 3-dB spectral

bandwidth from 3.16 nm (SA-06) to 3.48 nm (SA-18), while also reducing the pulse width from 858 fs (SA-06) to 781 fs (SA-18).

5.2 Outcome and Research Contribution

This study has yielded several significant contributions to the field of pulsed lasers. The author conducted a detailed analysis of the experimental results involving a novel SA using tapered fibres coated with Ni/PDMS and NiO/PDMS composites.

The main contributions of this study are as follows.

- The Ni/PDMS and NiO/PDMS SAs significantly contribute to the generation of stable mode-locked pulse lasers with femtosecond durations. Their ability to generate shorter pulse durations compared to existing Ni and NiO based SAs highlights their potential for applications requiring high precision and ultrafast operation in fields such as telecommunications, biomedical imaging, and materials processing.
- This study optimised the SMF lengths in the EDFL cavity by incorporating a Ni/PDMS SA. The findings serve as a guideline for tailoring the fibre lengths to achieve the desired pulse characteristics in future EDFL configurations.
- This study optimised NiO concentration to enhance SA performance within the EDFL cavity, addressing challenges related to curing times and offering practical guidelines for future SA fabrication and applications. This work reveals a trade-off between SA transmission loss, nonlinear characteristics, and pulse performance, offering insights into how material concentration, ΔT, spectral bandwidth, pulse width, and SA stability influence.

5.3 Suggestion for Future Work

This study contributes to the optimisation of two materials, Ni and NiO, in the context of optimising the dispersion effect and investigating the influence of NiO concentrations. As the investigation unfolded, several ideas for future research emerged. The recommendations are as follows:

- Exploring the effect of different Ni and NiO particle sizes could be an avenue for future research. Additionally, investigating the varied calcination processes of Ni and NiO materials, where higher calcination might enhance crystallinity and potentially influence nonlinear characteristics, which could further impact the laser pulse performance.
- In addition to the erbium-doped fibre commonly used in the 1.55 μm wavelength region, alternatives such as Thulium and Holmium for the 2 μm wavelength region in conjunction with Ni or NiO materials could be considered. Moreover, investigating the 1.0 μm wavelength region utilising ytterbium as the doped fibre presents another intriguing option that might offer unique characteristics for pulse laser applications.
- Implementing a net normal dispersion within a cavity can potentially lead to the generation of dissipative waves or Noise-Like Pulses (NLPs). Dissipative waves, or NLPs, are solitons that differ from CS. Dissipative waves arise from a delicate balance between the nonlinearity and normal dispersion. Exploring this avenue may provide insights into novel pulse dynamics and broaden the understanding of the soliton behaviour within the laser cavity.

REFERENCES

[1] "Alghamdi, T. A., & Harun, S. W. (2024). Ultrashort pulse generation with a Black Phosphorus Thin Film Absorber. IEEE Access, 12, 126915–126920. https://doi.org/10.1109/access.2024.3455437".

[2] "Wang, H., Jiang, C., Chu, H., Dai, H., Fu, B., Lu, S., & Zhang, Z. (2022). SiO2 Passivated Graphene Saturable Absorber Mirrors for Ultrashort Pulse Generation. Nanomaterials, 13(1), 111. https://doi.org/10.3390/nano13010111".

[3] P. C. Debnath and D. Il Yeom, "Ultrafast fiber lasers with low-dimensional saturable absorbers: Status and prospects," *Sensors*, vol. 21, no. 11, pp. 1–32, 2021, doi: 10.3390/s21113676.

[4] "Ahmed, M. H. M., N. Mohd Yusoff, Che, Alresheedi, M. T., Natrah Shafiqah Rosli, Zainal Abidin Talib, & Mohd Adzir Mahdi. (2021). Nanosized titanium dioxide saturable absorber for soliton mode-locked thulium-doped fiber laser. Results in Physics, 31, 104930–104930. https://doi.org/10.1016/j.rinp.2021.104930".

[5] "Dhara, A. (2024). SYNTHESIS AND ELECTRICAL TRANSPORT PROPERTIES OF METAL OXIDE NANOMATERIALS. Futuristic Trends in Chemical Material Sciences & Nano Technology Volume 3 Book 8, 164–168. https://doi.org/10.58532/v3becs8p4ch3 ".

[6] "Galtsov, I. S., Fokin, V. B., Dorovatovsky, A. V., Paramonov, M. A., Demyanov, G. S., Minakov, D. V., Sheindlin, M. A., & Levashov, P. R. (2024). Thermophysical properties of solid and liquid nickel near melting point. Journal of Applied Physics, 136(14). https://doi.org/10.1063/5.0234884".

[7] "Cattaneo, E., & Riegel, B. (2024). Chemistry and Electrochemistry | Nickel (pp. 740–761). Elsevier. https://doi.org/10.1016/B978-0-323-96022-9.00073-6 ".

[8] "Salah, A., Ren, H.-D., Nabilah Al-Ansi, Adel Al-Salihy, Qaraah, F. A., Mahyoub, S. A., Ahmed, A. A., & Drmosh, Q. A. (2024). Interface Engineering Induced by Low Ru Doping in Ni/Co@NC Derived from Ni-ZIF-67 for Enhanced Electrocatalytic Overall Water Splitting. ACS Applied Materials & Interfaces. https://doi.org/10.1021/acsami.4c13769".

[9] "Annealing Effect on Nickel Oxide Nanoparticles Properties. (2023). Jordan Journal of Physics, 16(3), 373–380. https://doi.org/10.47011/16.3.12".

[10] A. A. Ahmed, M. Devarajan, and N. Afzal, "Fabrication and characterization of high performance MSM UV photodetector based on NiO film," *Sens Actuators A Phys*, vol. 262, pp. 78–86, Aug. 2017, doi: 10.1016/j.sna.2017.05.028.

[11] W. , M. T. , Y. Y. , Z. C. , C. J. , C. L. , Z. W. , & F. B. Lyu, "Nickel Nanoparticles as Broadband Saturable Absorbers for Ultrafast Photonics. ," *ACS Appl Nano Mater*, vol. 7, no. 7, pp. 8221–8228, 2024.

[12] A. M. Salman and A. Al-Janabi, "Ni-NPs doped PVA: An efficient saturable absorber for generation multiwavelength Q-switched fiber laser system near 1.5 μm," *Opt Mater (Amst)*, vol. 98, pp. 109418–109418, Dec. 2019, doi: 10.1016/j.optmat.2019.109418.

[13] A. M. Salman and A. Al-Janabi, "Nickel Nanoparticles Saturable Absorber for Multiwavelength Pulses Generation in Ytterbium-Doped Fiber Laser," *Fiber and Integrated Optics*, vol. 39, no. 3, pp. 109–121, 2020, doi: 10.1080/01468030.2020.1768607.

[14] H. Ahmad, S. A. Reduan, and N. Yusoff, "Chitosan capped nickel oxide nanoparticles as a saturable absorber in a tunable passively Q-switched erbium doped fiber laser," *RSC Adv*, vol. 8, no. 45, pp. 25592–25601, 2018, doi: 10.1039/c8ra04380a.

[15] A. Nady, M. H. M. Ahmed, A. A. Latiff, A. Numan, C. H. Raymond Ooi, and S. W. Harun, "Nickel oxide nanoparticles as a saturable absorber for an all-fiber passively Q-switched erbium-doped fiber laser," *Laser Phys*, vol. 27, no. 6, pp. 1–6, 2017, doi: 10.1088/1555-6611/aa6bd7.

[16] A. N. A. Nady, M. H. M. A. M. H. M. Ahmed, A. A. L. A. A. Latiff, C. H. R. O. C. H. Raymond Ooi, and S. W. H. S. W. Harun, "Femtoseconds soliton mode-locked erbium-doped fiber laser based on nickel oxide nanoparticle saturable absorber," *Chinese Optics Letters*, vol. 15, no. 10, pp. 100602–100602, 2017, doi: 10.3788/col201715.100602.

[17] K. Y. Lau and D. Hou, "Recent research and advances of material-based saturable absorber in mode-locked fiber laser," *Opt Laser Technol*, vol. 137, no. November 2020, p. 106826, 2021, doi: 10.1016/j.optlastec.2020.106826.

[18] L. Dai *et al.*, "Carbon nanotube mode-locked fiber lasers: recent progress and perspectives," 2020, *De Gruyter Open Ltd*. doi: 10.1515/nanoph-2020-0446.

[19] P. He *et al.*, "Preparation of tellurium nanowires and its application in ultrafast photonics," *J Lumin*, vol. 252, Dec. 2022, doi: 10.1016/j.jlumin.2022.119335.

[20] D. Kang, S. Sarkar, K. S. Kim, and S. Kim, "Highly Damage-Resistant Thin Film Saturable Absorber Based on Mechanically Functionalized SWCNTs," *Nanoscale Res Lett*, vol. 17, no. 1, 2022, doi: 10.1186/s11671-021-03648-2.

[21] E. K. Ng *et al.*, "Optimization process of spin-coated black phosphorus/polydimethylsiloxane composite on microfiber as saturable absorber for ultrafast photonics," *Infrared Phys Technol*, vol. 130, May 2023, doi: 10.1016/j.infrared.2023.104578.

[22] R. I. Woodward, "Dispersion engineering of mode-locked fibre lasers," Mar. 01, 2018, *IOP Publishing Ltd*. doi: 10.1088/2040-8986/aaa9f5.

[23] “Nornormey, E. A., Nelson, N. A., Asare, E., Opoku-Akyea, D., Okpoti, F., & Reine Makafui McEben-Nornormey. (2024). The Effect of Dispersion and Attenuation on Fiber Optic Communication Systems. International Journal of Research and Innovation in Applied Science, IX(VIII), 343–378. https://doi.org/10.51584/ijrias.2024.908032 ”.

[24] “Trujillo, A., Gomez, G., & Zemanate, A. (2020). Algorithm for the dynamic compensation of Chromatic Dispersion in XGS-PON network architecture. IOP Conference Series: Materials Science and Engineering, 844, 012048. https://doi.org/10.1088/1757-899x/844/1/012048 ”.

[25] Shivinder Devra and Gurmeet Kaur, “Different Compensat ion Techniques To Compensate Chromatic Dispersion In Fiber Optics,” 2011.

[26] S. G. Sazonkin *et al.*, “Analysis of the Passive Stabilization Methods of Optical Frequency Comb in Ultrashort-Pulse Erbium-Doped Fiber Lasers,” Oct. 01, 2022, *MDPI*. doi: 10.3390/fib10100088.

[27] “Islam, Md. I., & Islam, M. S. (2020). Highly negative dispersion compensating fiber with low third order dispersion. Journal of Optical Communications, 0(0). https://doi.org/10.1515/joc-2020-0159 ”.

[28] “Irawan, D., Azhar, A., & Ramadhan, K. (2022). High-Performance Compensation Dispersion with Apodization Chirped Fiber Bragg Grating for Fiber Communication System. Jurnal Penelitian Pendidikan IPA, 8(2), 992–999. https://doi.org/10.29303/jppipa.v8i2.1521 ”.

[29] “Ekaterina Iordanova, Pavlina Miteva, Dakova, D., Chamati, H., Georgi Yankov, Georgieva, D. A., & Kovachev, L. M. (2024). Linear and Nonlinear Optics of Broad-Band Laser Pulses: Diffraction. ACS Omega, 9(19), 20648–20657. https://doi.org/10.1021/acsomega.4c02996 ”.

[30] Kaertner Franz X., “Chapter 3 Nonlinear Pulse Propagation,” 2005.

[31] T. Ilavarasan and M. Meenakshi, “An overview of fiber dispersion and nonlinearity compensation techniques in optical orthogonal frequency division multiplexing systems,” *Journal of Optics (India)*, vol. 44, no. 3, pp. 255–270, Sep. 2015, doi: 10.1007/s12596-015-0254-9.

[32] S. Kumar Orappanpara Soman, “A tutorial on fiber Kerr nonlinearity effect and its compensation in optical communication systems,” *Journal of Optics (United Kingdom)*, vol. 23, no. 12, Dec. 2021, doi: 10.1088/2040-8986/ac362a.

[33] “Moss, D. (2024). Graphene oxide for efficient self-phase modulation in silicon nitride nanowire waveguides. https://doi.org/10.31219/osf.io/ub598 ”.

[34] “Paschotta, D. R. (n.d.). self-phase modulation. Www.rp-Photonics.com. https://www.rp-photonics.com/self_phase_modulation.html .”

[35] S. Gatz and J. Herrmann, “Soliton propagation in materials with saturable nonlinearity,” 1991.

[36] A. Zheltikov, “Analytical insights into self-phase modulation: beyond the basic theory,” *Opt Express*, vol. 26, no. 13, p. 17571, Jun. 2018, doi: 10.1364/oe.26.017571.

[37] B. Gao *et al.*, “Generation and categories of solitons in various mode-locked fiber lasers,” *Optik (Stuttg)*, vol. 220, Oct. 2020, doi: 10.1016/j.ijleo.2020.165168.

[38] G. Millot and P. Tchofo-Dinda, “G. Millot, & P. Tchofo-Dinda. (2005). SOLITONS | Optical Fiber Solitons, Physical Origin and Properties. Elsevier EBooks, 56–65. https://doi.org/10.1016/b0-12-369395-0/01246-x.”

[39] S. Xu, A. Turnali, and M. Y. Sander, “Group-velocity-locked vector solitons and dissipative solitons in a single fiber laser with net-anomalous dispersion,” *Sci Rep*, vol. 12, no. 1, Dec. 2022, doi: 10.1038/s41598-022-10818-4.

[40] S. K. Turitsyn, B. G. Bale, and M. P. Fedoruk, “Dispersion-managed solitons in fibre systems and lasers,” Dec. 2012. doi: 10.1016/j.physrep.2012.09.004.

[41] B. Oktem, C. Ülgüdür, and F. Ö. Ilday, “Soliton-similariton fibre laser,” *Nat Photonics*, vol. 4, no. 5, pp. 307–311, May 2010, doi: 10.1038/nphoton.2010.33.

[42] “Zhang, Y., Dai, K., & Chen, D. (2023). Switchable property of dissipative soliton and dispersion-management soliton in fiber laser. Optics and Laser Technology, 158, 108790–108790. https://doi.org/10.1016/j.optlastec.2022.108790 ”.

[43] “Li, S., Zhao, X., He, Y., Wang, L., Fan, W., Gao, X., Wang, G., Zhang, W., Fu, S., Lu, C., Zhang, H., & Qu, W. (2024). Er-doped fiber lasers with all-fiber dispersion management based on Cr2Sn2Te6 saturable absorbers. Optics & Laser Technology, 175, 110729–110729. https://doi.org/10.1016/j.optlastec.2024.110729 ”.

[44] D. J. , et al. Richardson, “320fs Soliton Generation with Passively Mode-Locked Erbium Fibre Laser,” *Electronics Letters* , vol. 27, no. 9, pp. 730–732, 1991.

[45] Y. Cui, F. Lu, and X. Liu, “MoS2-clad microfibre laser delivering conventional, dispersion-managed and dissipative solitons,” *Sci Rep*, vol. 6, Jul. 2016, doi: 10.1038/srep30524.

[46] J. Peng, L. Zhan, Z. Gu, K. Qian, S. Luo, and Q. Shen, “Direct generation of 128-fs Gaussian pulses from a compensation-free fiber laser using dual mode-locking mechanisms,” *Opt Commun*, vol. 285, no. 5, pp. 731–733, Mar. 2012, doi: 10.1016/j.optcom.2011.10.082.

[47] L. E. Nelson, D. J. Jones, K. Tamura, H. A. Haus, and E. P. Ippen, “Ultrashort-pulse fiber ring lasers,” *Appl Phys B*, vol. 65, no. 2, pp. 277–294, 1997, doi: 10.1007/s003400050273.

[48] Y. Song, X. Shi, C. Wu, D. Tang, and H. Zhang, "Recent progress of study on optical solitons in fiber lasers," *Appl Phys Rev*, vol. 6, no. 2, Jun. 2019, doi: 10.1063/1.5091811.

[49] R. Paschotta, "https://www.rp-photonics.com/solitons.html."

[50] U. Keller, "Keller, U. (2010). Ultrafast solid-state laser oscillators: a success story for the last 20 years with no end in sight. Applied Physics B, 100(1), 15–28. https://doi.org/10.1007/s00340-010-4045-z".

[51] "ocw.mit.edu", Accessed: Feb. 07, 2024. [Online]. Available: https://ocw.mit.edu/courses/6-974-fundamentals-of-photonics-quantum-electronics-spring-2006/9817c9baafd71b0c65e8b62c388cafc8_q_swtch_mode_loc.pdf

[52] M. A. Ismail, S. W. Harun, H. Ahmad, and M. C. Paul, "Passive Q-switched and Mode-locked Fiber Lasers Using Carbon-based Saturable Absorbers," in *Fiber Laser*, InTech, 2016. doi: 10.5772/61703.

[53] "Han, Y., Guo, Y., Gao, B., Ma, C., Zhang, R., & Zhang, H. (2020). Generation, optimization, and application of ultrashort femtosecond pulse in mode-locked fiber lasers. Progress in Quantum Electronics, 71, 100264. https://doi.org/10.1016/j.pquantelec.2020.100264 ".

[54] "Yu, L., Tang, Z., Liang, J., Zeng, Q., Wang, J., Luo, X., Wang, J., Yan, P., Dong, F., Liu, X., Lue, Q., Guo, C., & Ruan, S. (2023). High-energy femtosecond pulse generation from a hybrid mode-locked large-mode-area Er:ZBLAN fiber laser. Optics Letters, 48(7), 1830–1830. https://doi.org/10.1364/ol.485820 ".

[55] H. A. Haus, "Haus, H. A. (2000). Mode-locking of lasers. IEEE Journal of Selected Topics in Quantum Electronics, 6(6), 1173–1185. https://doi.org/10.1109/2944.902165."

[56] "insight review articles," 2003. [Online]. Available: www.nature.com/nature

[57] "Shakaty, A. A., Hmood, J. K., & Mhdi, Bushra. R. (2021). Graphene-based Saturable Absorber for Pulsed Fiber Laser Generation. Journal of Physics: Conference Series, 1795(1), 012048. https://doi.org/10.1088/1742-6596/1795/1/012048 ".

[58] B. Zhang *et al.*, "Recent Progress in 2D Material-Based Saturable Absorbers for All Solid-State Pulsed Bulk Lasers," Feb. 01, 2020, *Wiley-VCH Verlag*. doi: 10.1002/lpor.201900240.

[59] J. Jeon, J. Lee, and J. H. Lee, "Numerical study on the minimum modulation depth of a saturable absorber for stable fiber laser mode locking," *Journal of the Optical Society of America B*, vol. 32, no. 1, pp. 31–37, 2014, doi: 10.1364/josab.32.000031.

[60] H. H. Liu and K. K. Chow, "Enhanced stability of dispersion-managed mode-locked fiber lasers with near-zero net cavity dispersion by high-contrast saturable absorbers," *Opt Lett*, vol. 39, no. 1, pp. 150–153, Jan. 2014, doi: 10.1364/ol.39.000150.

[61] C. Ma, X. Tian, B. Gao, and G. Wu, "Numerical simulations on influence of the saturable absorber in Er-doped fiber laser," *Opt Commun*, vol. 410, pp. 941–946, Mar. 2018, doi: 10.1016/j.optcom.2017.10.013.

[62] J. Lee, S. Kwon, and J. H. Lee, "Numerical investigation of the impact of the saturable absorber recovery time on the mode-locking performance of fiber lasers," *Journal of Lightwave Technology*, vol. 38, no. 15, pp. 4124–4132, Aug. 2020, doi: 10.1109/JLT.2020.2985718.

[63] L. Cheng *et al.*, "Linear and nonlinear optical properties modulation of Sb 2 Te 3 /GeTe bilayer film as a promising saturable absorber," *Results Phys*, vol. 13, Jun. 2019, doi: 10.1016/j.rinp.2019.102282.

[64] A. Martinez *et al.*, "Low-loss saturable absorbers based on tapered fibers embedded in carbon nanotube/polymer composites," *APL Photonics*, vol. 2, no. 12, pp. 126103–126103, Dec. 2017, doi: 10.1063/1.4996918.

[65]. H A Haus ; 5 *et al.*, "Stable mode-locked fiber laser based on CVD fabricated graphene saturable absorber," 19. A. H. Castro Neto, 2004.

[66] B. Nizamani *et al.*, "Mechanical exfoliation of indium tin oxide as saturable absorber for Q-switched Ytterbium-doped and Erbium-doped fiber lasers," *Opt Commun*, vol. 475, Nov. 2020, doi: 10.1016/j.optcom.2020.126217.

[67] S. Salam *et al.*, "FIrpic thin film as saturable absorber for passively Q-switched and mode-locked erbium-doped fiber laser," *Optical Fiber Technology*, vol. 50, pp. 256–262, Jul. 2019, doi: 10.1016/j.yofte.2019.04.005.

[68] B. Fu, J. Li, Z. Cao, and D. Popa, "Bound states of solitons in a harmonic graphene-mode-locked fiber laser," *Photonics Res*, vol. 7, no. 2, p. 116, Feb. 2019, doi: 10.1364/prj.7.000116.

[69] K. Y. Lau, X. Liu, and J. Qiu, "A Comparison for Saturable Absorbers: Carbon Nanotube Versus Graphene," *Adv Photonics Res*, vol. 3, no. 10, p. 2200023, Oct. 2022, doi: 10.1002/adpr.202200023.

[70] "Steinberg, D., Zapata, J. D., Nascimento, R., Rosa, H. G., Saito, M., & de, T. (2022). Mode-locked erbium-doped fiber laser based on a mechanically exfoliated ReS2 saturable absorber onto D-shaped optical fiber. Optical Materials Express, 12(4), 1657–1657. https://doi.org/10.1364/ome.447660 ".

[71] H. Ahmad, N. H. Mansor, S. A. Reduan, and R. Ramli, "Generation of mode-locked pulses based on D-shaped fiber with CdTe as a saturable absorber in the C-band region," *RSC Adv*, vol. 12, no. 14, pp. 8637–8646, Mar. 2022, doi: 10.1039/d1ra09069k.

[72] “Ahmad, H., Nur Hidayah Mansor, Siti Aiyah Reduan, & Rizal Ramli. (2022). Generation of mode-locked pulses based on D-shaped fiber with CdTe as a saturable absorber in the C-band region. RSC Advances, 12(14), 8637–8646. https://doi.org/10.1039/d1ra09069k ”.

[73] B. Nizamani *et al.*, “Mode-locked erbium-doped fiber laser via evanescent field interaction with indium tin oxide,” *Optical Fiber Technology*, vol. 55, Mar. 2020, doi: 10.1016/j.yofte.2019.102124.

[74] “Хонина, С. Н., Kazanskiy, N. L., & Muhammad Ali Butt. (2023). Optical Fibre-Based Sensors—An Assessment of Current Innovations. Biosensors, 13(9), 835–835. https://doi.org/10.3390/bios13090835 ”.

[75] M. Kowalczyk *et al.*, “Sb_2Te_3-deposited D-shaped fiber as a saturable absorber for mode-locked Yb-doped fiber lasers,” *Opt Mater Express*, vol. 6, no. 7, p. 2273, Jul. 2016, doi: 10.1364/ome.6.002273.

[76] Y. Cui, F. Lu, and X. Liu, “Nonlinear Saturable and Polarization-induced Absorption of Rhenium Disulfide,” *Sci Rep*, vol. 7, Jan. 2017, doi: 10.1038/srep40080.

[77] F. Passerini, “M2-brane superalgebra from Bagger-Lambert theory JHEP08(2008)062 M2-brane superalgebra from Bagger-Lambert theory,” 2008. [Online]. Available: http://iopscience.iop.org/1126-6708/2008/08/062

[78] G. A. Valaskovic, M. Holton, and G. H. Morrison, “Parameter control, characterization, and optimization in the fabrication of optical fiber near-field probes.”

[79] G. Rego, “Fibre optic devices produced by arc discharges,” 2010, *IOP Publishing Ltd*. doi: 10.1088/2040-8978/12/11/113002.

[80] “Ha, C. K., Nam, K. H., & Kang, M. S. (2021). Efficient harmonic generation in an adiabatic multimode submicron tapered optical fiber. Communications Physics, 4(1). https://doi.org/10.1038/s42005-021-00677-2 ”.

[81] T. Anbalagan, H. Haroon, H. A. Zain, H. Rafis, and S. W. Harun, “Recent Progress of Tapered Optical Fiber for Biosensing Applications,” *Journal of Engineering Science and Technology Review*, vol. 15, no. 5, pp. 204–209, 2022, doi: 10.25103/jestr.155.25.

[82] B. Renganathan, D. Sastikumar, G. Gobi, N. Rajeswari Yogamalar, and A. Chandra Bose, “Nanocrystalline ZnO coated fiber optic sensor for ammonia gas detection,” *Opt Laser Technol*, vol. 43, no. 8, pp. 1398–1404, Nov. 2011, doi: 10.1016/j.optlastec.2011.04.008.

[83] L. Zhang, Y. Tang, and L. Tong, “Micro-/Nanofiber Optics: Merging Photonics and Material Science on Nanoscale for Advanced Sensing Technology,” 2013, doi: 10.1016/j.isci.

[84] Z. Kang *et al.*, "Microfiber coated with gold nanorods as saturable absorbers for 2 μm femtosecond fiber lasers," *Opt Mater Express*, vol. 8, no. 12, pp. 3841–3850, 2018, doi: 10.1364/ome.8.003841.

[85] Z. Hu *et al.*, "NbS2-nanosheet-based saturable absorber for 1.5 μm and 2 μm ultrafast fiber lasers," *Photonics Nanostruct*, vol. 54, May 2023, doi: 10.1016/j.photonics.2023.101117.

[86] S. Chen *et al.*, "Femtosecond Pulsed Fiber Laser by an Optical Device Based on NaOH-LPE Prepared WSe2 Saturable Absorber," *Nanomaterials*, vol. 12, no. 16, Aug. 2022, doi: 10.3390/nano12162747.

[87] X. Liu *et al.*, "Reverse saturable absorption in Ti3C2 MXene nanosheets for dissipative soliton resonance mode-locking operation in Er-doped fiber laser," *Opt Mater (Amst)*, vol. 136, Feb. 2023, doi: 10.1016/j.optmat.2023.113463.

[88] Z. He *et al.*, "Two-dimensional gold decorated indium selenide for near-infrared and mid-infrared ultrafast photonics," *Opt Laser Technol*, vol. 150, no. July 2021, p. 107920, 2022, doi: 10.1016/j.optlastec.2022.107920.

[89] C. Liu *et al.*, "Near-infrared all-fiber mode-locked laser based on vanadium carbide nanosheets," *Optik (Stuttg)*, vol. 260, no. March, p. 168792, 2022, doi: 10.1016/j.ijleo.2022.168792.

[90] Z. B. Liu *et al.*, "Broadband all-optical modulation using a graphene-covered-microfiber," *Laser Phys Lett*, vol. 10, no. 6, Jun. 2013, doi: 10.1088/1612-2011/10/6/065901.

[91] A. Murad *et al.*, "Generation of noise-like pulse using nickel-based metal-organic framework saturable absorber," *Optik (Stuttg)*, vol. 290, p. 171275, Oct. 2023, doi: 10.1016/j.ijleo.2023.171275.

[92] N. Mohd Yusoff, M. H. Mohamed Ahmed, E. K. Ng, M. T. Alresheedi, M. Z. H. Mayzan, and M. A. Mahdi, "Noise-like pulse generation in 1.95 μm region using bulk α-alumina saturable absorber," *Results Phys*, vol. 52, Sep. 2023, doi: 10.1016/j.rinp.2023.106843.

[93] X. Jiang *et al.*, "Generation of dissipative soliton in erbium-doped fiber laser passively mode locked by InSb saturable absorber," *Optik (Stuttg)*, vol. 289, Oct. 2023, doi: 10.1016/j.ijleo.2023.171269.

[94] P. Guo *et al.*, "Nonlinear photonics device based on double perovskite oxide Ba2LaTaO6 for ultrafast laser generation," *Opt Laser Technol*, vol. 155, Nov. 2022, doi: 10.1016/j.optlastec.2022.108334.

[95] S. Ko, J. Lee, J. Koo, B. S. Joo, M. Gu, and J. H. Lee, "Chemical wet etching of an optical fiber using a hydrogen fluoride-free solution for a saturable absorber based on the evanescent field interaction," *Journal of Lightwave Technology*, vol. 34, no. 16, pp. 3776–3784, Aug. 2016, doi: 10.1109/JLT.2016.2583061.

[96] N. D. Jaji, H. L. Lee, M. H. Hussin, H. M. Akil, M. R. Zakaria, and M. B. H. Othman, "Advanced nickel nanoparticles technology: From synthesis to applications," *Nanotechnol Rev*, vol. 9, no. 1, pp. 1456–1480, 2020, doi: 10.1515/ntrev-2020-0109.

[97] Sani Garba Danjumma, "Nickel Oxide (NiO) Devices and Applications: A Review," *International Journal of Engineering Research and*, vol. V8, no. 04, 2019, doi: 10.17577/ijertv8is040281.

[98] F. Wang, J. Hu, Y. Peng, X. Wu, H. Xue, and H. Pang, "Application and modification of nickel-based metal-organic frameworks in electrochemical sensing," *Advanced Sensor and Energy Materials*, vol. 2, no. 2, p. 100053, Jun. 2023, doi: 10.1016/j.asems.2023.100053.

[99] C. Dou *et al.*, " Ternary ReS 2(1-x) Se 2x alloy saturable absorber for passively Q-switched and mode-locked erbium-doped all-fiber lasers ," *Photonics Res*, vol. 7, no. 3, p. 283, 2019, doi: 10.1364/prj.7.000283.

[100] G. Genchi, A. Carocci, G. Lauria, M. S. Sinicropi, and A. Catalano, "Nickel: Human health and environmental toxicology," Feb. 01, 2020, *MDPI AG*. doi: 10.3390/ijerph17030679.

[101] N. M. Fe, N. Fe, M. S. Mk, and D. Djuhana, "Investigation to Localized Surface Plasmon Resonance Properties of," vol. 855, pp. 243–247, 2020, doi: 10.4028/www.scientific.net/KEM.855.243.

[102] G. S. Pawar, A. Elikkottil, B. Pesala, A. A. Tahir, and T. K. Mallick, "Plasmonic nickel nanoparticles decorated on to LaFeO 3 photocathode for enhanced solar hydrogen generation," *Int J Hydrogen Energy*, vol. 44, no. 2, pp. 578–586, Jan. 2019, doi: 10.1016/j.ijhydene.2018.10.240.

[103] L. Karam, J. Reboul, N. El Hassan, J. Nelayah, and P. Massiani, "Nanostructured nickel aluminate as a key intermediate for the production of highly dispersed and stable nickel nanoparticles supported within mesoporous alumina for dry reforming of methane," *Molecules*, vol. 24, no. 22, Nov. 2019, doi: 10.3390/molecules24224107.

[104] J. T. S. Cahill, D. T. Blewett, N. V. Nguyen, A. Boosalis, S. J. Lawrence, and B. W. Denevi, "Optical constants of iron and nickel metal and an assessment of their relative influences on silicate mixture spectra from the FUV to the NIR," *Icarus*, vol. 317, pp. 229–241, Jan. 2019, doi: 10.1016/j.icarus.2018.07.008.

[105] "Ablated nickel nanoparticles: third harmonic generation and optical nonlinearities".

[106] "Strong Third-order Optical Nonlinearities of the Ag, Ni, Ti, and Co Nanoparticles Synthesized During Laser Ablation of Bulk Metals in Liquids".

[107] J. Chen *et al.*, "Plasmonic nickel nanoantennas," *Small*, vol. 7, no. 16, pp. 2341–2347, Aug. 2011, doi: 10.1002/smll.201100640.

[108] E. T. Kho, S. Jantarang, Z. Zheng, J. Scott, and R. Amal, "Harnessing the Beneficial Attributes of Ceria and Titania in a Mixed-Oxide Support for Nickel-Catalyzed Photothermal CO2 Methanation," *Engineering*, vol. 3, no. 3, pp. 393–401, Jun. 2017, doi: 10.1016/J.ENG.2017.03.016.

[109] "Third-order non-linear optical switching and threshold limiting of NiO thin films".

[110] "Nonlinear refraction in NiO thin films".

[111] J. R. Manders *et al.*, "Solution-Processed Nickel Oxide Hole Transport Layers in High Efficiency Polymer Photovoltaic Cells," *Adv Funct Mater*, vol. 23, pp. 2993–3001, 2013, doi: 10.1002/adfm.201202269.

[112] B. Wang *et al.*, "Novel self-assembled porous yolk-shell NiO nanospheres with excellent electrochromic performance for smart windows," *Particuology*, vol. 84, pp. 72–80, Jan. 2024, doi: 10.1016/j.partic.2023.03.007.

[113] T. P. Mokoena, H. C. Swart, and D. E. Motaung, "A review on recent progress of p-type nickel oxide based gas sensors: Future perspectives," *J Alloys Compd*, vol. 805, pp. 267–294, Oct. 2019, doi: 10.1016/j.jallcom.2019.06.329.

[114] K. O. Egbo, C. P. Liu, C. E. Ekuma, and K. M. Yu, "Vacancy defects induced changes in the electronic and optical properties of NiO studied by spectroscopic ellipsometry and first-principles calculations," *J Appl Phys*, vol. 128, no. 13, Oct. 2020, doi: 10.1063/5.0021650.

[115] M. Bonomo, D. Dini, and F. Decker, "Electrochemical and photoelectrochemical properties of nickel oxide (NiO) with nanostructured morphology for photoconversion applications," 2018, *Frontiers Media S.A.* doi: 10.3389/fchem.2018.00601.

[116] M. Ma *et al.*, "Ternary chalcogenide Ta2NiS5nanosheets for broadband pulse generation in ultrafast fiber lasers," *Nanophotonics*, vol. 9, no. 8, pp. 2341–2349, 2020, doi: 10.1515/nanoph-2019-0350.

[117] J. Wang *et al.*, "NiPS3 nanosheets for passive pulse generation in an Er-doped fiber laser," *J Mater Chem C Mater*, vol. 7, no. 46, pp. 14625–14631, 2019, doi: 10.1039/c9tc04722k.

[118] G. Sobon, A. Duzynska, M. Świniarski, J. Judek, and J. Sotor, "CNT-based saturable absorbers with scalable modulation depth for Thulium-doped fiber lasers operating at 1 . 9 μ m," no. October 2016, pp. 1–9, 2017, doi: 10.1038/srep45491.

[119] P. Wang *et al.*, "NiS2 as a broadband saturable absorber for ultrafast pulse lasers," *Opt Laser Technol*, vol. 132, pp. 106492–106492, Dec. 2020, doi: 10.1016/j.optlastec.2020.106492.

[120] J. He, H. Lu, L. Tao, Y. Zhao, Z. Zheng, and B. Zhou, "Novel two-dimensional semi-metallic NiTe2 based saturable absorber for ultrafast mode-locked fiber laser," *Infrared Phys Technol*, vol. 123, pp. 104195–104195, Jun. 2022, doi: 10.1016/j.infrared.2022.104195.

[121] A. Murad, N. Mohd Yusoff, J. Y. C. Liew, M. H. Yaacob, C. S. Goh, and M. A. Mahdi, "Nickel 1,3,5-benzene-tricarboxylic acid-metal organic framework polymer composite saturable absorber for femtosecond pulse generation," *Results Phys*, vol. 41, pp. 105881–105881, Oct. 2022, doi: 10.1016/j.rinp.2022.105881.

[122] Y. Zhang *et al.*, "MOF-derived porous NiO-Co3O4 for high performance ultrafast pulse generation," *Opt Laser Technol*, vol. 155, pp. 108358–108358, Nov. 2022, doi: 10.1016/j.optlastec.2022.108358.

[123] K. Y. Lau, J. C. Zheng, C. Jin, and S. Yang, "Mono-elemental saturable absorber in near-infrared mode-locked fiber laser: A review," May 01, 2022, *Elsevier B.V.* doi: 10.1016/j.infrared.2022.104103.

[124] C. Huda, S. W. Harun, A. A. A. Jafry, N. Kasim, A. H. Zaidan, and M. Yasin, "NICKEL DISULFIDE SATURABLE ABSORBER AS Q-SWITCHER IN ERBIUM-DOPED FIBER LASER CAVITY," *Chalcogenide Letters*, vol. 18, no. 3, pp. 149–154, 2021, doi: 10.15251/CL.2021.183.149.

[125] F. Taghizadeh, "The Study of Structural and Magnetic Properties of NiO Nanoparticles," *Optics and Photonics Journal*, vol. 06, no. 08, pp. 164–169, 2016, doi: 10.4236/opj.2016.68b027.

[126] C. Jayaseelan *et al.*, "Effect of sub-acute exposure to nickel nanoparticles on oxidative stress and histopathological changes in Mozambique tilapia, Oreochromis mossambicus," *Ecotoxicol Environ Saf*, vol. 107, pp. 220–228, 2014, doi: 10.1016/j.ecoenv.2014.06.012.

[127] B. Borah, G. Rajitha, and R. K. Dash, "Correlation between the thickness and properties of the ethanol treated GO–PDMS based composite materials," *Journal of Materials Science: Materials in Electronics*, vol. 29, no. 23, pp. 20216–20224, Dec. 2018, doi: 10.1007/s10854-018-0154-2.

[128] M. M. Rahman, S. H. Im, and J. J. Lee, "Enhanced photoresponse in dye-sensitized solar cells via localized surface plasmon resonance through highly stable nickel nanoparticles," *Nanoscale*, vol. 8, no. 11, pp. 5884–5891, 2016, doi: 10.1039/c5nr08155f.

[129] M. Mansor *et al.*, "Cerium oxide/polydimethylsiloxane composite tapered fiber saturable absorber for mode-locked pulsed erbium-doped fiber laser," *Infrared Phys Technol*, vol. 125, no. January, pp. 1–10, 2022, doi: 10.1016/j.infrared.2022.104220.

[130] S. Ravets, J. E. Hoffman, P. R. Kordell, J. D. Wong-Campos, S. L. Rolston, and L. A. Orozco, "Intermodal energy transfer in a tapered optical fiber: optimizing transmission," *Journal of the Optical Society of America A*, vol. 30, no. 11, p. 2361, Nov. 2013, doi: 10.1364/josaa.30.002361.

[131] R. Nagai and T. Aoki, "Ultra-low-loss tapered optical fibers with minimal lengths," *Opt Express*, vol. 22, no. 23, pp. 28427–28436, 2014, doi: 10.1364/oe.22.028427.

[132] N. M. Yusoff, M. A. W. Abdul Hadi, N. H. Zainol Abidin, M. T. Alresheedi, C. S. Goh, and M. A. Mahdi, "Aluminum oxide/polydimethylsiloxane-based Q-switched mode-locked erbium-doped fiber laser," *Optik (Stuttg)*, vol. 257, no. January, p. 168730, 2022, doi: 10.1016/j.ijleo.2022.168730.

[133] M. H. M. Ahmed *et al.*, "Ultrashort pulse thulium-doped fiber laser with molybdenum trioxide on tapered fiber," *Optik (Stuttg)*, vol. 257, no. February, pp. 1–11, 2022, doi: 10.1016/j.ijleo.2022.168736.

[134] I. D. Jung *et al.*, "Semiconductor saturable absorber mirrors supporting sub-10-fs pulses," *Appl Phys B*, vol. 65, no. 2, pp. 137–150, 1997, doi: 10.1007/s003400050259.

[135] K. Y. Lau *et al.*, "High Energy L-band Femtosecond Fiber Laser with Carbon Nanotube Saturable Absorber," *2018 IEEE 7th International Conference on Photonics, ICP 2018*, pp. 18–20, 2018, doi: 10.1109/ICP.2018.8533194.

[136] C. Huang, C. Wang, W. Shang, N. Yang, Y. Tang, and J. Xu, "Developing high energy dissipative soliton fiber lasers at 2 micron," *Sci Rep*, vol. 5, Sep. 2015, doi: 10.1038/srep13680.

[137] L. E. Nelson, D. J. Jones, K. Tamura, H. A. Haus, and E. P. Ippen, "Ultrashort-pulse fiber ring lasers," 1997.

[138] S. Tao, L. Xu, G. Chen, C. Gu, and H. Song, "Ultra-High Repetition Rate Harmonic Mode-Locking Generated in a Dispersion and Nonlinearity Managed Fiber Laser," *Journal of Lightwave Technology*, vol. 34, no. 9, pp. 2354–2357, May 2016, doi: 10.1109/JLT.2016.2528304.

[139] Q. Huang, C. Zou, T. Wang, M. Al Araimi, A. Rozhin, and C. Mou, "Influence of Average Cavity Dispersion and Spectral Bandwidth on Passively Harmonic Mode Locked L-Band Er-Doped Fiber Laser," *IEEE Journal of Selected Topics in Quantum Electronics*, vol. 25, no. 4, Jul. 2019, doi: 10.1109/JSTQE.2019.2924869.

[140] Y. Ge *et al.*, "Revision on fiber dispersion measurement based on Kelly sideband measurement," *Microw Opt Technol Lett*, vol. 58, no. 1, pp. 242–245, Jan. 2016, doi: 10.1002/mop.29532.

[141] C. Wang *et al.*, "High energy and low noise soliton fiber laser comb based on nonlinear merging of Kelly sidebands," *Opt Express*, vol. 30, no. 13, p. 23556, Jun. 2022, doi: 10.1364/oe.460609.

[142] Y. Chen *et al.*, "The formation of various multi-soliton patterns and noise-like pulse in a fiber laser passively mode-locked by a topological insulator based saturable absorber," *Laser Phys Lett*, vol. 11, no. 5, May 2014, doi: 10.1088/1612-2011/11/5/055101.

[143] W. H. Renninger, A. Chong, and F. W. Wise, "Pulse Shaping and Evolution in Normal-Dispersion Mode-Locked Fiber Lasers," 2011. [Online]. Available: http://ieeexplore.ieee.org.

[144] N. Z. A. Naharuddin *et al.*, "Pulsed-laser-ablated gold-nanoparticles saturable absorber for mode-locked erbium-doped fiber lasers," *Opt Laser Technol*, vol. 150, no. February, p. 107875, 2022, doi: 10.1016/j.optlastec.2022.107875.

[145] N. Li *et al.*, "Cavity-length optimization for high energy pulse generation in a long cavity passively mode-locked all-fiber ring laser," *Appl Opt*, vol. 51, no. 17, pp. 3726–3730, 2012, doi: 10.1364/AO.51.003726.

[146] S. Tang *et al.*, "High-Energy Mode-Locked Pulse Er-Doped Fiber Laser-Based GeTe as Saturable Absorber," *Nanomaterials*, vol. 13, no. 16, Aug. 2023, doi: 10.3390/nano13162331.

[147] D. Li *et al.*, "Wavelength and pulse duration tunable ultrafast fiber laser mode-locked with carbon nanotubes," *Sci Rep*, vol. 8, no. 1, Dec. 2018, doi: 10.1038/s41598-018-21108-3.

[148] A. Dutta, "Ultra Short Pico Second Chirped Pulse Generation using SESAM based Mode-Locked Fiber Laser," 2015.

[149] D. Li *et al.*, "Wavelength and pulse duration tunable ultrafast fiber laser mode-locked with carbon nanotubes," *Sci Rep*, vol. 8, no. 1, Dec. 2018, doi: 10.1038/s41598-018-21108-3.

[150] T. Zhu, Z. Wang, D. N. Wang, F. Yang, and L. Li, "Generation of wavelength-tunable and coherent dual-wavelength solitons in the C + L band by controlling the intracavity loss," *Photonics Res*, vol. 7, no. 8, p. 853, Aug. 2019, doi: 10.1364/prj.7.000853.

[151] M. Hashem *et al.*, "Fabrication and characterization of semiconductor nickel oxide (NiO) nanoparticles manufactured using a facile thermal treatment," *Results Phys*, vol. 6, pp. 1024–1030, 2016, doi: 10.1016/j.rinp.2016.11.031.

[152] N. M. Hosny, "Synthesis, characterization and optical band gap of NiO nanoparticles derived from anthranilic acid precursors via a thermal decomposition route," *Polyhedron*, vol. 30, no. 3, pp. 470–476, Feb. 2011, doi: 10.1016/j.poly.2010.11.020.

[153] A. A. Abul-Magd, H. Y. Morshidy, and A. M. Abdel-Ghany, "The role of NiO on the structural and optical properties of sodium zinc borate glasses," *Opt Mater (Amst)*, vol. 109, Nov. 2020, doi: 10.1016/j.optmat.2020.110301.

[154] Muhammad Arif Malik., "5.4: Concentration of solutions." Accessed: Jul. 15, 2024. [Online]. Available: https://chem.libretexts.org/Bookshelves/Introductory_Chemistry/Introduction_to_General_Chemistry_(Malik)/05%3A_Solutions/5.04%3A_Concentration_of_solutions

[155] H. Rezvantalab and S. Shojaei-Zadeh, "Particle adsorption at polydimethylsiloxane (PDMS)/water interfaces in the presence of a cross-linking reaction," *J Colloid Interface Sci*, vol. 400, pp. 70–77, Jun. 2013, doi: 10.1016/j.jcis.2013.02.048.

[156] Y. W. Song and S. Yamashita, "A tester for carbon nanotube mode lockers," *Japanese Journal of Applied Physics, Part 1: Regular Papers and Short Notes and Review Papers*, vol. 46, no. 5 A, pp. 3111–3113, May 2007, doi: 10.1143/JJAP.46.3111.

[157] E. K. Ng *et al.*, "Saturable absorber incorporating graphene oxide polymer composite through dip coating for mode-locked fiber laser," *Opt Mater (Amst)*, vol. 100, pp. 109619–19619, 2020, doi: 10.1016/j.optmat.2019.109619.

[158] Y. Jiang *et al.*, "Local nonlinearity engineering of evanescent-field-interaction fiber devices embedding in black phosphorus quantum dots," *Nanophotonics*, vol. 11, no. 1, pp. 87–100, Jan. 2022, doi: 10.1515/nanoph-2021-0513.

[159] J. Peng, R. Zhu, T. Shen, Y. Liu, Y. Ma, and F. Gu, "2D Saturable Absorbers for Potential Pulse Generation in the Visible-Wavelength Band," *Photonics*, vol. 10, no. 5, May 2023, doi: 10.3390/photonics10050543.

[160] B. Guo *et al.*, "Sub-200 fs soliton mode-locked fiber laser based on bismuthene saturable absorber," *Opt Express*, vol. 26, no. 18, pp. 22750–22760, 2018, doi: 10.1364/oe.26.022750.

[161] J. Sotor *et al.*, "All-fiber Ho-doped mode-locked oscillator based on a graphene saturable absorber," *Opt Lett*, vol. 41, no. 11, p. 2592, Jun. 2016, doi: 10.1364/ol.41.002592.

[162] Y. Meng, M. Salhi, A. Niang, K. Guesmi, G. Semaan, and F. Sanchez, "Mode-locked Er:Yb-doped double-clad fiber laser with 75-nm tuning range," *Opt Lett*, vol. 40, no. 7, p. 1153, Apr. 2015, doi: 10.1364/ol.40.001153.

[163] D. Y. Tang, P. D. Drummond, W. S. Man, and H. Y. Tam, "Observation of modulation instability in a fiber soliton ring laser," 1999. [Online]. Available: www.elsevier.comrlocateroptcom

[164] Z. Wen, K. Wang, H. Chen, B. Lu, and J. Bai, "Stable-, period-N- and multiple-soliton regimes in a mode-locked fiber laser with inconsistently filtered central wavelengths," *Opt Express*, vol. 28, no. 19, p. 28033, 2020, doi: 10.1364/oe.400981.

[165] J. Sotor *et al.*, "All-fiber Ho-doped mode-locked oscillator based on a graphene saturable absorber," *Opt Lett*, vol. 41, no. 11, p. 2592, Jun. 2016, doi: 10.1364/ol.41.002592.

[166] X.-D. Wang *et al.*, "Nanocomposites with gold nanorod/silica core-shell structure as saturable absorber for femtosecond pulse generation in a fiber laser," *Opt Express*, vol. 23, no. 17, p. 22602, Aug. 2015, doi: 10.1364/oe.23.022602.

[167] A. Martinez, K. Fuse, B. Xu, and S. Yamashita, "Optical deposition of graphene and carbon nanotubes in a fiber ferrule for passive mode-locked lasing," Technical Digest Optical Society of America, 2009.

[168] D. Churin, K. Kieu, and N. Peyghambarian, "The Role of the Saturable Absorber in a Mode-Locked Fiber Laser," *Optics InfoBase Conference Papers*, vol. 8237, pp. 1–6, 2012, doi: 10.1117/12.909499.

[169] J. Peng and S. Boscolo, "Filter-Based Dispersion-Managed Versatile Ultrafast Fibre Laser," *Sci Rep*, vol. 6, May 2016, doi: 10.1038/srep25995.

[170] Q. Sun *et al.*, "Experiment and simulations on the energy reservoir effect in femtosecond light filaments," 2005.

[171] Y. Feng *et al.*, "Saturable absorption behavior of free-standing graphene polymer composite films over broad wavelength and time ranges," *Opt Express*, vol. 23, no. 1, p. 559, Jan. 2015, doi: 10.1364/oe.23.000559.

[172] S. Salam, A. H. H. Al-Masoodi, M. Yasin, and S. W. Harun, "Soliton mode-locked Er-doped fiber laser by using Alq3 saturable absorber," *Opt Laser Technol*, vol. 123, Mar. 2020, doi: 10.1016/j.optlastec.2019.105893.

[173] J.-C. Chiu *et al.*, "Concentration effect of carbon nanotube based saturable absorber on stabilizing and shortening mode-locked pulse," Marcel Dekker, 2003.

APPENDICES

Appendix A

OSA Spectrum over SMF at Maximum Pump Power

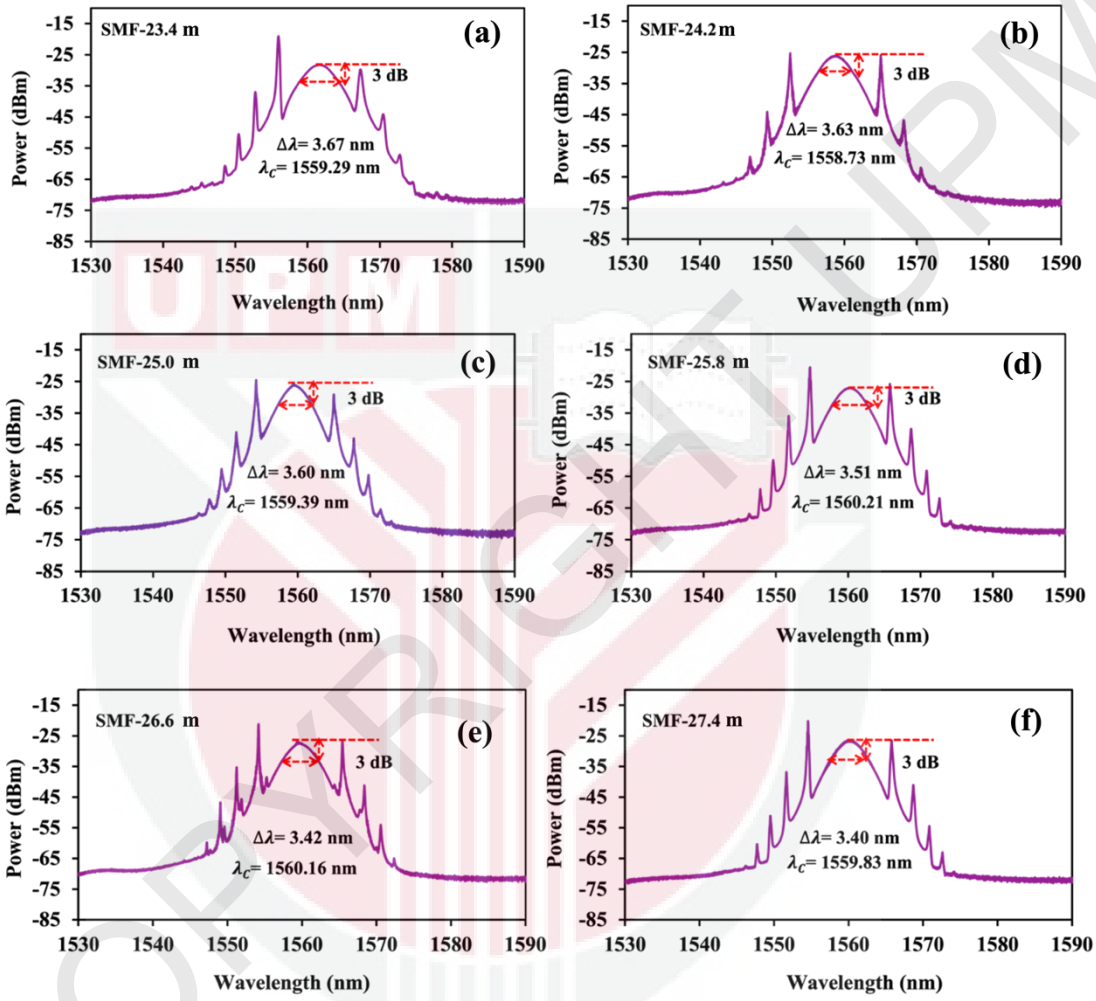

Figure A1 : OSA Spectrum Highlighted the 3 dB Spectral Measurements for (a) SMF-23.4 m, (b) SMF-24.2 m (c) SMF-25.0 m, (d) SMF-25.8 m, (e) SMF-26.6 m (f) SMF-27.4 m

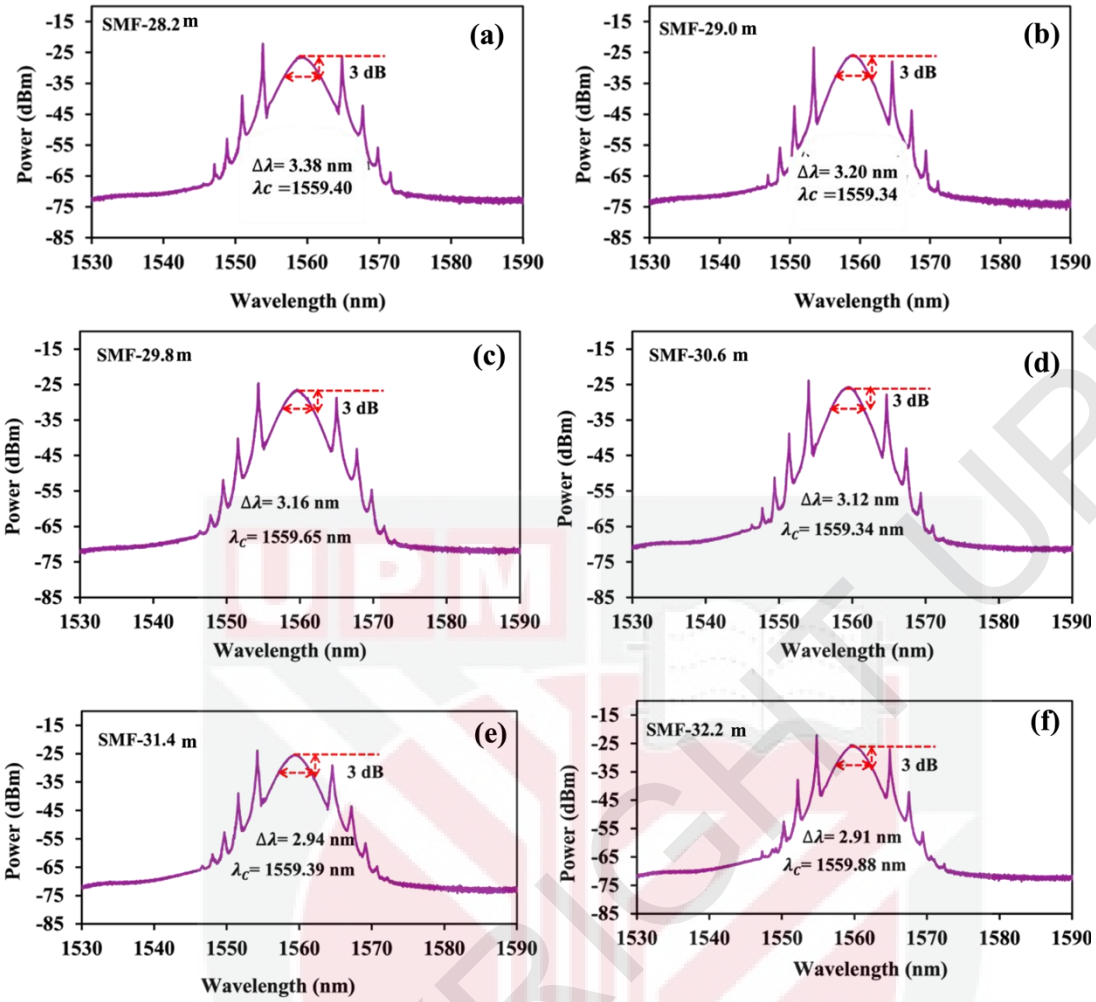

Figure A2 : OSA Spectrum Highlighted the 3 dB Spectral Measurements for (a) SMF-28.2 m, (b) SMF-29.0 m (c) SMF-29.8 m, (d) SMF-30.6 m, (e) SMF-31.4 m (f) SMF-32.2 m

Appendix B

Multiple Pulse Oberserved from Oscilloscope, Per Measurement, AC and OSA Stability for SMF-21.8 m

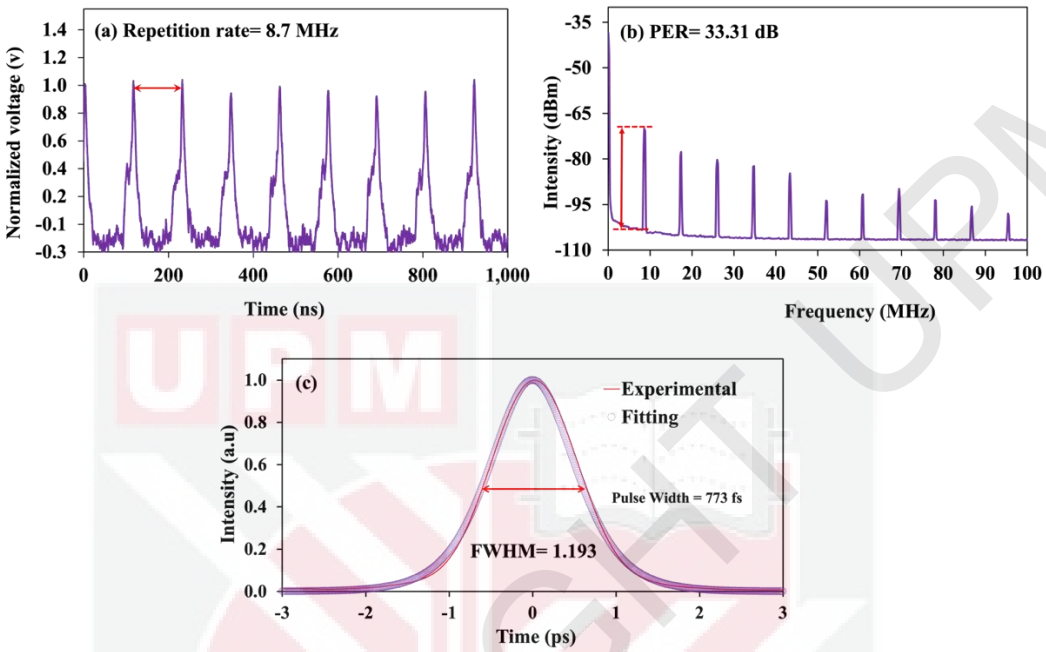

Figure B1 : (a) Oscilloscope Trace for SMF-21.8 m (b) PER Measurement (c) AC Trace for SMF-21.8 m

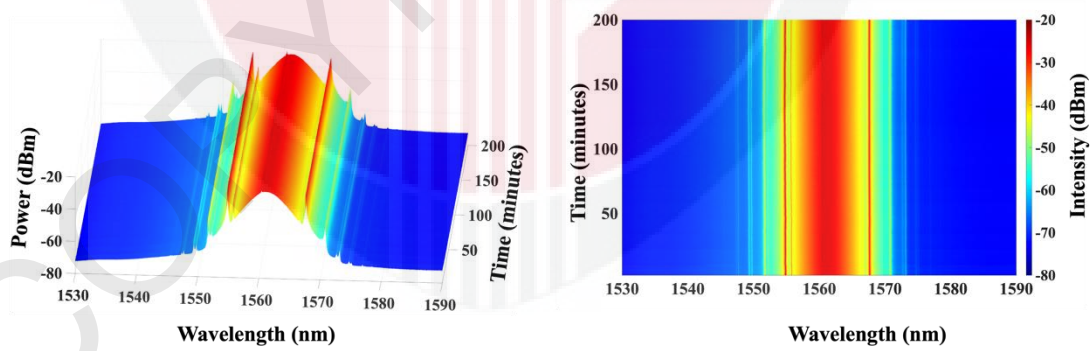

Figure B2 : 3-D Spectrogram for OSA Stability for SMF-21.8m within 200 Minutes

Appendix C

Osciloscope Trace for Different SMF Length

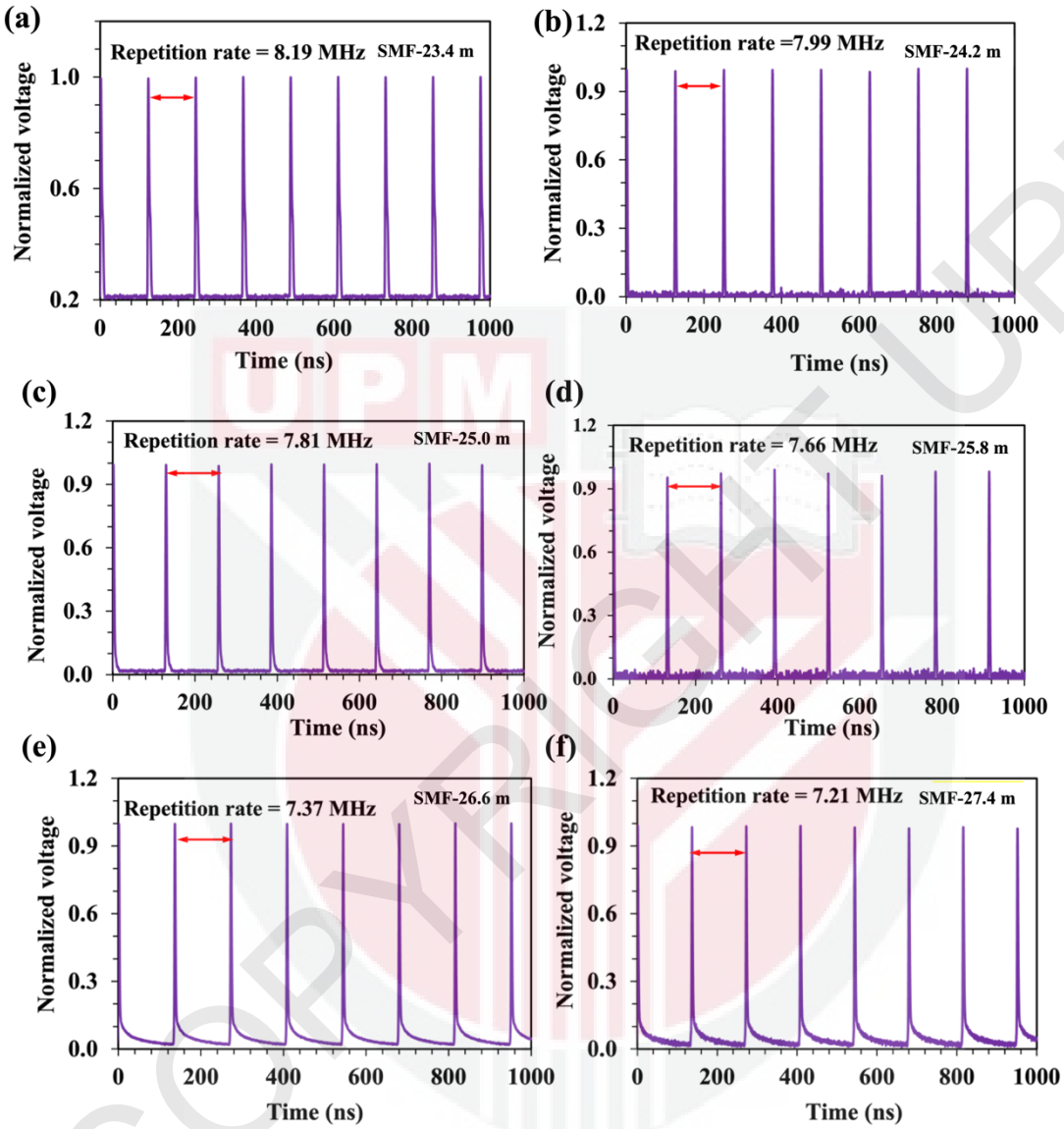

Figure C1 : Oscilloscope Trace in Time Domain Measurement for (a) SMF-23.4 m, (b) SMF-24.2 m (c) SMF-25.0 m, (d) SMF-25.8 m, (e) SMF-26.6 m (f) SMF-27.4 m

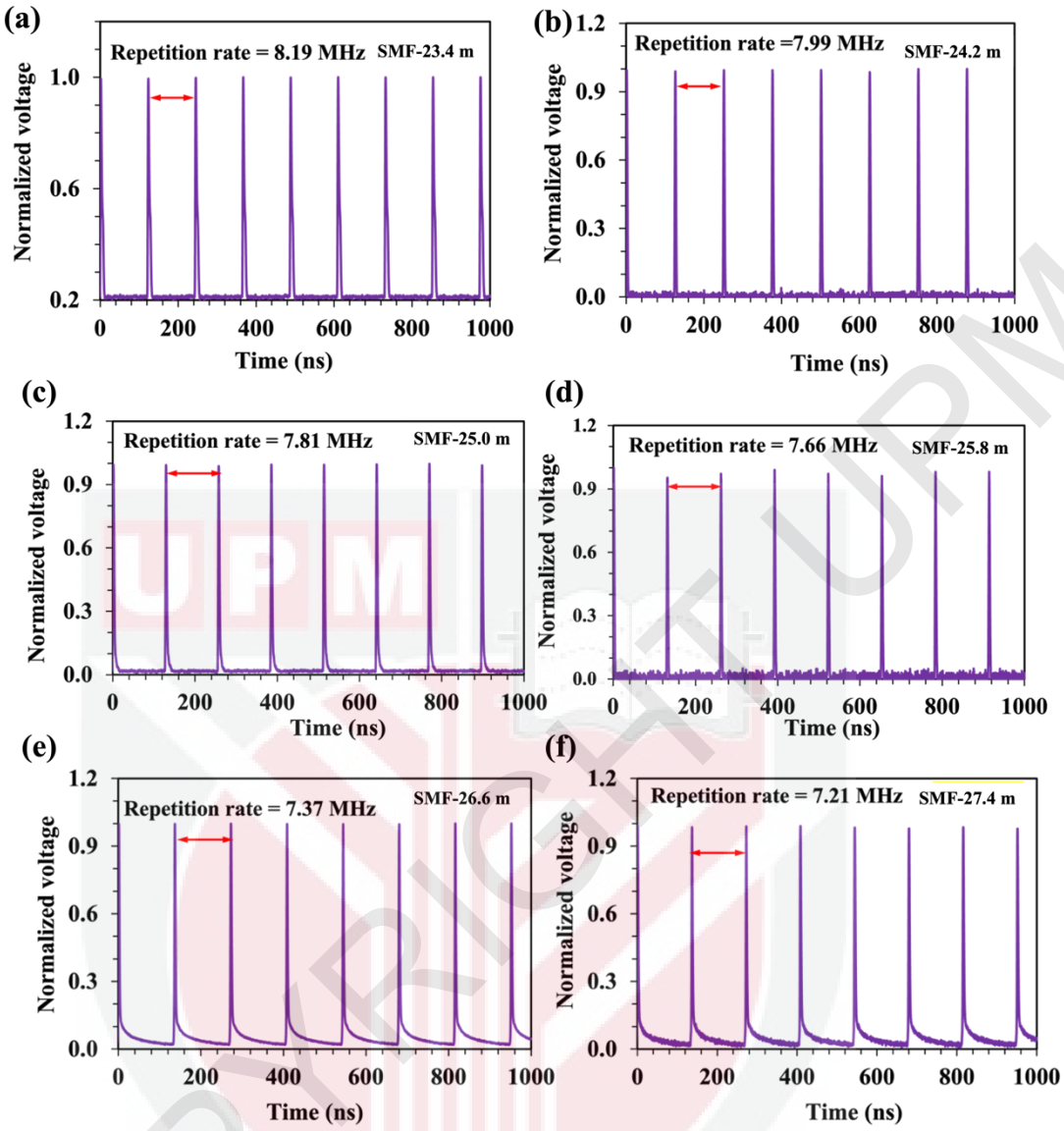

Figure C2 : Oscilloscope Trace in Time Domain Measurement for (a) SMF-28.2 m, (b) SMF-29.0 m (c) SMF-29.8 m, (d) SMF-30.6 m, (e) SMF-31.4 m (f) SMF-32.2 m

Appendix D

Autocorrelator Trace for Different SMF Length

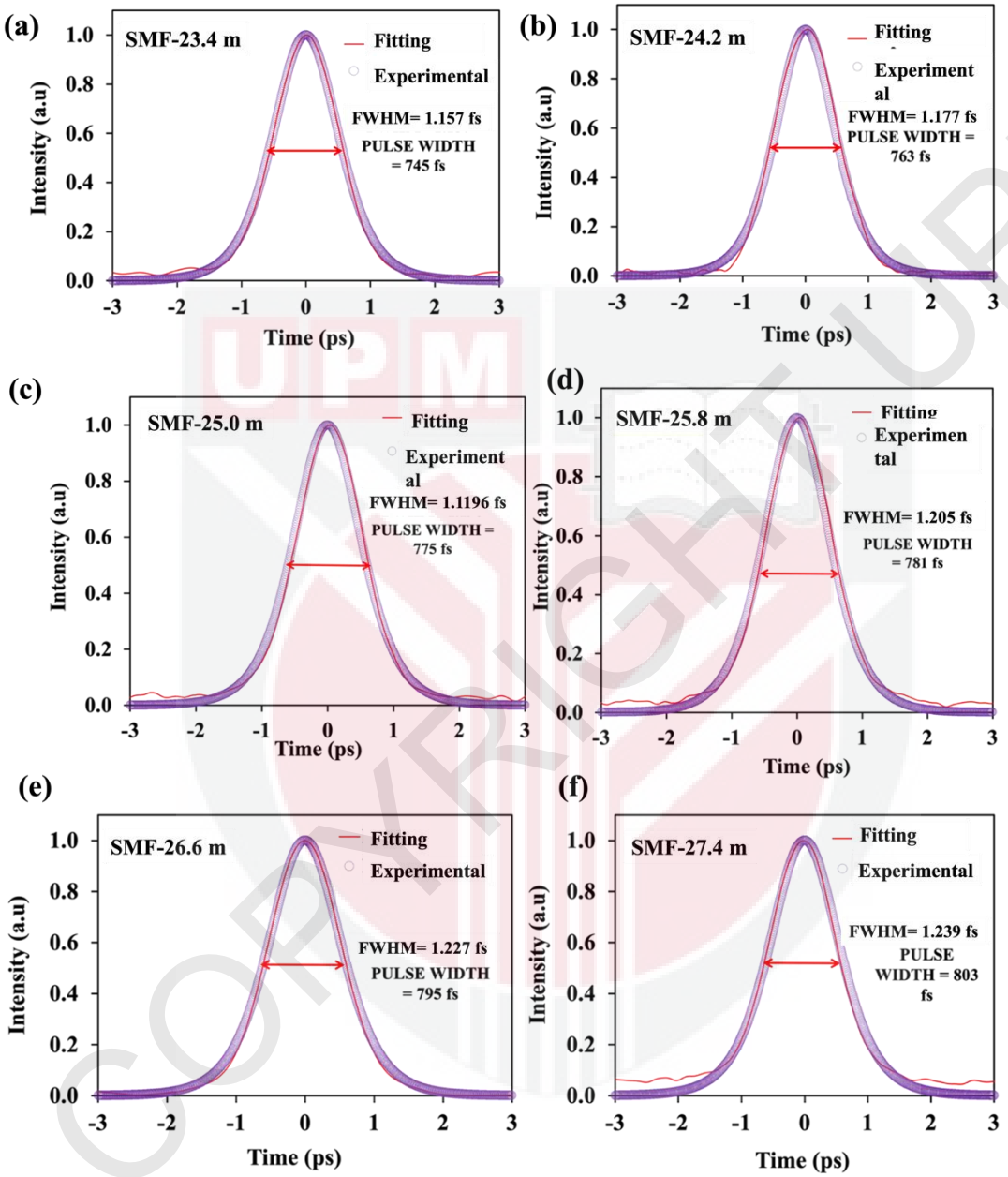

Figure D1 : AC Trace Measurement for (a) SMF-23.4 m, (b) SMF-24.2 m (c) SMF-25.0 m, (d) SMF-25.8 m, (e) SMF-26.6 m (f) SMF-27.4 m

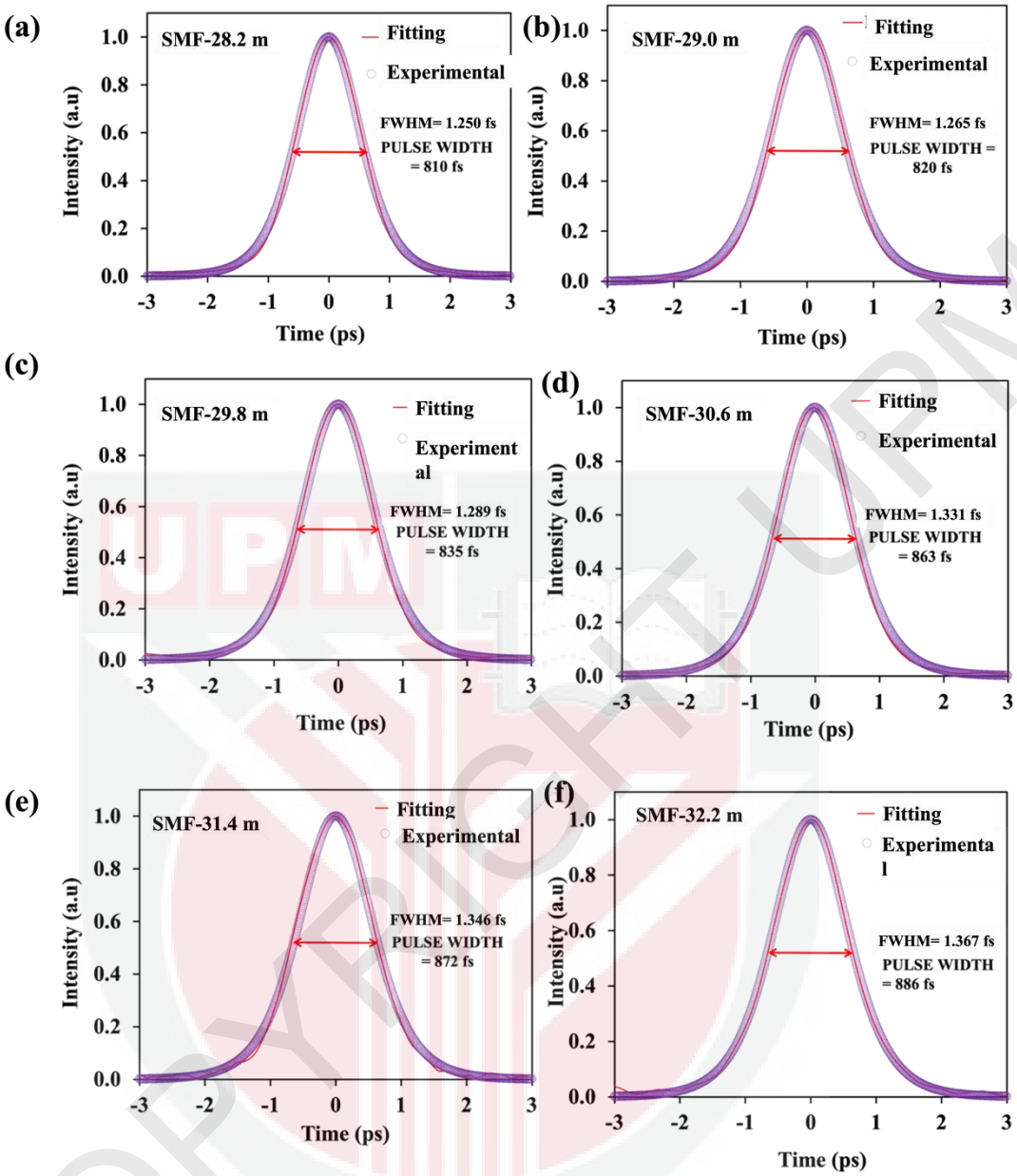

Figure D2 : AC Trace Measurement for (a) SMF-28.2 m, (b) SMF-29.0 m (c) SMF-29.8 m, (d) SMF-30.6 m, (e) SMF-31.4 m (f) SMF-32.2 m

Appendix E

RF Spectrum-PER Measurements for Different SMF Length

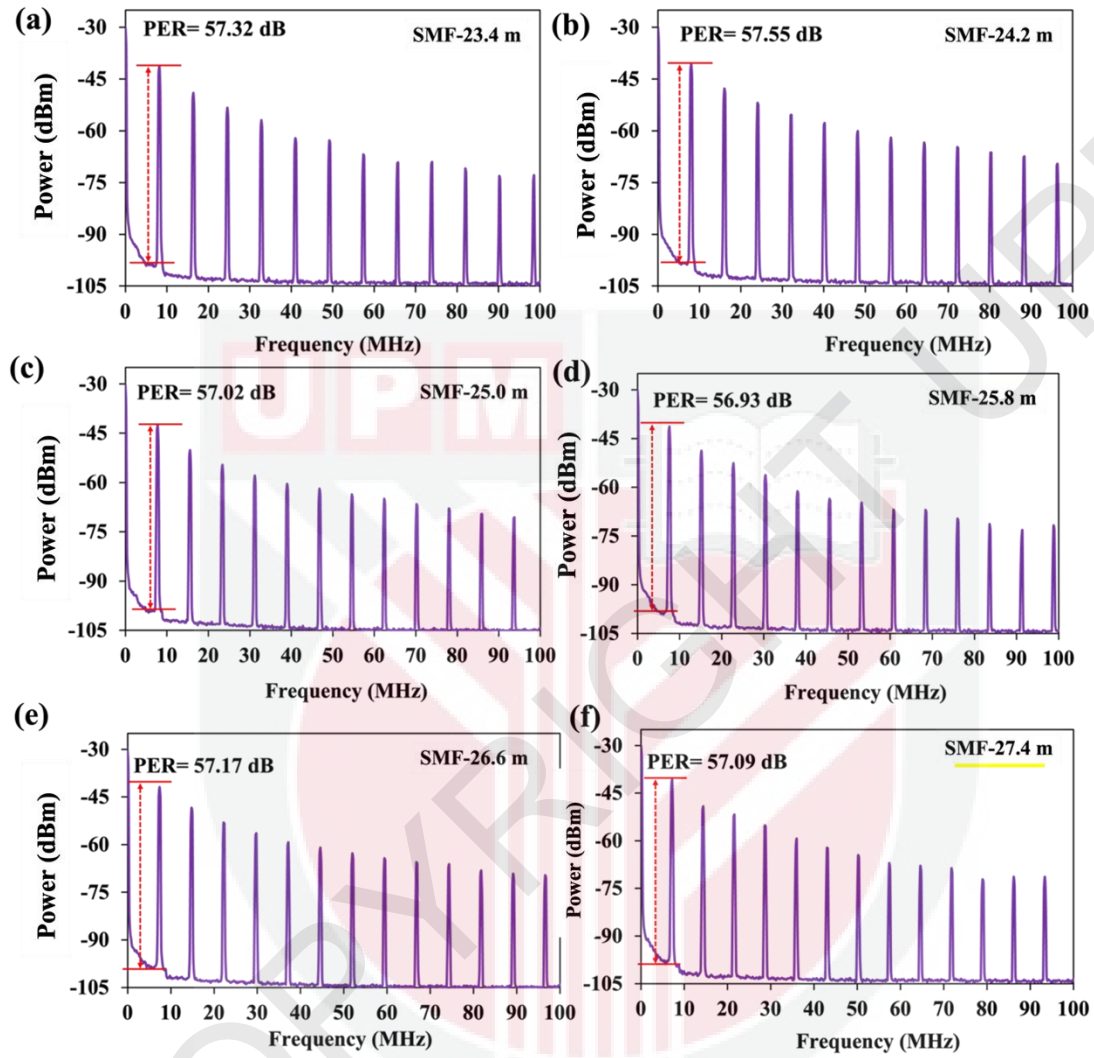

Figure E1 : RF Spectrum Measurement for (a) SMF-23.4 m, (b) SMF-24.2 m (c) SMF-25.0 m, (d) SMF-25.8 m, (e) SMF-26.6 m (f) SMF-27.4 m

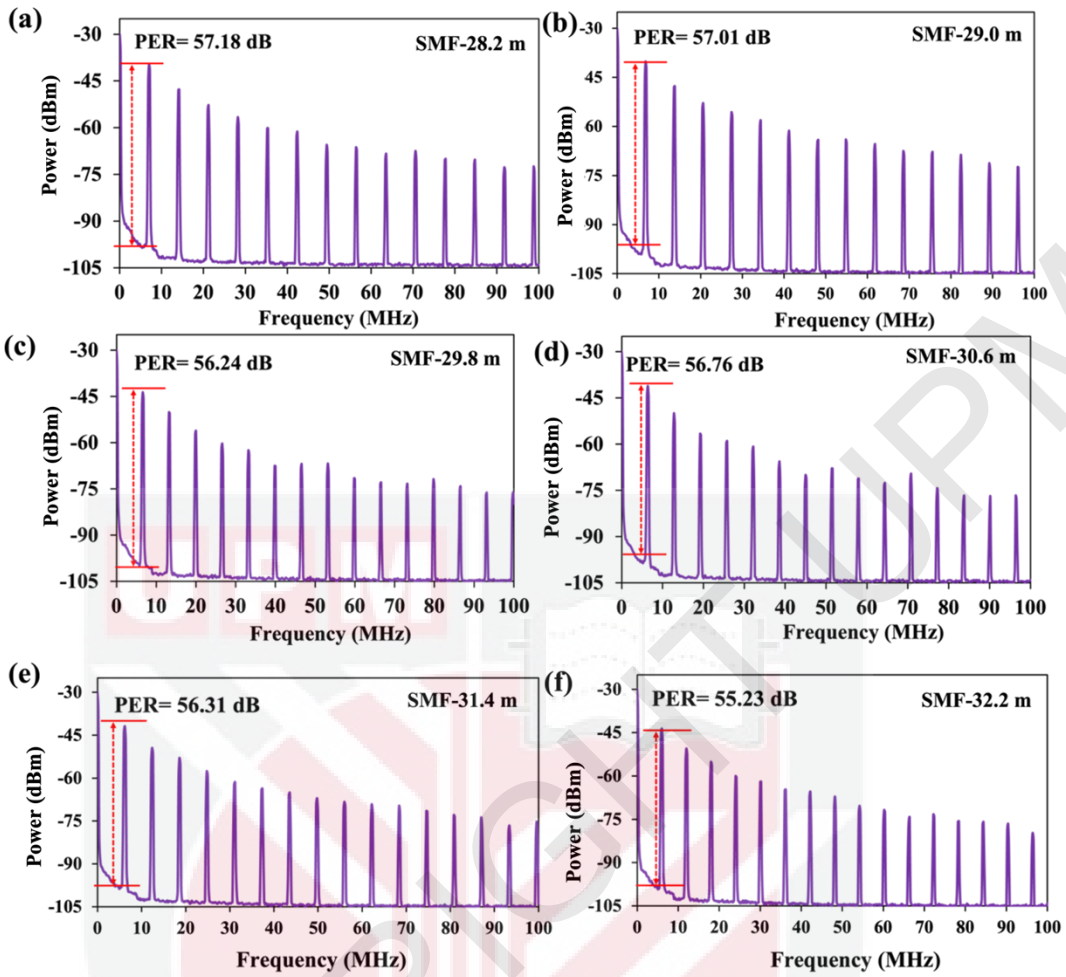

Figure E2 : RF Spectrum Measurement for (a) SMF-28.2 m, (b) SMF-29.0 m (c) SMF-29.8 m, (d) SMF-30.6 m, (e) SMF-31.4 m (f) SMF-32.2 m

Appendix F

OSA Spectrum Stability for Different SMF Length

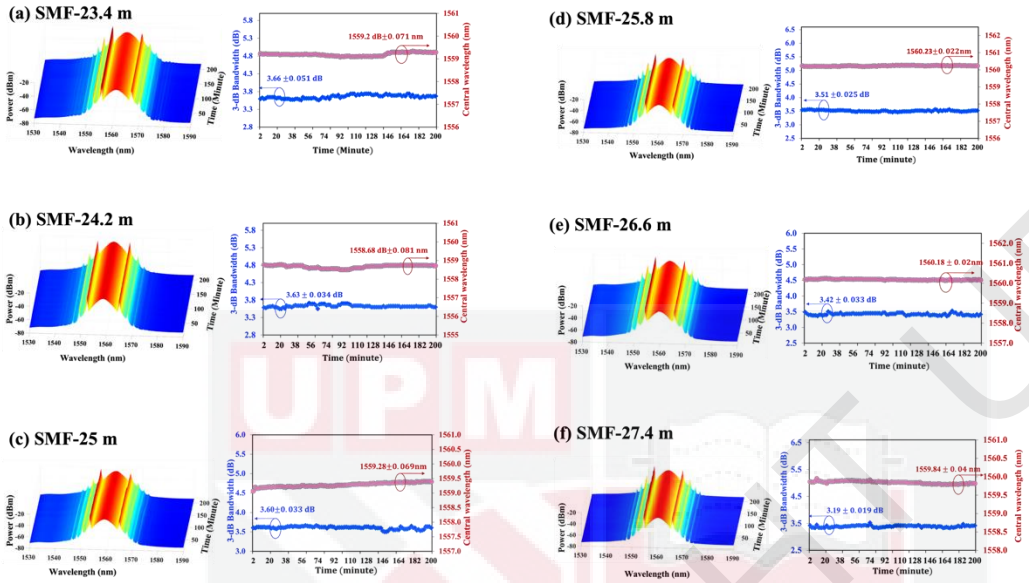

Figure F1 : OSA Spectrum Stability for (a) SMF-23.4 m, (b) SMF-24.2 m (c) SMF-25.0 m, (d) SMF-25.8 m, (e) SMF-26.6 m (f) SMF-27.4 m

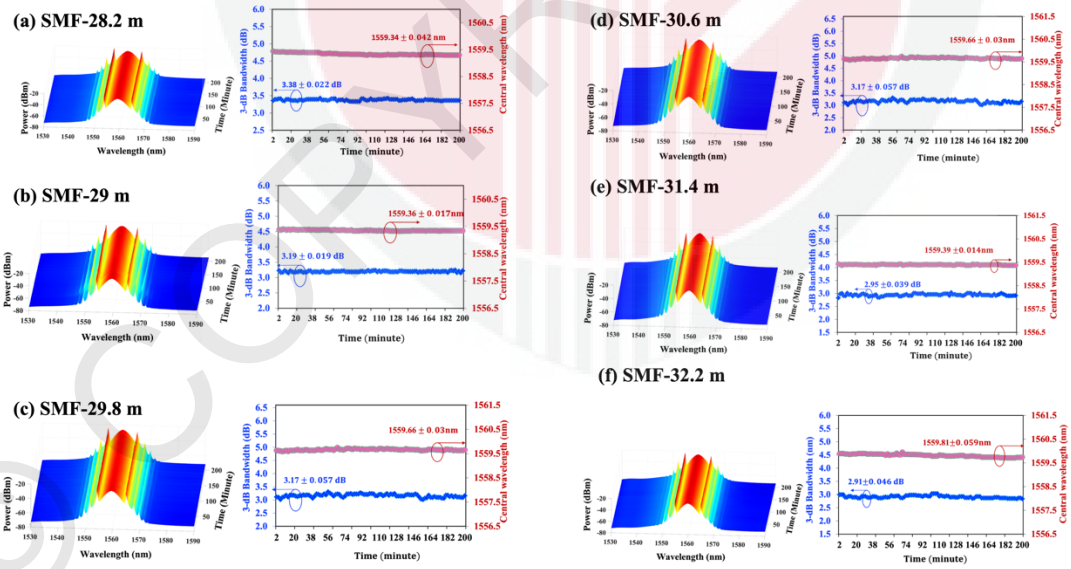

Figure F2 : OSA Spectrum Stability (a) SMF-28.2 m, (b) SMF-29.0 m (c) SMF-29.8 m, (d) SMF-30.6 m, (e) SMF-31.4 m (f) SMF-32.2 m

Appendix G

AC Stability Measurements for Different SMF Length

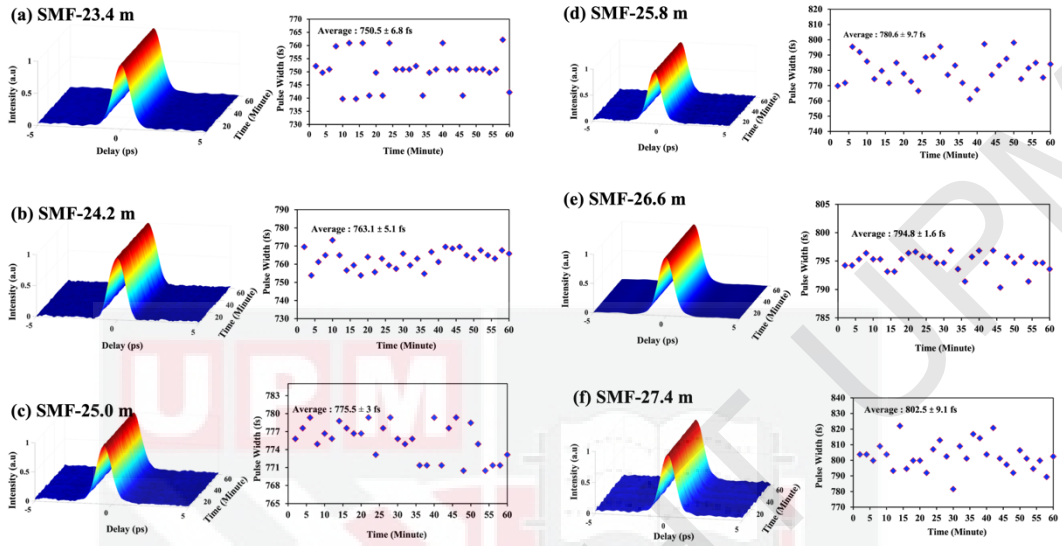

Figure G1 : AC Trace Stability for (a) SMF-23.4 m, (b) SMF-24.2 m (c) SMF-25.0 m, (d) SMF-25.8 m, (e) SMF-26.6 m (f) SMF-27.4 m

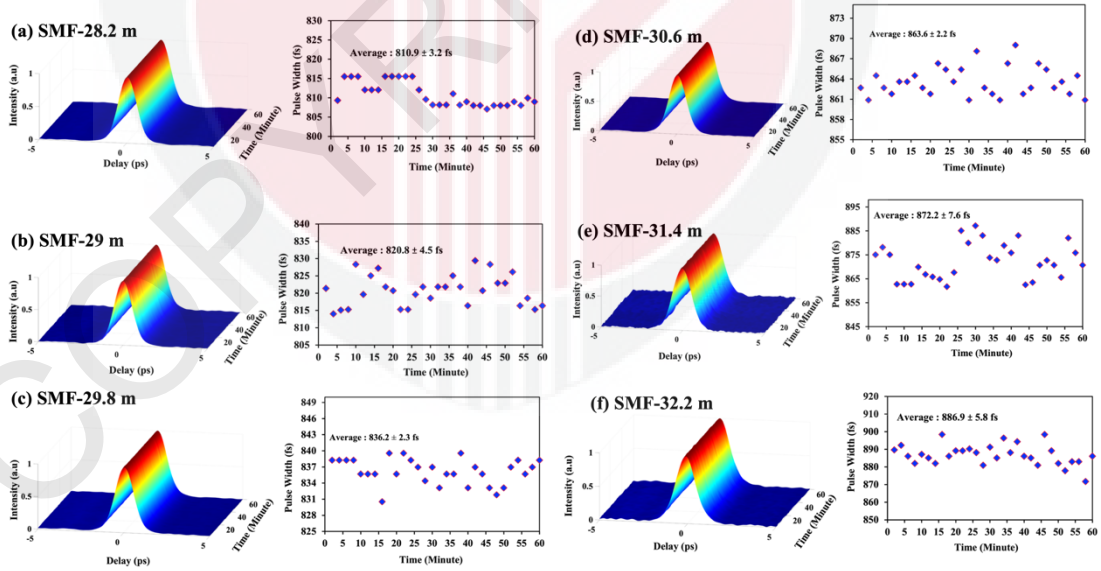

Figure G2 : AC Trace Stability for (a) SMF-28.2 m, (b) SMF-29.0 m (c) SMF-29.8 m, (d) SMF-30.6 m, (e) SMF-31.4 m (f) SMF-32.2 m

Appendix H

Osciloscope Trace for Different Nio Concentrations

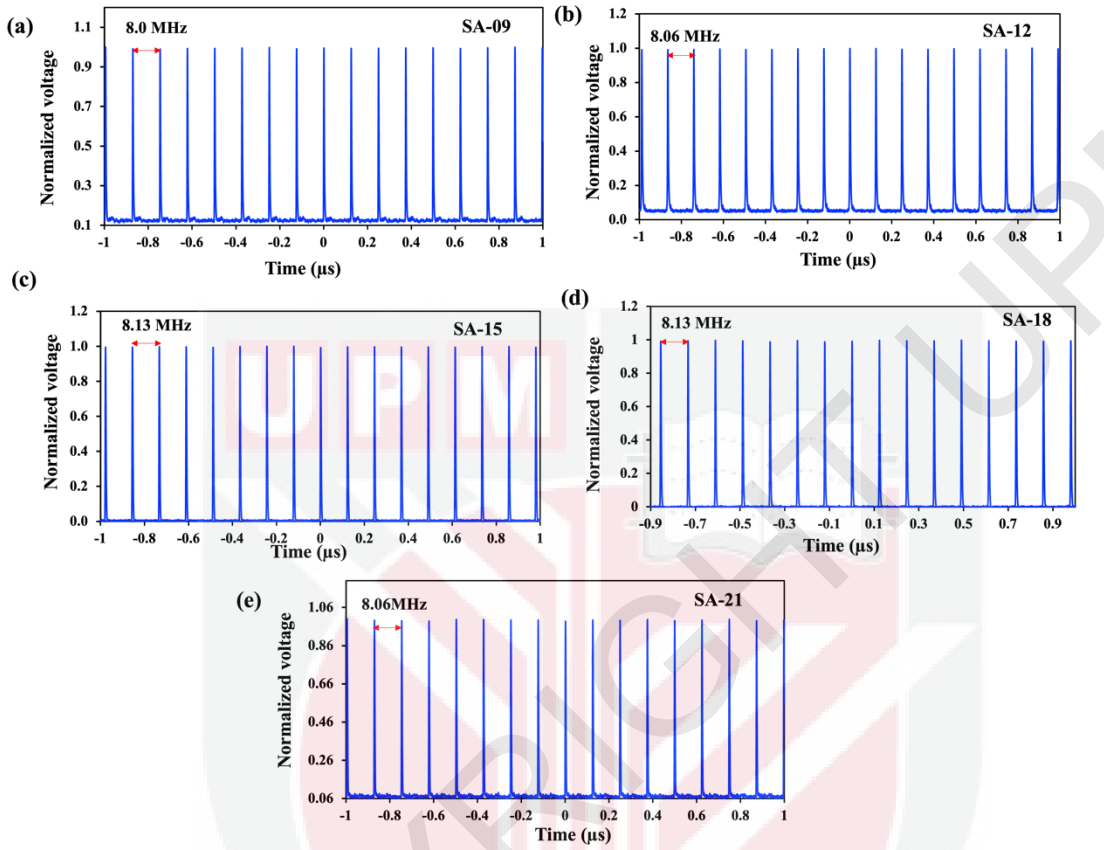

Figure H1 : Oscilloscope Trace for Different Concentrations (a) SA-09 (b) SA-12 (c) SA-15, (d) SA-18, and (e) SA-21

Appendix I

Peak Extention Ratio (PER) for Different Nio Concentrations

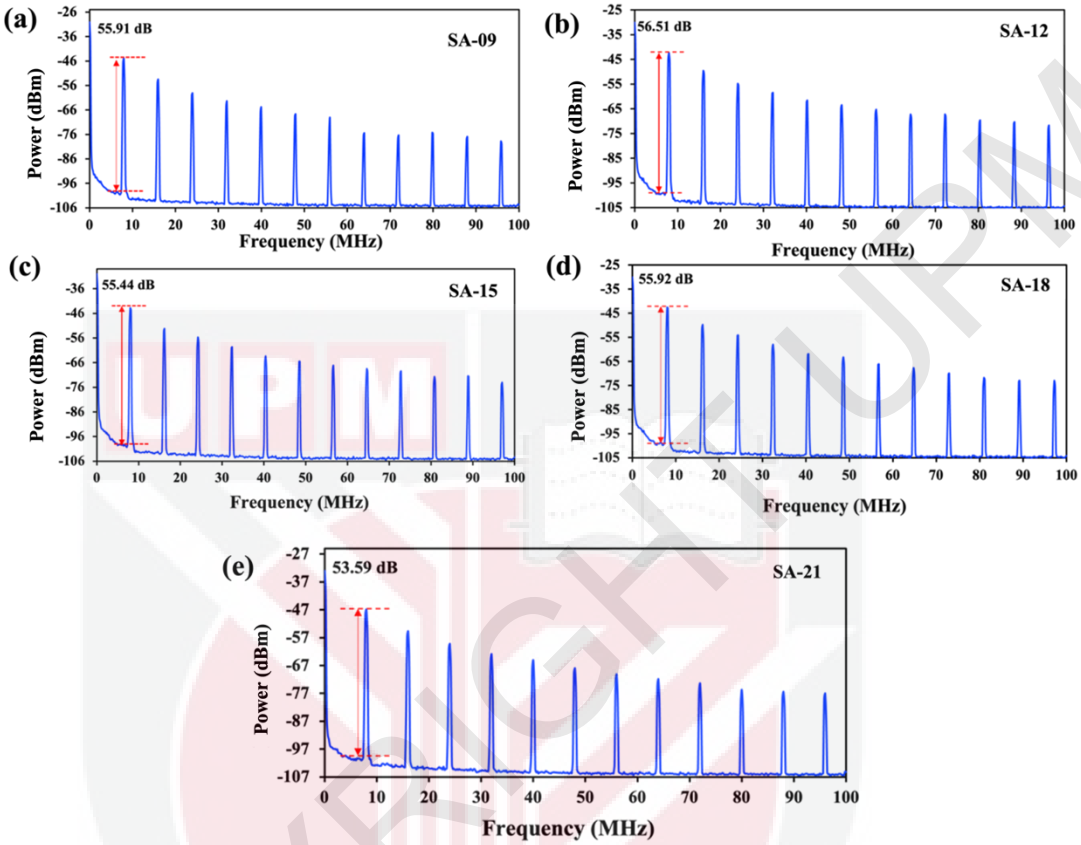

Figure I1 : PER for Different Concentrations (a) SA-09 (b) SA-12 (c) SA-15, (d) SA-18, and (e) SA-21

Appendix J

OSA Spectrum Stability for Different Nio Concentrations

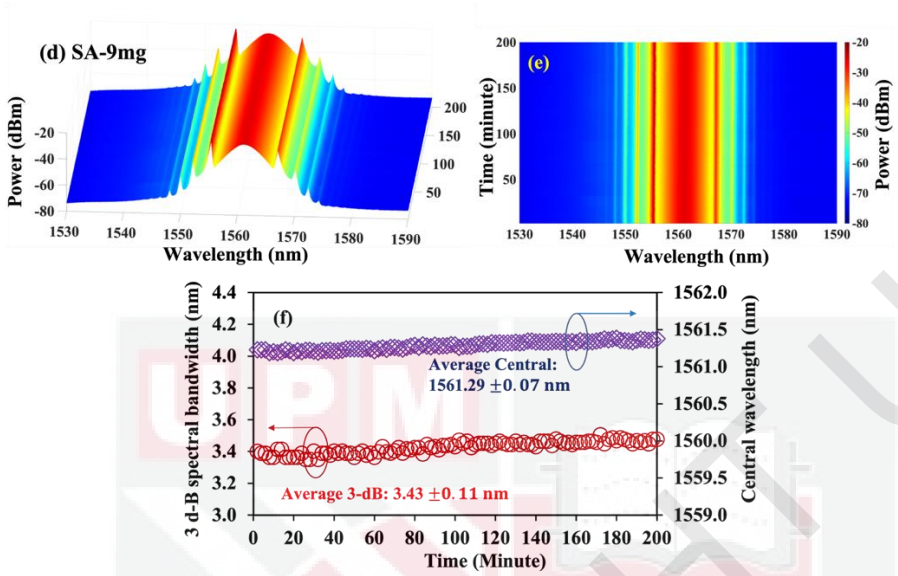

Figure J1 : Spectrum Stability for SA-09 (a) 3-D Spectrogram within 200 Minutes (b) Overview of (c) Measurements of 3-dB Bandwidth and Central Wavelength over 200 Minutes

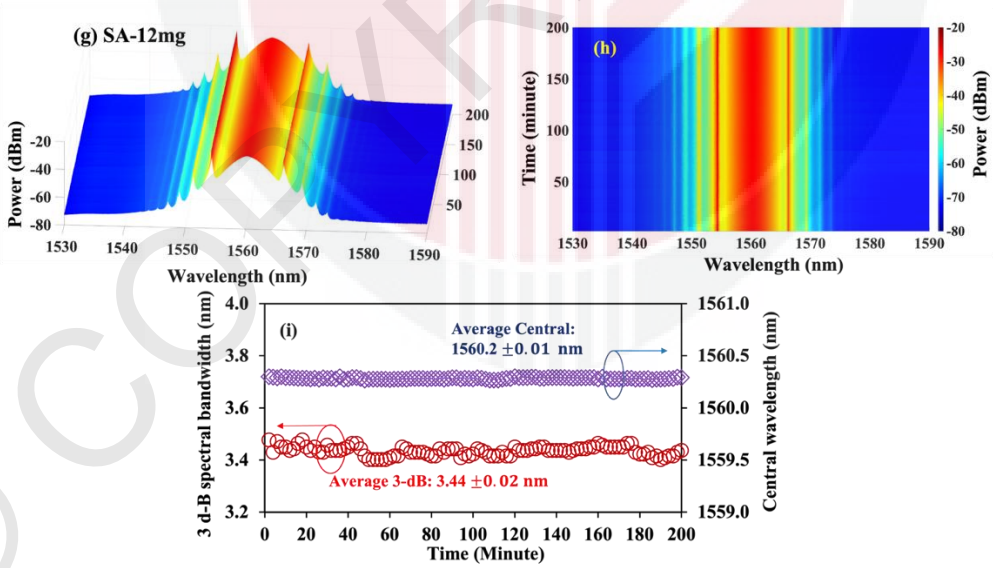

Figure J2 : Spectrum Stability for SA-12 (a) 3-D Spectrogram within 200 Minutes (b) Overview of (c) Measurements of 3-dB Bandwidth and Central Wavelength over 200 Minutes

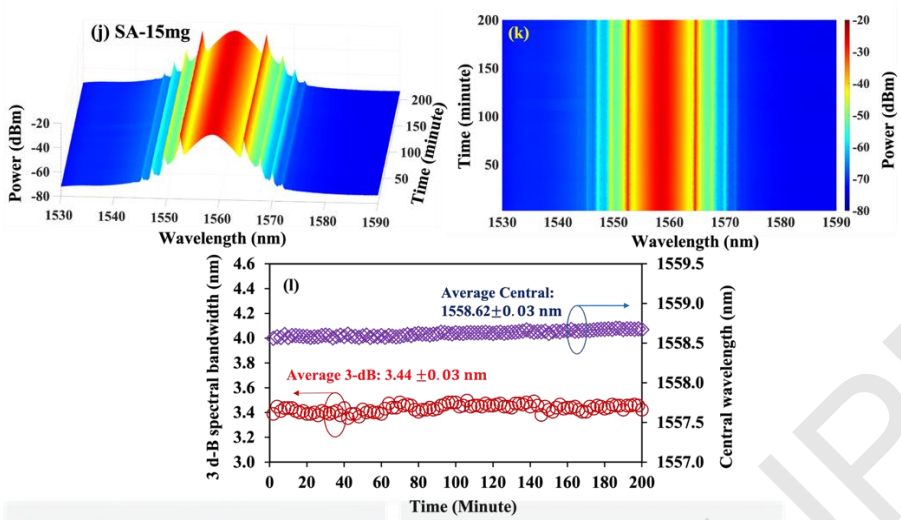

Figure J3 : Spectrum Stability for SA-15 (a) 3-D Spectrogram within 200 Minutes (b) Overview of (c) Measurements of 3-dB Bandwidth and Central Wavelength over 200 Minutes

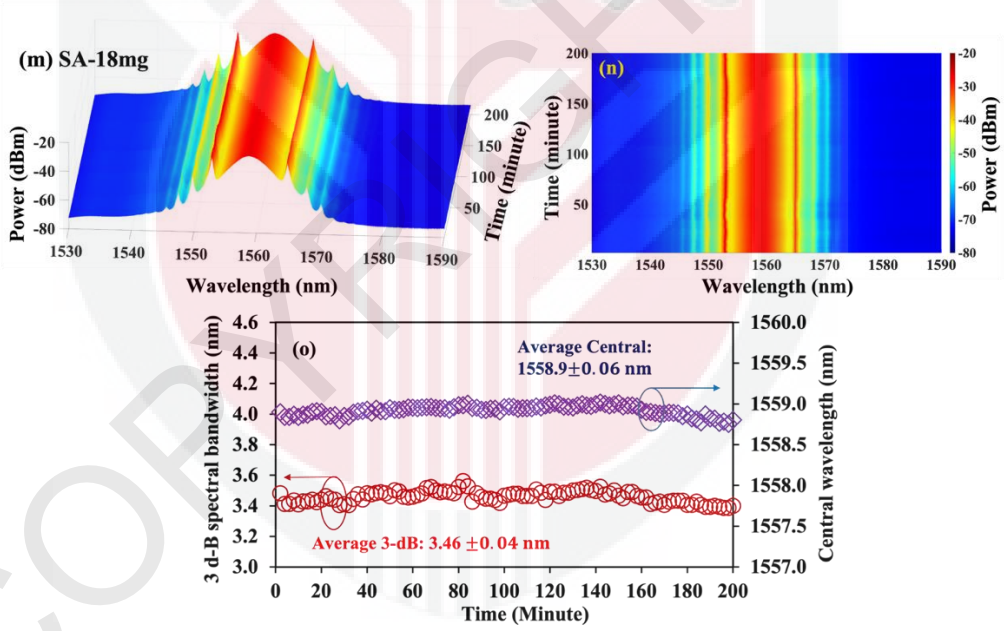

Figure J4 : Spectrum Stability for SA-18 (a) 3-D Spectrogram within 200 Minutes (b) Overview of (c) Measurements of 3-dB Bandwidth and Central Wavelength over 200 Minutes

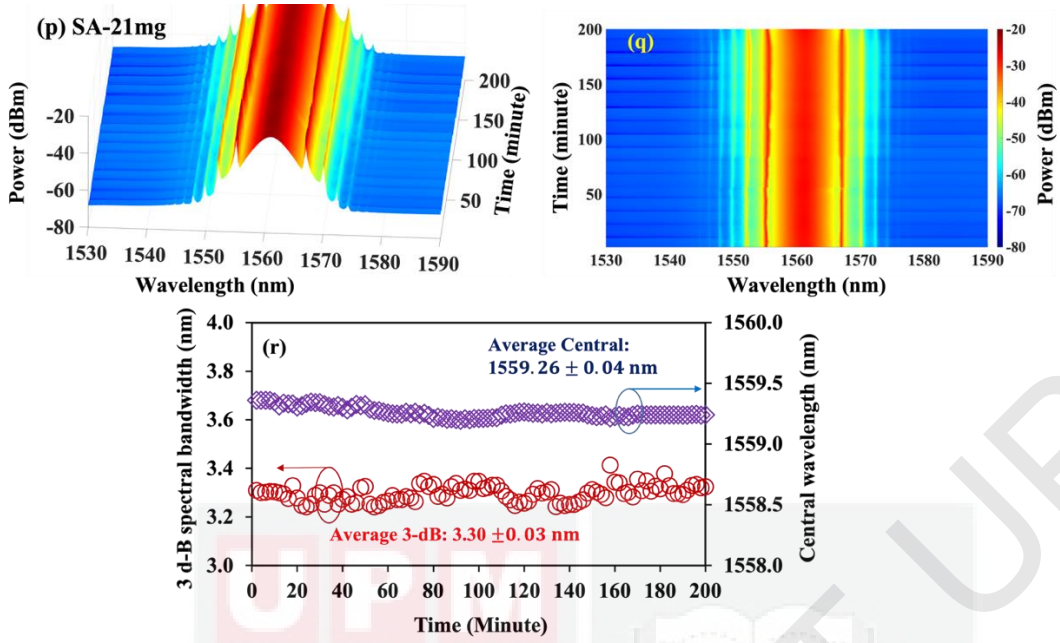

Figure J5 : Spectrum Stability for SA-21 (a) 3-D Spectrogram within 200 Minutes (b) Overview of (c) Measurements of 3-dB Bandwidth and Central Wavelength over 200 Minutes

Appendix K

Auto Correlator Stability for Differents Nio Concentrations

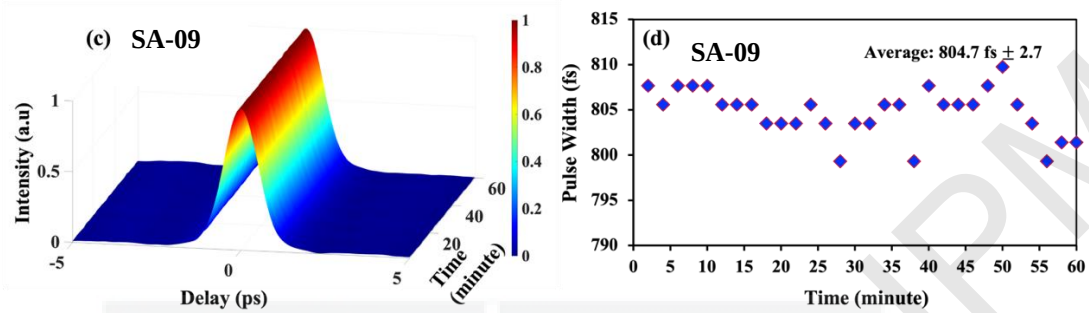

Figure K1 : Autocorrelator Stability for SA-09 (a) 3-D Spectogram of Normalised Autocorrelator within 60 Minutes. (b) Pulse-Width (fs) Measurements within 60 Minutes

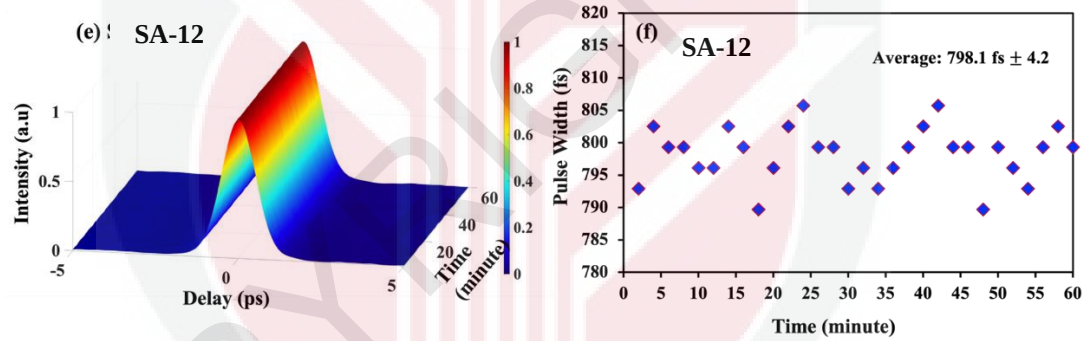

Figure K2 : Autocorrelator Stability for SA-12 (a) 3-D Spectogram of Normalised Autocorrelator within 60 Minutes. (b) Pulse-Width (fs) Measurements within 60 Minutes

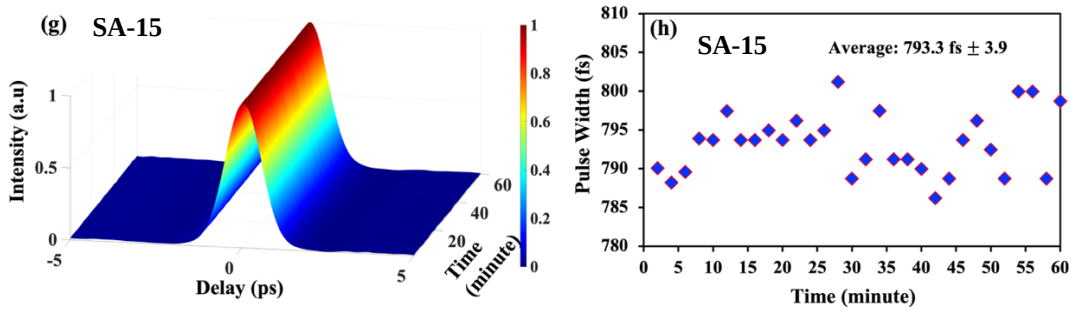

Figure K3 : Autocorrelator Stability for SA-15 (a) 3-D Spectogram of Normalised Autocorrelator within 60 Minutes. (b) Pulse-Width (fs) Measurements within 60 Minutes

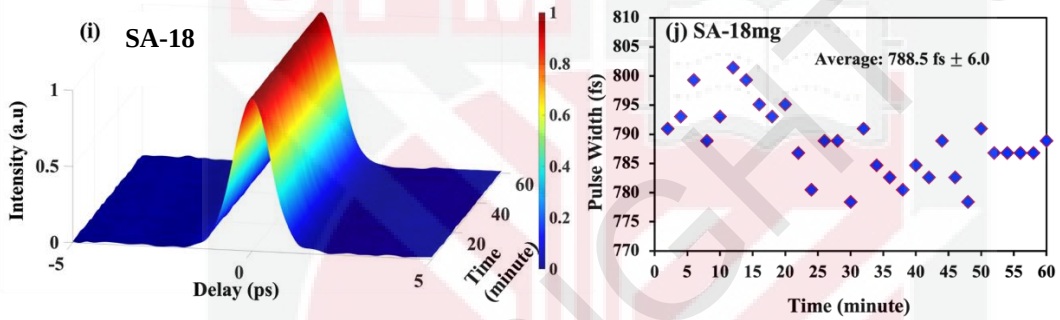

Figure K4 : Autocorrelator Stability for SA-18 (a) 3-D Spectogram of Normalised Autocorrelator within 60 Minutes. (b) Pulse-Width (fs) Measurements within 60 Minutes

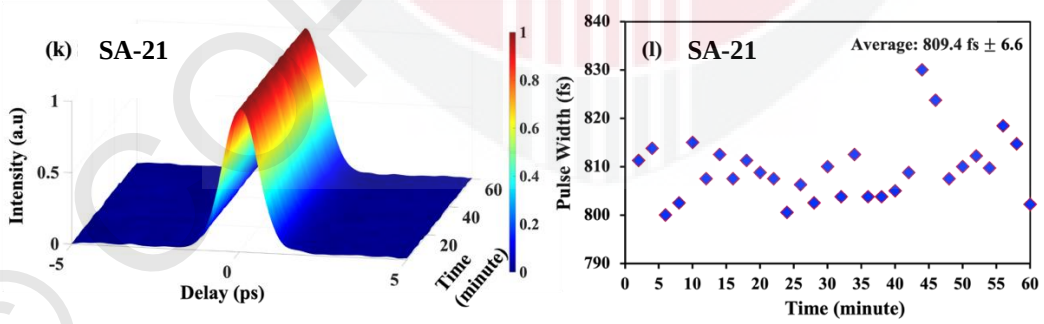

Figure K5 : Autocorrelator Stability for SA-12 (a) 3-D Spectogram of Normalised Autocorrelator within 60 Minutes. (b) Pulse-Width (fs) Measurements within 60 Minutes

BIODATA OF STUDENT

Siti Asma binti Che Aziz was born in Machang, Kelantan in 1985. She attained a B.Eng(Hons) in Electrical and Electronics Engineering from Universiti Kebangsaan Malaysia in 2008. In 2011, she completed her M.Sc in Electrical and Electronics Engineering from Universiti Kebangsaan Malaysia. She gained 4 years of experience as an assistant manager at TM Berhad before being appointed as a lecturer in Faculty of Electronics and Computer Technology and Engineering at Universiti Teknikal Malaysia Melaka in 2014. She is currently pursuing her Doctor of Philosophy Degree in Photonics Engineering at Universiti Putra Malaysia under SLAB scholarship provided by Ministry of Higher Education.

LIST OF PUBLICATIONS

Journals

S.A. Che Aziz, N. Mohd Yusoff, N.H. Zainol Abidin, C.A. Che Abdullah, Idris, M. I., M.T. Alresheedi, Ng, E. K., & Mahdi, M. A. (2023). Nickel oxide-embedded tapered fibre as a saturable absorber for ultrafast photonics. Optik, 295, 171508–171508. https://doi.org/10.1016/j.ijleo.2023.171508.

Conferences

"Characterization of Chitosan from Shrimp Shell Waste Extraction". S.A.C. Aziz, M.A. Mahdi, M.I Idris, N.H. Zainol Abidin, C.A.C. Abdullah, S. A. M. Chachuli. 12th International Fundamental Science Congress (iFSC) which is organized by Faculty of Science, Universiti Putra Malaysia (UPM).

Book Chapter

"Improvement of Chitosan Characterization from Shrimp Shell Waste Extraction". S.A.C. Aziz, S.A.M. Chachuli, M. I. Idris, N.H. Zainol Abidin, C.A.C. Abdulllah, M.A. Mahdi, 2022. Pp:164-168. International Fundamental Science Congress (IFSC 2021) ebook with eISBN: 9786299691402.
https://science.upm.edu.my/e_buku/the_12th_international_fundamental_science_congress_ifsc_2022-13990
https://heyzine.com/flip-book/99310bb75b.html